Monte Carlo algorithm for strongly interacting non-equilibrium quantum systems in nanoelectronics

Corentin Bertrand

Communauté
UNIVERSITÉ Grenoble Alpes

THÈSE

Pour obtenir le grade de

DOCTEUR DE LA COMMUNAUTÉ UNIVERSITÉ GRENOBLE ALPES

Spécialité : **Physique Théorique**

Arrêté ministériel : 25 mai 2016

Présentée par

Corentin BERTRAND

Thèse dirigée par **Xavier WAINTAL, CEA**
et codirigée par **Christoph GROTH, CEA**

préparée au sein du **Laboratoire Photonique, Électronique et Ingénierie Quantiques (PHELIQS) – IRIG – CEA**
dans **l'École Doctorale de Physique de Grenoble (ED n°47)**

Algorithme Monte-Carlo pour les systèmes quantiques à fortes interactions et hors d'équilibre en nanoélectronique

Thèse soutenue publiquement le **27 septembre 2019**,
devant le jury composé de :

M Markus HOLZMANN
Directeur de recherche, LPMMC à Grenoble, Président du jury
M Jan VON DELFT
Professeur, Université Ludwig-Maximilians à Munich, Rapporteur
M Dider POILBLANC
Directeur de recherche, IRSAMC à Toulouse, Rapporteur
M Denis BASKO
Directeur de recherche, LPMMC à Grenoble, Examinateur
M Félix WERNER
Chargé de recherche, Laboratoire Kastler Brossel à Paris, Examinateur

Thèse de Doctorat

Monte Carlo Algorithm for Strongly Interacting Non-Equilibrium Quantum Systems in Nanoelectronics

Algorithme Monte-Carlo pour les systèmes quantiques à fortes interactions et hors d'équilibre en nanoélectronique

Corentin Bertrand

Soutenue le 27 septembre 2019 à Grenoble

Abstract

Non-equilibrium quantum many-body problems are attracting increasingly more attention in condensed matter physics. For instance, systems of interacting electrons submitted to an external (constant or varying) electric field are studied in nanoelectronics, and more recently in materials, for the search of novel non-equilibrium states of matter. In this thesis, we developed a new numerical generic method for these problems, and apply it to the Anderson impurity model. This model is a good representation of a quantum dot coupled to one or several leads, and gives rise at equilibrium to the Kondo effect — a manifestation of Coulomb interactions within the dot. We apply our method to compute the collapse of the Kondo effect when the quantum dot is driven out of equilibrium by a voltage bias. Our method is based on a diagrammatic Quantum Monte Carlo (QMC) algorithm. The QMC is an optimized version of the algorithm of Profumo *et al.* [*Phys. Rev. B* **91**, 245154 (2015)], which computes time-dependent observables or correlation functions as perturbation series in the interaction strength U. To address the problem of diverging series at large U, we constructed a robust resummation scheme which analyses the analytical structure of the series in the U complex plane, for proposing a tailor-made regularization method using a conformal transform of the complex plane. As a post-treatment, a Bayesian technique allows to introduce non-perturbative information to tame the exacerbation of error bars caused by the resummation. We emphasize the potential application to study non-equilibrium materials through "quantum embedding" schemes, such as the Dynamical Mean Field Theory (DMFT), which allow to study lattice models through solving a self-consistent impurity model.

Résumé

Les problèmes quantiques à plusieurs corps hors d'équilibre concentrent de plus en plus d'attention en physique de la matière condensée. Par exemple, les systèmes d'électrons en interaction soumis à un champ électrique externe (constant ou variable) sont un sujet d'étude important en nanoélectronique, mais aussi plus récemment en science des matériaux, afin d'identifier de nouveaux états de la matière hors d'équilibre. Dans cette thèse, une nouvelle méthode numérique et générique a été conçue pour ces systèmes, et appliquée au modèle d'impureté d'Anderson. Ce modèle représente fidèlement un point quantique couplé à une ou plusieurs électrodes, et rends compte à l'équilibre de l'effet Kondo : une manifestation des interactions Coulombiennes au sein du point quantique. Cette méthode a permis d'observer la disparition de l'effet Kondo lorsque le point quantique est conduit hors d'équilibre par une différence de potentiel. Le cœur de la méthode utilise un algorithme Monte-Carlo Quantique diagrammatique. Il s'agit d'une version optimisée de l'algorithme de Profumo *et al.* [*Phys. Rev. B* **91**, 245154 (2015)], qui calcule des observables dépendantes du temps ou des fonctions de corrélations à travers leurs séries de perturbation en puissances de la force de l'interaction U. Le problème de la divergence de ces séries à grand U est traité par une méthode de resommation robuste. Elle analyse la structure analytique des séries dans le plan complexe en U afin de proposer une régularisation sur mesure par transformation conforme du plan complexe. En post-traitement, une technique Bayésienne permet d'inclure des informations non perturbatives pour réduire les barres d'erreurs qui ont été exacerbées par la resommation. Cette méthode pourrait être appliquée à l'étude de matériaux hors d'équilibre grâce aux algorithmes de "quantum embedding", comme la théorie de champs moyen dynamique, qui permettent l'étude de modèles sur réseaux par la résolution d'un problème d'impureté autocohérent.

Remerciements

Ce travail est le fruit de trois intenses années passées en compagnie de personnes formidables qui y ont contribué de diverses façons.

Tout d'abord mon directeur de thèse Xavier Waintal, qui est une source intarissable d'idées et d'optimisme. Même aux heures les plus sombres, il a toujours su apporter une nouvelle lumière, souvent inattendue, une idée, une découverte; ou tout simplement parfois me rappeler que, même si ça ne fonctionne pas, on a quand même appris quelque chose.

Plus discret, mais non moins essentiel, mon co-directeur de thèse Christoph Groth, qui n'a pas son pareil pour animer les débats du déjeuner.

Ensuite, nos collaborateurs. Olivier Parcollet pour son expertise sur le problème quantique à plusieurs corps. Serge Florens pour ses calculs NRG. Tous les deux m'ont apportées de précieux conseils et ont partagé leur expertise lors de nos discussions.

Les étudiants, postdocs et stagiaires du Groupe Théorie, qui m'ont soutenues à leurs façons par leurs présences, leurs problèmes, leurs solutions, leurs désespoirs, leurs joies. Je pense aux partenaires de randonné et de ski: Pacôme qui ne manque pas une occasion de sortir prendre l'air en montagne, et Benoit qui marche bien plus vite qu'il n'en a l'air. Mais aussi tous les autres avec qui j'ai partagé de bons moments: Stefan, Mathieu, Thomas, Vincent, Shuo, Antonio, Tatiane et Marjan.

Enfin mes parents Catherine et Christian, ma sœur et mon frère, et mes amis à Grenoble ou ailleurs, qui ont su me faire passer de merveilleux weekends et vacances pour me ressourcer.

Je souhaite les remercier tous chaleureusement pour leur soutient.

Contents

Introduction

Quantum many-body physics is the field of research aiming at describing and predicting quantum systems of many interacting particles. Unlike in one-body systems, which can be pictured as systems where particles "ignore" each other, fascinating collective phenomena emerge from the complex interplay between particles in many-body systems. In condensed matter physics, interactions between *e.g.* electrons are essential to understand a large spectrum of phenomena including superconductivity, Mott insulators or the Kondo effect. But the Shrödinger equation for such systems is notoriously hard to solve, and exact analytical solutions are known only in few simple cases. For this reason, exact numerical methods have become standard tools for these problems.

In parallel to this field, important experimental improvements have been made since the 1980s for manipulating quantum particles individually. In particular, nanoscale electronic circuits under low temperatures allow to study the motion of single electrons in complex and highly controlled geometries [43, 88, 98]. Electrons are pushed out of their equilibrium state by *e.g.* photonic excitations, submitting a voltage difference, or sending microwaves pulses through the circuit. Applications in quantum nanoelectronics aim at developing novel quantum technologies with *e.g.* reduced-size low consumption transistors, more sensitive sensors, as well as long-lasting and fast computer memories. To this regard, many-body effects represent new potential technologies, but have only been poorly explored in this context.

A typical nanoelectronic device is the quantum dot, a zero dimensional electron "pool", which behaves as an artificial atom coupled to one or several reservoirs. When it contains an unpaired electron, its magnetic moment couples with the spin of the conduction electrons in the reservoirs, heavily affecting the conductance through the dot [28, 42, 43, 149]. This is known as the Kondo effect, a hallmark of quantum many-body physics in zero dimensional systems. It was originally observed in magnetic impurities in metals, antiferromagnetically coupled to the surrounding electrons, and causing an unexpected minimum of resistance as a function of temperature [83]. The Kondo physics is the subject of an impressive amount of studies, still today [73, 85, 135, 136, 156]. The Kondo effect in thermal equilibrium is well understood: an exact analytical description exists [9, 78, 165, 179, 180], as well as robust and efficient numerical solutions of interacting impurity models [19, 181]. But the status of the Kondo effect out of equilibrium, *e.g.* in quantum dots under a voltage bias is still the subject of an intense research [31, 126, 174], as there is no robust and generic predictive tools for this problem. In this thesis, we contributed to fill this gap. We developed a numerical method to compute for example the density of states in a voltage biased quantum dot in the Kondo regime, which is shown in Fig. 1. We will develop along this document the tools to obtain such results.

Studying non-equilibrium regimes is also interesting in other many-body problems [72, 107, 162]. Indeed, when driven out of thermal equilibrium, many interacting systems reach a stationary state which has no equivalent in their equilibrium counterpart. This

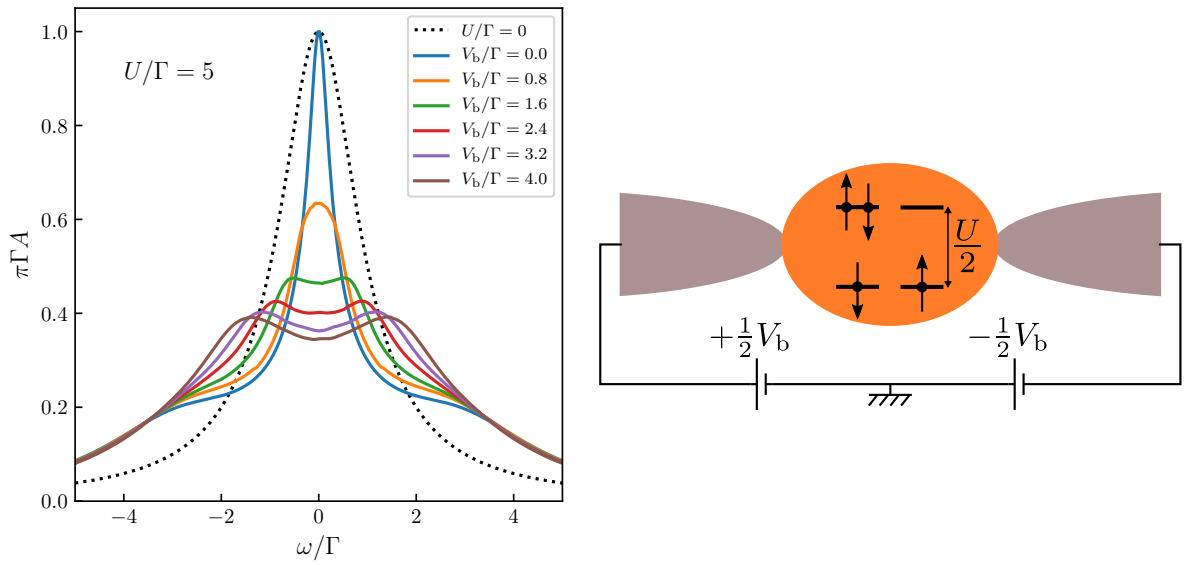

Figure 1: A two-terminal Anderson impurity model under a voltage bias V_b (right panel) and the corresponding density of state calculated in this thesis (left panel). The model corresponds to a quantum dot connected to two leads with a tunneling rate Γ. We depict here a particle-hole symmetric model with Coulomb repulsion U between electrons and between holes. Its density of states (left panel) shows the splitting of a central resonance (the Kondo resonance) as V_b increases. This is a feature of the interplay between the many-body Kondo effect and the non-equilibrium physics. We will develop along this thesis the tools to obtain such results. The model and discussion of this result are in chapter 5.

is the case of certain materials with strong electronic interactions where a hidden state can be triggered with electric field or light pulses, such as light-induced superconductivity [20, 37, 115–117] or metal-insulator transition driven by electric field [113]. More fundamentally, the role of interactions in the formation of a thermal state in quantum systems is still an important theoretical problem, and can be addressed by studying the relaxation of many-body systems after a sudden change of Hamiltonian [106] – so-called quenched systems.

Solving models of interacting impurity coupled to a bath is an important step for the study of materials. Indeed, "quantum embedding" methods, such as the Dynamical Mean Field Theory (DMFT) [40, 45, 84] or its extensions [14, 15], provide numerical schemes to approximate lattice interacting systems — such as a crystalline material — by mapping it onto a self-consistent impurity problem. DMFT extends the mean field theory, as the dynamics (and not only average properties) of the bath is generated from the solution of the impurity itself. In this context, numerical solvers for the impurity problem have to be robust to arbitrary bath. Although constructing a robust approximation-free *non-equilibrium* impurity solver is still a challenge today, the perspectives are stimulating [13].

At the intersection of quantum many-body and non-equilibrium physics, analytic methods developed for equilibrium give poor results and the predictive power of numerical tools is still incipient. Nevertheless, many methods traditionally used for the equilibrium many-body problem have been extended to non-equilibrium. Most of them computes the time evolution of a quenched system: the system is first prepared in a

"simple" state (*e.g.* non interacting) that is well described. At a given time, the Hamiltonian is changed to bring in complexity (*e.g.* interactions or voltage) and we let the system evolve. It relaxes at long time into a steady state solution of the new Hamiltonian. The Density Matrix Renormalization Group (DMRG) [153, 154, 176, 177], a powerful method in one dimensional equilibrium systems based on a matrix-product representation of the many-body states, has been extended to time-dependent Hamiltonians and to compute currents and other transport quantities [60, 156]. So was Wilson's Numerical Renormalization Group (NRG) [4, 5] method, a renormalization group method which is very successful in solving impurity problems at equilibrium [19, 181]. Methods based on many-body Green's function, path integral or Feynman diagrams expansions are used in the imaginary-time Matsubara formalism to compute observables and correlation functions at equilibrium. To manage time-dependant quantities and non-equilibrium systems, they have been formulated in the real-time Schwinger–Keldysh formalism [79, 134, 157]. In numerical solvers, this is most notably used for the large family of Quantum Monte Carlo (QMC) algorithms [44, 129–132, 144, 173–175]. Despite this intense activity, most of these algorithms suffer from intractable complexity for computing the long time dynamics after the quenching of the system.

For diagrammatic QMC in the real-time formalism, this complexity is embodied in the so-called "dynamical sign problem". An observable is written as a perturbation series, the order n coefficient being a sum of n-dimensional integrals called Feynman diagrams. These integrals being of high dimension, they are computed using a Monte Carlo algorithm. The sign problem arises when large cancellations occur between sampled contributions, so that the number of samples required to reach longer times skyrockets. Two ways out are being developed currently: the inchworm algorithm [11, 12, 21, 22, 24–26, 47, 91, 135], and a rewriting of traditional diagrammatic QMC, by regrouping diagrams into determinants and explicitly summing cancelling terms [128]. The latter is free of dynamical sign problem, and is able to reach the long time limit, but with a computational complexity scaling as $\mathcal{O}(2^n)$ in the perturbation order n. An analogous improvement has been developed in the equilibrium Matsubara formalism [109, 142, 160].

Despite this progress, some important obstacles remained before a robust algorithm can be used for many-body impurity problems. First, of most interest are frequency resolved quantities, such as the density of states, whereas previous real-time QMC methods yield a single quantity at a given time. To apply Fourier transform, a large time range has to be sampled as finely as large frequencies are needed. This leads to a heavy computational cost. Second, diagrammatic QMC provides a perturbation series in some parameter U (in this work the interaction strength). In the perturbative regime, results are easily obtained by summing the series. But at large U, the series may diverge and resummation methods are then necessary. Numerous methods are known [56] and used in physics including Padé approximants [16], Lindelöf extrapolation [97, 166] or Cesàro-Riesz technique [129]. However, these do not provide information about whether or not a series can be resummed, to which precision, and what method is best suited for it. Plus, they are difficult to automatize, which is a necessary condition for practical usage in a DMFT loop.

In this work, we aim at computing Green's functions — correlation functions for the presence of electrons between two space-time points — of a non-equilibrium quantum impurity problem. We can derive many quantities of interest from these correlations, for example density of states or currents. We developed a real-time diagrammatic QMC based on the work of Ref. [128], and implemented using the TRIQS package [121]. It com-

putes Green's functions as perturbation series in powers of the interaction strength U. Each coefficient is a multidimensional integral of increasingly large determinants, which regroup the contributions from all diagrams. For a Green's function $G(t, t')$ between two times t and t', we observed that the calculation of the determinants is largely independent from t. Also, the t-dependent part can be separated from the other by writing G as a convolution between a trivial t-dependent function and a complex t-independent "kernel". We designed an optimized Monte Carlo method to compute the kernel, allowing to recover G on a wide t range by a simple convolution. Therefore, in a single Monte Carlo run, we obtain, after Fourier transform, the series for the full frequency dependent Green's function. The series obtained — of the form $\sum_n F_n U^n$ — has a convergence radius R_F, meaning it diverges for $|U| > R_F$. The divergence is caused by the analytical structure of the series taken as a function of the complex variable U, *i.e.* singularities $U_0, U_1, \ldots$ in the U complex plane which constrain its convergence radius $R_F = \min(|U_0|, |U_1|, \ldots)$. Therefore, we considered the problem of resummation of the divergent series as a problem of sending away singularities in the complex plane. We designed a scheme to detect the singularities responsible for the divergence. From this information, conformal transforms are used to move them away by deforming the complex plane. In addition, a Bayesian technique was used to reduce error bars by including non-perturbative information into the resummed series. Finally, we applied our methodology to the Anderson impurity model [8]. Perturbation series of the impurity Green's function were computed up to $\sim 10^{\text{th}}$ order. At equilibrium, we observed the Kondo effect in the strong interaction regime, which was benchmarked against state of the art NRG calculations. Out of equilibrium, we computed non-equilibrium density of state (as shown in Fig. 1), current–voltage characteristics and the electronic distribution function.

This thesis is organized as follows. In chapter 1, we review the main features of the Kondo effect and its theoretical treatment in term of renormalization group. Out of equilibrium, we emphasize on its experimental signature in quantum dots and its theoretical and numerical treatment. We devote chapter 2 to the introduction of the Schwinger–Keldysh formalism within which Green's functions are expanded in power series, and the coefficients interpreted in the light of Feynman diagrams. Anticipating the Monte Carlo calculations, kernels are then defined and their relation with the Green's functions are derived. The Monte Carlo algorithm is then detailed in chapter 3, after an introduction to Markov chain Monte Carlo using the Metropolis–Hastings algorithm. We recall the work of Ref. [128] before extending it to compute kernels. In chapter 4, the resummation procedure is explained and illustrated with an example. Finally, chapter 5 shows the application to the Anderson impurity model.

Chapter 1

The Kondo effect: a quantum many-body problem

The Kondo effect is probably one of the most iconic quantum many-body effects. It arises when a localised magnetic moment is antiferromagnetically coupled to a continuum of electrons. At low temperature, the moment is screened by the electrons spins, which enhances deeply their scattering rate on the local moment, and therefore their transport properties. It has been the subject of an intense research since its observation in metals containing magnetic impurities, as a minimum of resistance when temperature is lowered [64]. Theoretical developments led to the introduction of the powerful renormalization group methods [7, 181] in condensed matter physics, before exact solutions of interacting impurity models were found with a Bethe ansatz [165].

Nevertheless, it still attracts a lot of attention, mainly for two reasons. First, it can be observed with unprecedented control in quantum dots. These allow in addition to study the Kondo physics under a voltage difference, hence mixing the many-body and non-equilibrium physics. Second, interacting impurity models — which contains the Kondo physics — can be used to study lattice models and real materials with strong electronic correlations through a quantum embedding self-consistent loop. Being able to resolve the Kondo physics is therefore important in the task to study the interplay between many-body and out-of-equilibrium physics — whether it is in impurities, in quantum dots, or in strongly correlated materials.

1.1 Magnetic impurities in a metal

1.1.1 Minimum of resistance and the Kondo problem

Electric resistance in a metal is caused by scattering of the conduction electrons. At low temperature, scattering events are caused by phonons and impurities — or larger defects — in the crystalline structure. It was believed before the 1930s that resistance in metals should decrease when temperature is lowered. Indeed, following Matthiessen's rule, the resistance caused by phonons and impurities simply add up. Considering a Debye spectrum for the phonons, their contribution to resistance scales as T^5 at low temperature T. The contribution of defects should be independent of temperature, hence the total resistance is expected to decrease monotonically and saturates when temperature is lowered. The zero temperature resistance is then given by defects only.

However, many experimental evidences of a *minimum of resistance* in dilute alloys

such as gold with iron impurities were gathered from the 1930s [50]. The origin of the now called Kondo effect was found to be impurities containing an unpaired electron in a d or f shell orbital, hence a net local magnetic moment. Comparisons between different impurity concentrations c_{imp} concluded that the effect was not related to interactions between impurities [83]. Indeed, the minimum of resistance occurs at a temperature T_{min} roughly proportional to $c_{\text{imp}}^{1/5}$, therefore weakly dependant on the concentration. In addition, the resistance at zero temperature and the minimal resistance are proportional to c_{imp}, so that the relative depth of the minimum is independent from the concentration.

Physical picture

The local magnetic moment of the impurity is coupled with the conduction electrons through an antiferromagnetic exchange interaction. When temperature goes below the Kondo temperature, the effective coupling with electrons near the Fermi level is increased: the system enters a strong coupling regime. In addition to scattering on the impurity potential, coherent scattering events which flip the impurity spin occurs. The scattering rate is particularly enhanced for electrons near the Fermi level, which then screens the impurity moment. This results into a singlet ground state between the impurity and the electrons spin [181]. The enhanced scattering rate when temperature is lowered explains the observed minimum of resistance.

In the strong coupling regime, low energies are well described by Landau's Fermi liquid theory [63, 119]. Near the impurity, electrons are renormalized into almost free quasiparticles. This local Fermi liquid is governed by the Kondo temperature T_{K}. The renormalized mass of the quasiparticles is $\sim T_{\text{K}}^{-1}$, their residual interaction is $\sim T_{\text{K}}$, and their density of state is a Lorentzian of width $\sim T_{\text{K}}$ centered on the Fermi level. This peak is called the Kondo resonance.

For temperatures $T \ll T_{\text{K}}$, the Kondo temperature is the only energy scale of the system. The low energy excitations and the thermodynamics are therefore *universal* functions of T and T_{K}.

The Kondo s-d exchange model

The exact origin of the anomalous resistance minimum was famously discovered by J. Kondo [83] about 30 years after its experimental discovery. His explanation revealed the many-body nature of this phenomenon. Non-magnetic impurities — with zero total spin — affect conduction electrons only through a scattering potential which adds up to the lattice potential. The induced resistance is independent from the temperature. However, a magnetic impurity has an internal degree of freedom (its spin) whose fluctuations affect how electrons are scattered on it. The coupling of an electron to the impurity indeed depends on the current state of the impurity spin, hence on the previous scatterings. The conduction electrons cannot be considered independent, they are correlated.

Kondo worked on a model where the impurity is reduced to a localized magnetic moment $\vec{\mathbf{S}}$ and is coupled by exchange interaction to the spin of the conduction electrons, assumed non-interacting. This is called s-d exchange model, or more simply Kondo

model. Assuming the coupling J is the same for all electrons, the Hamiltonian is:

$$\mathbf{H} \equiv \mathbf{H}_0 + \mathbf{V} \tag{1.1a}$$

$$\mathbf{H}_0 \equiv \sum_{\vec{\mathbf{k}},\sigma} \epsilon_{\vec{\mathbf{k}}} \mathbf{c}^\dagger_\sigma(\vec{\mathbf{k}}) \mathbf{c}_\sigma(\vec{\mathbf{k}}) \tag{1.1b}$$

$$\mathbf{V} \equiv -J \vec{\mathbf{S}} \cdot \vec{\mathbf{s}} \tag{1.1c}$$

$\mathbf{c}^\dagger_\sigma(\vec{\mathbf{k}})$ and $\mathbf{c}_\sigma(\vec{\mathbf{k}})$ respectively creates and annihilates an electron with momentum $\vec{\mathbf{k}}$ and spin σ. $\epsilon_{\vec{\mathbf{k}}}$ is the energy of a conduction electron of momentum $\vec{\mathbf{k}}$. $\vec{\mathbf{s}}$ is the average spin operator of the conduction electrons on the impurity. In second quantization, $\vec{\mathbf{s}}$ can be expanded in the basis of momenta to obtain:

$$\mathbf{V} \;=\; -J \sum_{\vec{\mathbf{k}}\vec{\mathbf{k}}'} \left[\mathbf{S}^+ \mathbf{c}^\dagger_\downarrow(\vec{\mathbf{k}}) \mathbf{c}_\uparrow(\vec{\mathbf{k}}') + \mathbf{S}^- \mathbf{c}^\dagger_\uparrow(\vec{\mathbf{k}}) \mathbf{c}_\downarrow(\vec{\mathbf{k}}') + \mathbf{S}_z \Big(\mathbf{c}^\dagger_\uparrow(\vec{\mathbf{k}}) \mathbf{c}_\uparrow(\vec{\mathbf{k}}') - \mathbf{c}^\dagger_\downarrow(\vec{\mathbf{k}}) \mathbf{c}_\downarrow(\vec{\mathbf{k}}') \Big) \right] \tag{1.2}$$

where $\mathbf{S}^\pm \equiv \mathbf{S}_x \pm i \mathbf{S}_y$ are the ladder spin operators and $\mathbf{S}_x$, $\mathbf{S}_y$ and $\mathbf{S}_z$ are the three spatial components of the impurity spin operator $\vec{\mathbf{S}}$. We will only consider the case $S = 1/2$. The derivation of this Hamiltonian can be found in appendix A.

For simplicity, we assume the conduction density of state $\rho(\omega) = \sum_{\vec{\mathbf{k}}} \delta(\hbar\omega - \epsilon_{\vec{\mathbf{k}}})$ to be constant, and the conduction band of half-width D to be centered on the Fermi level ϵ_F. The coupling strength J can be positive for a ferromagnetic coupling or negative for an antiferromagnetic coupling. However, the ferromagnetic coupling is irrelevant to the Kondo effect. The origin of the antiferromagnetic coupling is explained by the relation of the Kondo model with the Anderson impurity model, discussed in section 1.2.1. Only a single impurity is necessary in the model, as coupling between impurities is irrelevant to the Kondo effect.

In order to take into account the presence of several bands in the metal, Eq. 1.1 can be generalized into the N-channel Kondo model [27, 119]. A spin S is then coupled to not one but N independent free electron channels. In this work, we only consider a single channel.

Kondo's perturbation expansion in J

The conductivity σ in an isotropic metal with free electron dispersion relation is written in term of the scattering time $\tau(\epsilon)$ (for an electron of energy ϵ) as (see [64] Sec. 2.2):

$$\sigma = -\frac{4e^2}{3m} \int \tau(\epsilon) \epsilon \frac{\mathrm{d}n_\mathrm{F}}{\mathrm{d}\epsilon} \rho(\epsilon) \, \mathrm{d}\epsilon \tag{1.3}$$

where $\rho(\epsilon)$ is the density of states of electrons and n_F is the Fermi distribution [64].

The matrix element for scattering events which does not change the impurity spin — *e.g.* the scattering of an electron of momentum $\vec{\mathbf{k}}$ and spin $\uparrow$ into an electron of momentum $\vec{\mathbf{k}}'$ and spin $\uparrow$, while the impurity staid in a state $\downarrow$ — is simply J. In the first order perturbation theory in J, these are the only events considered. But Kondo included higher order contributions, where the impurity spin is flipped. For example, an electron of state $\vec{\mathbf{k}} \uparrow$ is scattered into an intermediary state $\vec{\mathbf{q}} \downarrow$, then into its final state $\vec{\mathbf{k}}' \uparrow$; while the impurity state goes as $\downarrow$ then $\uparrow$ then $\downarrow$. The matrix element is:

$$J^2 \int \frac{1 - n_\mathrm{F}(\epsilon_{\vec{\mathbf{q}}})}{\epsilon_{\vec{\mathbf{k}}} - \epsilon_{\vec{\mathbf{q}}}} \frac{\mathrm{d}^3 \vec{\mathbf{q}}}{(2\pi)^3} \tag{1.4}$$

which is independent of $\vec{\mathbf{k}}'$. The momentum integral is replaced by an energy integral. The contribution is then, with a constant density of state ρ:

$$J^2\rho \int_{\epsilon_\mathrm{F}-D}^{\epsilon_\mathrm{F}+D} \frac{1-n_\mathrm{F}(\epsilon)}{\epsilon_{\vec{\mathbf{k}}}-\epsilon}\,\mathrm{d}\epsilon \tag{1.5}$$

At zero temperature, the integral gives a logarithmic term, the contribution becomes:

$$J^2\rho \ln\left|\frac{\epsilon_{\vec{\mathbf{k}}}-\epsilon_\mathrm{F}}{\epsilon_{\vec{\mathbf{k}}}-\epsilon_\mathrm{F}-D}\right| \tag{1.6}$$

First and second order processes contributions are grouped by summing their matrix elements. The total scattering probability of an electron of momentum $\vec{\mathbf{k}}$ to any other state is obtained from the square of this sum. In an isotropic metal, this gives:

$$\frac{1}{\tau(\epsilon)} \propto J^2 + 2J^3\rho \ln\left|\frac{\epsilon-\epsilon_\mathrm{F}}{\epsilon-\epsilon_\mathrm{F}-D}\right| + \mathcal{O}\big(J^4\big) \tag{1.7}$$

We see that in this perturbative treatment, the scattering probability diverges for electrons near the Fermi level. One can expect that transport properties, which are mostly given by these electrons, are heavily affected at low temperature. Indeed, in the limit $k_\mathrm{B}T \ll D$ the resistivity $R = 1/\sigma$ is given, up to 3$^\mathrm{rd}$ order in J and neglecting terms proportional to J^3 but independant of T, by:

$$R = R_0\left(1 + 2J\rho \ln\left|\frac{k_\mathrm{B}T}{D}\right|\right) \tag{1.8}$$

with R_0 the resistivity caused by the first term in Eq. 1.7. Other 2$^\mathrm{nd}$ order processes have not been taken into account here, but some of them cancel and the others do not give a logarithmic term and are therefore negligible at low temperature.

In the antiferromagnetic case $J < 0$, the $\ln T$ term makes the resistivity increase when temperature is lowered, therefore explaining the resistance minimum. As mentioned above, the ferromagnetic case is physically irrelevant. The logarithmic term is caused by second order scattering processes involving a flip of the impurity spin. This demonstrates the many-body nature of the Kondo effect. Also, it shows that it relies on an internal (degenerate) degree of freedom of the impurity. The role of the Fermi level is explicit in Eq. 1.7: the Kondo effect especially enhances the scattering of electrons near the Fermi level.

Kondo's explanation is nevertheless unsatisfactory. At low temperatures the $\ln T$ term diverges, whereas the resistivity is expected to saturate when $T \to 0$. More advanced perturbative treatments in J show systematically a similar divergence [1], and are correct only for temperatures larger than some energy scale:

$$k_\mathrm{B}T_\mathrm{K} \equiv De^{-1/|J|\rho} \tag{1.9}$$

defining the Kondo temperature T_K. This problem is beyond the sole resistivity, most thermodynamic quantities (*e.g.* magnetic susceptibility, entropy, specific heat) diverge similarly, so that the whole description of the system is wrong in this limit. Looking for a correct description of an impurity at low temperature became to be known as the Kondo problem.

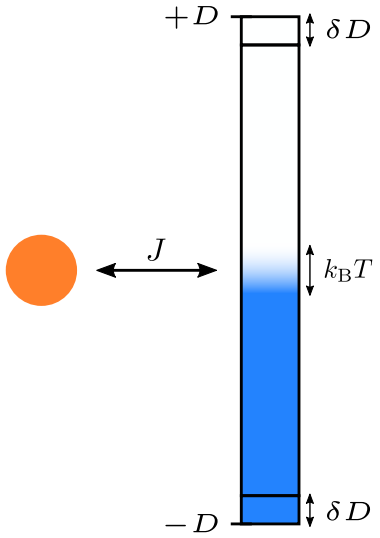

Figure 1.1: Scaling procedure. The impurity (left) is coupled to a continuum of energy levels (right) of bandwidth $2D$ filled with electrons (blue) up to the Fermi level. In the scaling procedure, we construct an effective Hamiltonian by integrating out the band edges δD.

1.1.2 Scaling arguments

To solve the Kondo problem, Anderson tried to apply a simple scaling argument [7], inspired by similar problems in high energy physics. In the end, his "poor man's scaling" did not bring a definitive solution, but offered a totally new way to consider the problem and new physical insights. This will give rise to the Numerical Renormalization Group method — which will finally solve the Kondo problem — and to the systematic application of renormalization group ideas in condensed matter physics.

Anderson's poor man's scaling

To start his scaling argument, Anderson [7] noticed that the origin of the logarithmic divergence are the high energy ends of the conduction band. His scaling argument consists in integrating out the high energy electron states to find an effective Hamiltonian which has the same form than the initial one, but different parameters. By continuing this process one reduces the effective bandwidth and changes continuously the parameters of the effective Hamiltonian. The parameters trajectory is described by a set of differential equations.

We remind that the conduction band is centered on the Fermi level and of half width D. The states in the infinitesimal energy ranges $[-D, -D + |\delta D|]$ and $[D - |\delta D|, D]$ ($|\delta D| \ll D$, see Fig. 1.1), lying at the edges of the band, are integrated out. This is possible because they are far from the Fermi level, so they are fully occupied by electrons or by holes. An effective Hamiltonian is found with the same form as the initial Hamiltonian Eq. 1.1, but with a renormalized interaction $J + \delta J$, with, to 2^{nd} order in J:

$$\delta J = 2J^2 \rho \frac{\delta D}{D} \tag{1.10}$$

Note that $\delta D < 0$ here. This gives the scaling equation:

$$\frac{\mathrm{d}J\rho}{\mathrm{d}\ln D} = 2(J\rho)^2 \tag{1.11}$$

The same calculation made up to 3^{rd} order in J gives:

$$\frac{\mathrm{d}J\rho}{\mathrm{d}\ln D} = 2(J\rho)^2 + 2(J\rho)^3 + \mathcal{O}\big((J\rho)^4\big) \tag{1.12}$$

From these first orders, one can assume that $\mathrm{d}J\rho/\mathrm{d}\ln D$ do not depend on D, and write:

$$\frac{\mathrm{d}J\rho}{\mathrm{d}\ln D} = \frac{1}{\Psi'(J\rho)} \tag{1.13}$$

where Ψ' is the derivative of some universal function Ψ, which is known perturbatively in the limit $|J\rho| \ll 1$.

By integrating this equation for a constant density of state, the initial problem with parameters (J, D) is mapped onto an effective model with new parameters $(\tilde{J}, \tilde{D})$, as long as the scaling procedure approximations are valid for these parameters. All models on the same trajectory are therefore equivalent concerning the low energy excitations. Also, the scaling equation possess an invariant quantity:

$$De^{-\Psi(J\rho)} = D|2J\rho|^{1/2}e^{1/(2J\rho)+\mathcal{O}(J\rho)} \sim k_\mathrm{B}T_\mathrm{K} \tag{1.14}$$

which is approximately the scale of temperature bellow which perturbation theory was failing in the preceding section. We can thus take this *scaling invariant* as a new definition of the Kondo temperature T_K. The consequence is important: in the regime of parameters where the model exhibits this scaling property, the low energy excitations are characterized by a single parameter T_K. The details of the model — the exact shape of the conduction band — do not play any role in Anderson's scaling argument. For this reason, the description of the Kondo effect is universal.

We can describe the trajectories in the weak coupling limit $|J\rho| \ll 1$. From the scaling equation 1.12 we note that J decreases strictly when the bandwidth D is reduced, except when $J = 0$ is reached. $J = 0$ corresponds to a fixed point, a point onto which trajectories are trapped. Ferromagnetic initial models with $J > 0$ all reach this fixed point for $\tilde{D} \to 0$. The effective model for these is free of interactions, and can therefore be solved easily. Antiferromagnetic initial models with $J < 0$ see their coupling increase in amplitude when bandwidth is reduced, until the scaling procedure breaks down. This happen when $\tilde{D}$ get down to $k_\mathrm{B}\max(T, T_\mathrm{K})$. Indeed, when the bandwidth get close to the temperature, the band edges are no longer fully filled or empty, and when it get close to the Kondo temperature, $\tilde{J}$ is not perturbative anymore.

Even though Anderson's scaling method could not solve the antiferromagnetic case — which is the physically interesting one — he provided a new way to look at the problem. He showed that the Kondo physics has a scaling property which allows to considerably reduce the effective bandwidth of the conduction electrons, and therefore to reduce the number of degrees of freedom needed to describe the low energy physics. By doing so, he showed the universality of the Kondo physics, reducing the parameters of the system to a single one, T_K. Hence, all thermodynamic quantities depend on T and T_K only.

What was missing was a way to continue the scaling procedure down for bandwidths smaller than the Kondo temperature. It was provided by Wilson's Numerical Renormalization Group method.

Numerical Renormalization Group method

The ideas of scaling — also called renormalization group — can be applied numerically. An iterative process would construct successive effective Hamiltonians by integrating out the higher energy levels of the conduction band. That is exactly the purpose of the Numerical Renormalization Group (NRG) method devised by Wilson [181]. A comprehensive review of NRG methods can be found in Ref. [19].

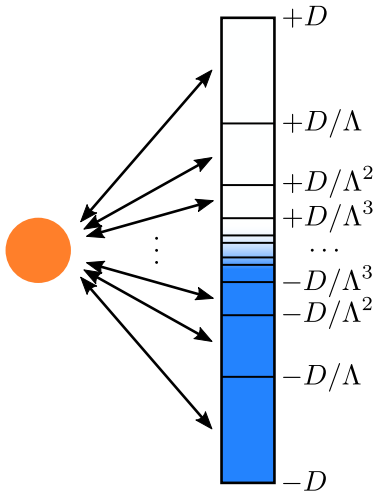

Figure 1.2: NRG scaling procedure. In NRG, the continuum is discretized logarithmically. Each slice is approximated by a single state coupled to the impurity. The scaling procedure consists in integrating out the discreet states from outer to inner band, thus constructing step-by-step an effective model.

To do this two things need to be added to Anderson's poor man's scaling. First, the spectrum of the conduction band has to be discretized, so that the band width can be reduced iteratively in a discreet number of steps. Second, a Hamiltonian model has to be designed to host the effective Hamiltonian on all energy scales. It should represent the impurity and the conduction band.

In NRG, the spectrum is discretized logarithmically. The density of state $\rho(\varepsilon)$, assumed zero outside the band $[-D, D]$, is approximated by discreet values $\rho(\pm\varepsilon_n)$ for $n \geq 0$, with:

$$\varepsilon_n = \frac{D}{\Lambda^n} \tag{1.15}$$

where $\Lambda > 1$ is a parameter (see Fig. 1.2). The n^{th} step in the iterative process is to reduce the effective conduction band spectrum from $[-\varepsilon_{n-1}, \varepsilon_{n-1}]$ to $[-\varepsilon_n, \varepsilon_n]$. The discretization introduces some error which depends on Λ, so the choice of Λ is important. A Λ close to 1 yields a thin discretization at all energies, close to a continuum. The error is small, but the number of steps to reach small energies is huge. A large Λ yields a larger error due to looser approximations in the spectrum, but small energies are faster to reach. $\Lambda \approx 2$ is usually considered a good compromise.

To fulfill the second requirement, the Kondo model is transformed in a semi-infinite linear chain model. The impurity lies at the end site of the chain, the conduction electrons are modeled by the rest of it. The chain is a tight-binding 1D Hamiltonian, with nearest-neighbour coupling γ_n between sites n and $n+1$. The hopping Hamiltonian between the impurity and its only neighbour is the terms in J in the Kondo model.

The NRG method consists in constructing the semi-infinite chain energy spectrum by adding sites one by one. Initially, the effective Hamiltonian is a two-site cluster containing the impurity site and the first site of the conduction electrons, and the bandwidth is D. The eigen-energies of the cluster are computed. The band largest (discreet) energy is integrated out to construct a new effective Hamiltonian. The effect is to split the eigen-energies of the impurity, which is accounted by adding a site. This process is iteratively reproduced. Importantly — and as a consequence of the logarithmic discretization — the hopping parameters γ_n decrease exponentially to zero at large n, so that the splittings are infinitely weak and the process converges. The number of eigen-energies in the spectrum grows exponentially in this iterative process, which is a problem for practical numerical implementation. To avoid that, only the N_s smaller ones are kept. The choice of N_s depends largely on the problem studied.

After n steps, a discreet spectrum is obtained. It is a good approximation of the infinite chain spectrum for a temperature close to the current bandwidth, *i.e.* D/Λ^n. The discreet spectrum get closer to a continuum when the bandwidth goes to zero, therefore the method provides more detailed information at low temperatures.

The NRG method allowed a satisfactory understanding of the Kondo effect. It showed that in the antiferromagnetic case, the effective coupling $\tilde{J}$ increases in magnitude infinitely when the bandwidth is reduced. Therefore, $J = -\infty$ forms another fixed point of the renormalization flow of the Kondo model, which entirely describes the Kondo physics at low energies.

With the NRG method, Wilson was able to give a satisfactory physical picture of the Kondo effect, giving to the Kondo temperature the status of emerging energy scale governing alone the low energy physics. In addition, near the strong coupling fixed point, this picture was well interpreted in terms of Fermi liquid [119].

Finally, this picture was systematically confirmed by an exact solution of the Kondo model found with a Bethe ansatz [9, 165, 179]. Surprisingly, this is independent from the results gathered around the Kondo problem by scaling arguments and Fermi liquid theory, so it provided a perfect validation of the previous theories and hypothesis.

1.2 The Kondo effect in quantum dots

A renewal of interest for the Kondo effect arose with the first use of the Scanning Tunneling Microscope (STM). Metallic surfaces could then be inspected on the atomic level, and single impurities could be observed and displaced at will [101]. This opened new possibilities for studying the Kondo effect. Before the STM, only macroscopic quantities such as resistance or magnetic susceptibility could be measured to infer the presence and effects of impurities.

But the STM manipulations were only a preview to what could be done a bit latter in nanoelectronics. Indeed, the improvements of industrial semiconductor technologies led to a new field where nanoscopic constructions are precise enough to accurately observe quantum effects. One of them is the quantum dot, a potential well that can contain one or several electrons. When connected to one or several leads, this is a powerful realization of the Anderson impurity model, and display the Kondo effect. In addition, it can also be driven out of equilibrium by applying a voltage bias between the leads. This led to vast possibilities in studying the interplay between the quantum many-body physics of the Kondo effect and the non-equilibrium properties of nanoelectronic devices.

1.2.1 Quantum dots: experiments and model

Experimental realizations

Quantum dots are zero dimensional nanoelectronic devices generally described as artificial atoms. They generally allow for precise experimental control. In a 2D Electron Gas (2DEG) formed at the interface of a GaAs/AlGaAs heterostructure, negative potentials can be applied with gates capacitively coupled to the electron gas, and constrain it in some region of the interface [28, 42, 43, 149]. As illustrated in Fig. 1.3, one can then form a small bounded area (the dot), connected by tunnel junctions to reservoirs (the leads). By adjusting gates voltages, one can tune the coupling between the leads and the dot or the charging energy of the dot. At equilibrium, the dot contains a precise number

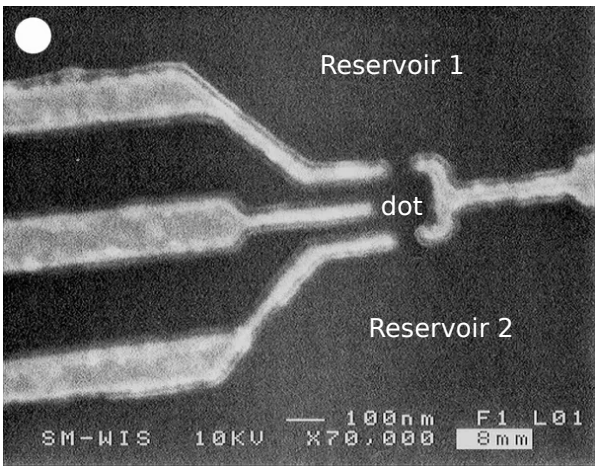

Figure 1.3: Scanning electron microscope top view of a 2DEG quantum dot. Adapted from Goldhaber-Gordon *et al.* [43]. Negative potential in the gates (light gray areas) repulse the 2DEG which is then confined in the black areas. The quantum dot (middle) is connected by tunnel junctions to two large reservoirs (top and bottom).

of electrons which can be changed at will by adjusting the charging energy with a gate voltage V_g. Coulomb repulsion between electrons is directly related to the radius of the dot, and therefore can be adjusted by design.

Other nanotechnologies can be used to build quantum dots or similar devices where the Kondo effect can be observed, such as carbon nanotubes [76, 120] or nanowires [88] bridging two electrodes. More recently, single molecules have been used as quantum dots, attached to two electrodes by electrostatic forces or deposited on a metallic surface [65]. In 2DEG, quantum rings also form quantum dots [81], allowing to use the magnetic flux through the ring as an extra control parameter. The more exotic N-channel Kondo effect have also been reproduced in single molecules [122, 137] as well as in a nanoelectronic device [73, 74].

The Anderson impurity model and its relation with the Kondo model

Quantum dots are well described by the Anderson impurity model [8]. We consider an empty dot. The leads form baths of conduction electrons. A first electron can enter the dot with a charging energy ϵ_d, and a second electron with charging energy $\epsilon_d + U$. $U \geq 0$ is the energy of the Coulomb repulsion between the two electrons. We neglect the possibility to bring more electrons in.

The Hamiltonian of this single orbital Anderson impurity model is made of a one-body part $\mathbf{H}_0$ and a Hubbard–like interaction part of strength U:

$$\mathbf{H} \equiv \mathbf{H}_0 + U\mathbf{n}_\uparrow\mathbf{n}_\downarrow \tag{1.16a}$$

$$\mathbf{H}_0 \equiv \mathbf{H}_{\text{bath}} + \mathbf{H}_{\text{bath–dot}} + \epsilon_d(\mathbf{n}_\uparrow + \mathbf{n}_\downarrow) \tag{1.16b}$$

$\mathbf{n}_\sigma$ are operators counting the number of electrons with spin σ in the dot. $\mathbf{H}_{\text{bath}}$ is the Hamiltonian of the leads and $\mathbf{H}_{\text{bath–dot}}$ of the coupling between the leads and the dot. For example, if the leads are modeled by semi-infinite tight-binding chains with

nearest-neighbour hopping:

$$\mathbf{H}_{\text{bath}} \equiv \sum_{\substack{i,j<0\\ \sigma}} (h_{ij}^{\text{L}} - \delta_{ij}\mu^{\text{L}})\mathbf{c}_{i\sigma}^{\dagger}\mathbf{c}_{j\sigma} + \sum_{\substack{i,j>0\\ \sigma}} (h_{ij}^{\text{R}} - \delta_{ij}\mu^{\text{R}})\mathbf{c}_{i\sigma}^{\dagger}\mathbf{c}_{j\sigma} \tag{1.17a}$$

$$\mathbf{H}_{\text{bath–dot}} \equiv \sum_{\sigma} \left(\gamma^{\text{L}}\mathbf{c}_{-1\sigma}^{\dagger}\mathbf{d}_{\sigma} + \gamma^{\text{R}}\mathbf{c}_{+1\sigma}^{\dagger}\mathbf{d}_{\sigma} + h.c.\right) \tag{1.17b}$$

$\mathbf{d}_{\sigma}^{\dagger}$ and $\mathbf{d}_{\sigma}$ creates and annihilates an electron with spin σ in the dot single orbital, such that $\mathbf{d}_{\sigma}^{\dagger}\mathbf{d}_{\sigma} \equiv \mathbf{n}_{\sigma}$. i and j are site indices, negative ones for the left lead and positive ones for the right lead. $\mathbf{h}^{\text{L}}$ and $\mathbf{h}^{\text{R}}$ are the non-interacting Hamiltonians of the left and right leads. Each lead is connected to a bath with different chemical potentials μ^{L}, μ^{R} and potentially different temperatures, although we will only consider equal temperatures. The difference in chemical potential is interpreted as a voltage bias between the leads $eV_{\text{b}} = \mu^{\text{L}} - \mu^{\text{R}}$. We neglect the dependence of the couplings γ on energy. This model is realized experimentally, thanks to quantum dots, with control over all its parameters. In the following, we are considering the large bandwidth limit $D \to +\infty$ for the leads electrons, with a constant density of states ρ^{L} and ρ^{R}.

At equilibrium, both leads have the same Fermi energy ϵ_{F} and can be considered as a single continuum. In the limit of no coupling between the interacting dot and the conduction electrons $\Gamma \sim 0$, we can distinguish different low temperature regimes. If $\epsilon_d < \epsilon_F$ and $\epsilon_d + U > \epsilon_F$, there is a single electron on the dot. Charge fluctuations are small so that the ground state has a local magnetic moment. It is also two-fold degenerate due to spin symmetry. It can be shown, using a Schrieffer–Wolff transformation [155], that up to 1$^{\text{st}}$ order in Γ and if $\epsilon_F - \epsilon_d \gg \Gamma$ and $\epsilon_d + U - \epsilon_F \gg \Gamma$, that this model is equivalent to a spin 1/2 Kondo model with an antiferromagnetic coupling $J\rho = U\Gamma/(\epsilon_d - \epsilon_{\text{F}})(\epsilon_d + U - \epsilon_{\text{F}})$ with conduction electrons near the Fermi level. The dot is equivalent to the impurity. This is called the local moment regime.

The Anderson impurity model was originally used as a microscopic model to understand the origin of the antiferromagnetic coupling in magnetic impurities [8]. As it was understood, this origin is the Coulomb repulsion between electrons in the same orbital. The Schrieffer–Wolff transformation definitely proves that the ferromagnetic Kondo model is irrelevant to the Kondo physics.

In the case where the charging energy of the first or the second electron is close to the Fermi level, charge fluctuations are much more important. The equivalence with the Kondo model breaks down. This is the mixed valence regime. Finally, if the charging energy of both electrons are above (respectively below) the Fermi level, two holes (resp. electrons) occupy the impurity. The ground state is non magnetic and non degenerate. This regime is less interesting than the previous ones, and will not be considered.

1.2.2 The Kondo effect in the Anderson impurity model

First, it is important to note that this two-terminal Anderson model is not related to a 2-channel Kondo model. The two baths are separate, but not independent: electrons can move from one to the other through the dot [126].

The Anderson impurity model has been studied at equilibrium using the same tools as were used for the Kondo model: perturbation theory in powers of U [68, 183, 184], the poor man's scaling method [52], Fermi liquid theory [63] and Bethe ansatz [78, 180]. Numerical methods were also extensively used, for both studying the Kondo physics and

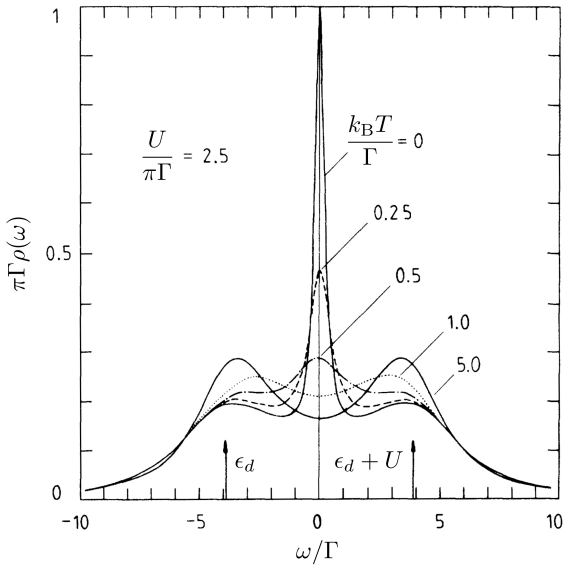

Figure 1.4: Evolution of the density of states as temperature is lowered in a particle-hole symmetric Anderson impurity model. Adapted from Horvatić *et al.* [68]. At large temperature, there are two resonances near each charging energy of the dot ϵ_d and $\epsilon_d + U$ (vertical arrows). When temperature goes below the Kondo temperature, the Kondo peak develops at the Fermi level.

constructing impurity solvers for quantum embedding studies of *e.g.* the Hubbard model. This of course includes NRG methods [18, 19, 123], but also Monte Carlo algorithms [45], such as the historic Hirsh-Fye algorithm [66] and the many so-called "continuous time" methods that followed [44, 144, 145, 173].

At equilibrium, the low energy properties of the two-terminal quantum dot are the same as the classic magnetic impurity in a metal. Deep into the local moment regime, *i.e.* when ϵ_d is well below the Fermi energy and correlations U are strong, the Kondo temperature is the only energy scale at low temperature. It can be written in terms of the parameters of the model [52, 90] as:

$$k_B T_K \approx \sqrt{\frac{\Gamma U}{\pi}} \exp\left(\frac{\pi^2 \epsilon_d}{2\Gamma}\right) \tag{1.18}$$

The complete spectrum of the Anderson impurity model at equilibrium has been computed by NRG [89, 90] and Bethe ansatz [68], in the same way as for the Kondo model. Coherent spin-flip scattering forms a Kondo resonance at the Fermi level of width $\sim T_K$, as illustrates in Fig. 1.4. Increasing U and decreasing ϵ_d reduces the charge fluctuations, brings the system deeper into the local moment regime and reduces the width of the Kondo peak. While the Kondo resonance get thinner, its spectral weight is transferred toward broader resonances centered on ϵ_d and $\epsilon_d + U$. These are named lower and upper Hubbard bands, and are associated to simple atomic excitations of the quantum dot.

We have seen that, in the Kondo regime, the low energy properties of the quantum dot are the same as in the impurity in a metal. Nevertheless, transport properties are affected by the Kondo physics in absolutely different ways.

1.2.3 Quantum dots under a voltage bias

Quantum dots driven out of equilibrium with a voltage bias represent simple nanoelectronics experiments. Surprisingly, simple measures of their conductance can display signatures of various physical effects. The most striking are the Coulomb blockade and the Kondo effect. Reviews related to transport in quantum dots can be found in Ref. [3, 133].

Suppression of conductance by Coulomb blockade

Before the Kondo effect, the first effect of Coulomb interaction which has been observed in quantum dots is the Coulomb blockade [2]. Quantum dots can be seen as artificial atoms, made of electronic orbitals which are increasingly separated in energy when Coulomb repulsion get stronger. Under a voltage bias V_b, the current trough the dot I is proportional to the number of levels between the chemical potentials of the leads. As a result, the current may be heavily suppressed by Coulomb repulsion depending on the on-site energy of the dot. In the limit $V_\mathrm{b} \sim 0$ and at zero temperature, the conductance $G = I/V_\mathrm{b}$ is globally zero as a function of gate voltage V_g, but overcomes sharp peaks whenever a level is inside the voltage bias window. Another typical signature is obtained by extending conductance measurements along the V_b axis. Coulomb diamonds are observed: diamond-shape areas aligned along the zero bias axis where G is suppressed.

Electronic spins are irrelevant to Coulomb blockade, but not to the Kondo effect. In quantum dot with particularly strong interaction, the spin degree of freedom of the dot electrons can build a Kondo effect on top of the Coulomb blockade.

Enhancement of conductance by Kondo effect: the zero bias anomaly

The principal difference between quantum dots and impurities in a metal is that dots (with their leads) are 1D systems while metals are 2D or 3D. A surprising consequence is that, in quantum dots, the Kondo effect enhances the *conduction* instead of the resistance at low temperature [41, 114, 133]. At zero temperature, the conductance even reach its maximum possible value in quantum mechanics $2e^2/h$. This can be understood from the fact that in 2D or 3D systems scattering can bring the electrons motion in many more directions than in 1D, where there are only two possibilities.

As a result, dots with an odd number of electrons — this is required for a magnetic moment to exist — see their conductance increase when temperature is lowered; whereas dots with an even number of electrons do not, because they lack the internal degree of freedom necessary for the Kondo effect. The zero-bias conductance then shows a temperature dependence as displayed in the upper panel of Fig. 1.5. At large temperature (red line), the conductance is peaked when an energy level is close to the chemical potential of the leads, as explained by Coulomb blockade alone. In the valleys between these peaks an integer number of electrons are in the dot. When temperature is decreased, valleys with an odd number of electrons enter the Kondo regime and see their conductance increase (blue lines). The universality of the Kondo regime can be observed here, as the conductance at zero bias is a universal function of T/T_K.

Assuming the Kondo temperature is small compared to the separation of the levels in energy ΔE, the conductance reaches a maximum at zero temperature $T = 0$, then is suppressed for $k_\mathrm{B}T_\mathrm{K} \ll k_\mathrm{B}T \ll \Delta E$. It increases again when $k_\mathrm{B}T \sim \Delta E$, as thermal energy is enough to overcome the charging energy of a new electron in the dot. The

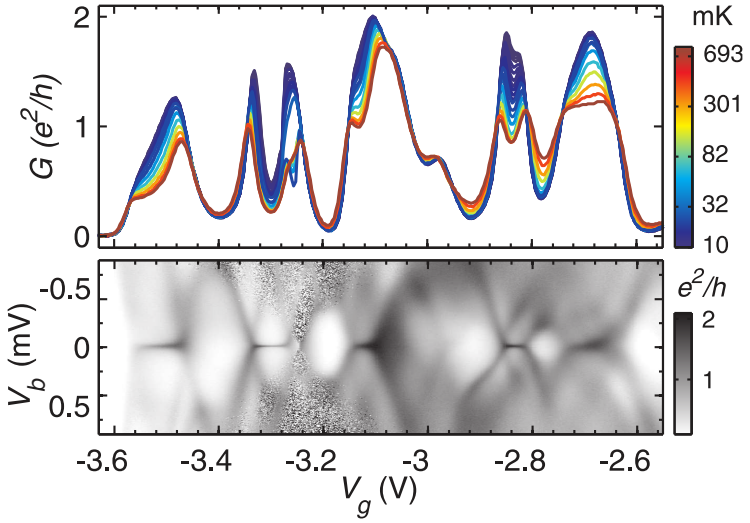

Figure 1.5: Signature of the Kondo effect in the conductance through a quantum dot. Adapted from Kretinin *et al.* [88]. Upper panel: at high temperature, the conductance as a function of gate voltage shows typical oscillations caused by Coulomb blockade (red line). At low temperature, the Kondo effect manifest itself by an enhancement of conductance in valleys with an odd number of electrons. Lower panel: conductance as a function of voltage bias and gate voltage. The zero bias anomaly forms ridges along $V_\mathrm{b} = 0$ across Coulomb diamonds with an odd number of electrons.

conductance therefore observes a minimum in temperature [133], which can be though of an analogue of the minimum of resistance caused by the Kondo effect in higher dimension.

As a function of voltage bias V_b, and in the limit $k_\mathrm{B}T \ll eV_\mathrm{b}$, the conductance forms a peak of width $\sim T_\mathrm{K}$ centered on zero bias. This so-called zero bias anomaly is shown in the bottom panel of Fig. 1.5, and appears as ridges of high conductance crossing the odd Coulomb diamonds on the zero bias axis. Away from these ridges, the transport is mostly led by Coulomb blockade. The Kondo effect is therefore killed by voltage bias, in the same manner that it is killed by temperature.

Splitting of the Kondo peak at large V_b

The effect of the Kondo regime on transport properties can be understood from the presence of the Kondo resonance in the one-body spectrum of the dot. The Landauer–Buttiker formula — expressing the current through a non-interacting region connected to leads as a function of local properties of the region and the distribution functions in the leads — can indeed be extended to interacting regions [102]. For the Anderson impurity model at zero temperature, the current is proportional to the spectral weight between the Fermi levels of the two leads. In the Kondo regime, this current is maximal, as long as $eV_\mathrm{b} \ll k_\mathrm{B}T_\mathrm{K}$. When voltage bias is increased, the spectral weight within the bias window has to collapse, so it is expected that the Kondo peak disappear.

Many theoretical works based on perturbation theory and scaling arguments [38, 103, 138], equation of motion approach [169, 170] as well as Non-Crossing Approximation (NCA) calculations [182] predicted a splitting of the Kondo peak into two smaller and broader resonances centered on $\pm eV_\mathrm{b}$. In presence of two Fermi levels, a Kondo reso-

nance forms at each of them. However, they are weakened by non-equilibrium incoherent scattering: real transitions between the two leads give a finite lifetime to any state on the dot, therefore broadening all features of the spectrum [182]. Nevertheless, a few theoretical works did not conclude with a splitting [111]. Unlike measurement of conductance, experimental observation of the non-equilibrium density of state is challenging, but the splitting of the Kondo peak has been observed in the conductance through a weakly connected third lead, used as a probe to the density of states [30, 96].

1.2.4 Numerical tools for the non-equilibrium Anderson impurity model

The Kondo problem at equilibrium has been considered a key step to understand fermionic quantum many-body physics. Similarly, the two-terminal Anderson impurity model is a typical model to test ideas and algorithms for solving non-equilibrium quantum many-body physics. Unfortunately, analytical tools that were successful in the equilibrium model do not provide systematic ways out of equilibrium. However, a lot of energy is currently spent in developing numerical algorithms for the non-equilibrium many-body problem. Many of these methods computes the evolution of quenched systems: the system is first prepared with a simple Hamiltonian, then it is switched to a more complex one. The relaxation of the system toward a steady state is observed. In that sense, most of the following solvers computes the *real time* dynamics.

The ideas of renormalization group, which were successful in solving the Kondo problem, have been naturally extended to the non-equilibrium impurity. The NRG method has been extended to time-dependent impurity Hamiltonians [5, 6] as well as to transport through open systems [4]. Similar developments have been realized with DMRG [29, 60, 156, 178]. A perturbative real-time renormalization group method [80, 152] and a flow equation method [171] have also been used. The ideas of Functional Renormalization Group (FRG), which have already been applied to compute the equilibrium Anderson impurity model spectrum [59], have been upgraded to non-equilibrium and transport properties [75, 150].

Apart from the renormalization group ideas, methods based on the hierarchy of equation of motions in the real-time formalism [57, 185], as well as a variationnal approach using a time-dependant Gutzwiller wavefunction ansatz [95, 148] have also been used.

Most other numerical solutions rely on Monte Carlo algorithms. Early methods were inspired from "continuous-time" diagrammatic Quantum Monte Carlo (QMC) already used in equilibrium in the Matsubara formalism. The CT-HYB method [173] — based on a perturbative expansion in the hybridization term with the bath — was extended to real time [92, 111, 112, 146, 147, 151, 175]. The same development was made for its weak coupling counter-part CT-AUX [33, 82, 174, 175] — which uses auxiliary fields in a perturbative expansion in the interaction [44]. Both methods compute the evolution of a quenched Hamiltonian and tries to reach the steady state. However, they are limited by a strong "dynamical" sign problem at large times. A more marginal approach was to stay in the Matsubara formalism by using imaginary voltages [54, 55].

Path integral methods have not been very popular for fermionic systems, although real-time path integral Monte Carlo methods have been designed for equilibrium many-body problems [100, 110], inspired by a large field of research in chemistry [17]. We note however that a deterministic iterative summation of path integrals [172] has been applied to transport in the Anderson impurity model [36, 158]. Several works made quantitative

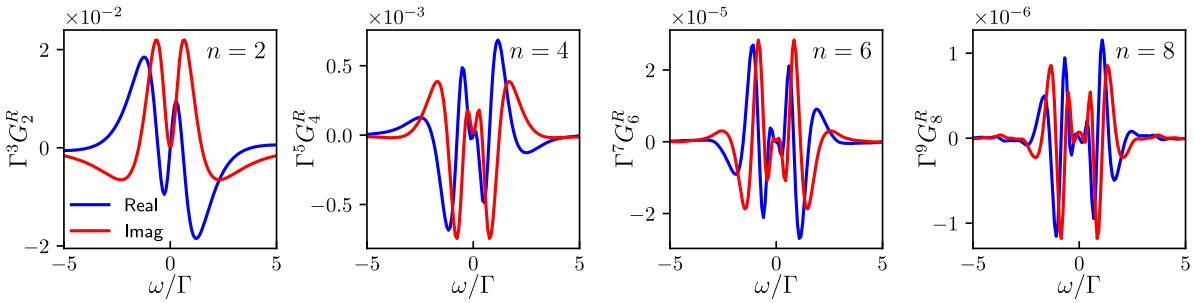

Figure 1.6: Typical result after a single run of the real-time QMC developed in this thesis: a perturbation series for the Green's function in the frequency domain. n is the perturbation order and Γ an energy unit. This data is for the particle-hole symmetric Anderson impurity model, details of the application are in chapter 5.

comparison between some of the above-mentioned methods [33, 36].

More recently, the inchworm algorithm was developed to deal with the dynamical sign problem [11, 12, 21, 22, 24–26, 47, 91, 135]. The central idea is to recycle the Monte Carlo information obtained at earlier times to reduce the scaling of computational cost with time from exponential to quadratic.

Another QMC approach, which is the basis of this thesis, consists in evaluating the perturbative expansion in the interaction, but with a careful Monte Carlo sampling to treat cancelling terms explicitly [128]. In this thesis, we developed an optimized version of this algorithm to compute physical quantities directly on a wide time range. Our QMC method yields perturbation series as function of time. We show in Fig. 1.6 a typical perturbation series, output of a single run of our QMC, after Fourier transform. To understand how to obtain such results, we have to present the real-time Schwinger–Keldysh formalism, and to introduce the kernels of Green's functions, which provide the way to compute a quantity over a full time range in a single QMC run. This is the purpose of the next chapter.

Chapter 2

Green's functions and kernels in the Keldysh formalism

The QMC algorithm developed in this thesis rely on the real-time (or Schwinger–Keldysh) formalism [134]. In the first part of this chapter we explain how this formalism allows to construct time-dependant observables and correlation functions as sums of Feynman diagrams. The diagrams, once regrouped into determinants, are the basis of the QMC algorithm.

In a second part, we introduce the kernels. These are the correlation functions actually computed by our QMC. They contains all information necessary to reconstruct — with a simple convolution — the Green's functions on a wide time-range, yielding physical quantities in the frequency domain by Fourier transform. Computing the kernels, and not the Green's function as in Ref. [128], is an important optimization. It avoids to run multiple independent Monte Carlos to sample the Green's functions along a time interval.

Readers who wish to jump straight to the final formulas are redirected to the final section of the chapter, page 43, which contains a summary of the formulas of interest for the practical calculation of the Green's function from the kernels.

In all this chapter, and the following ones, we use $\hbar = 1$.

2.1 Perturbation theory in the real-time formalism

The real-time formalism allows to compute time-dependant quantities of an interacting system through a perturbative expansion of the quantity of interest in powers of the interaction strength U. As in the imaginary time formalism, each coefficient is expressed as a sum of Feynman diagrams whose contributions are easily computed from correlation functions of the non-interacting problem. Its specificity is to write this expansion not on a single time axis, but on a closed-path time contour — first going forward in time, then backward. We develop this idea here by applying it to Green's functions.

2.1.1 Perturbation series of Green's functions

Consider a generic time-independent fermionic one-body problem:

$$\mathbf{H}_0 \equiv \sum_{xy} h_{xy} \mathbf{c}_x^\dagger \mathbf{c}_y \tag{2.1}$$

The indices x and y identify sites, orbitals, spins, or a combination of these depending on the problem. They will simply be called orbital indices. $\mathbf{c}^\dagger$ and $\mathbf{c}$ are fermionic creation and annihilation operators. On top of this, an interacting (possibly time-dependent) Hamiltonian is added:

$$\mathbf{H}(t) \equiv \mathbf{H}_0 + U\mathbf{H}_{\text{int}}(t) \tag{2.2}$$

$$\mathbf{H}_{\text{int}}(t) \equiv \sum_{xx'yy'} V_{xx'yy'}(t)\mathbf{c}_x^\dagger \mathbf{c}_{x'}\mathbf{c}_y^\dagger \mathbf{c}_{y'} \tag{2.3}$$

where U is the interaction strength. Like in any diagrammatic formalism, we assume $\mathbf{H}_0$ solved. This means that any physical quantity corresponding to $\mathbf{H}_0$ are known. We are interested in computing the Green's functions of the full problem $\mathbf{H}(t)$ from the Greens functions of $\mathbf{H}_0$.

The global idea of the formalism [134] is to expand the full propagator $\mathbf{U}(t)$ — which propagates a state from time 0 to time t under the influence of $\mathbf{H}$ — in powers of the interaction strength U, to apply it to an initial state represented by a density matrix $\boldsymbol{\rho}$, and then use Wick's theorem to write the series coefficients in term of the non-interacting Green's functions and V . However, to apply Wick's theorem, the density matrix should represent a thermal state of a non-interacting Hamiltonian. Such a choice would not be physical if $\mathbf{H}(t = 0)$ is interacting. To go around this obstacle, we start from $\mathbf{H}(t < 0) = \mathbf{H}_0$ and switch on interactions at $t = 0$. We then wait for the relaxation of the system.

If the unperturbed system is coupled to a thermal bath, and if it is free of bound states, the long time behavior of the perturbed system is agnostic from the exact way the interaction has been switched on, be it abruptly or adiabatically. If, in addition, the interaction $V(t)$ is constant after being switched on, then a stationary state is reached at long time. In a nanoelectronic device such as a quantum dot, interactions are often modeled only on a finite portion of the system, which is connected to non-interacting baths (the leads). In that case, the stationary state obtained after switching on interactions is the same as the state of a forever interacting system. The formalism developed in this chapter is therefore limited to systems coupled to non-interacting baths only, and we are interested only in these in this thesis. Nevertheless, an extended formalism exists to manage interacting baths, based on a three-branch time contour (see *e.g.* Ref. [134] Sec. 4.3).

Evolution along the Schwinger–Keldysh time contour

Suppose one wants to compute the following correlator:

$$G^<_{xx'}(t, t') \equiv i \left\langle \mathbf{c}_{x'}^\dagger(t')\mathbf{c}_x(t) \right\rangle \tag{2.4}$$

Creation and annihilation operators are in the Heisenberg picture. The quantum average $\langle \ldots \rangle$ is obtained form the density matrix $\boldsymbol{\rho}$ through $\langle \mathbf{A} \rangle \equiv \text{Tr}(\boldsymbol{\rho}\mathbf{A})$. This correlator is called lesser Green's function. Its relevance and relation to more common quantities is discussed in section 2.1.2, it is only used here as an example for the derivation. The result obtained in this section will be generalized to a large class of correlators in section 2.1.3.

To compute $\mathbf{G}^<$, for instance, we express it in the interaction picture:

$$G^<_{xx'}(t, t') = i \left\langle \tilde{\mathbf{U}}(0, t')\tilde{\mathbf{c}}_{x'}^\dagger(t')\tilde{\mathbf{U}}(t', t)\tilde{\mathbf{c}}_x(t)\tilde{\mathbf{U}}(t, 0) \right\rangle \tag{2.5}$$

$\tilde{\mathbf{c}}^\dagger$ and $\tilde{\mathbf{c}}$ are creation and annihilation operators in the interaction picture, and $\tilde{\mathbf{U}}(u,v)$ is the interaction picture propagator, which relates to the non-interacting propagator $\mathbf{U}_0$ and the full propagator $\mathbf{U}$ through $\tilde{\mathbf{U}}(u,v) \equiv \mathbf{U}_0^\dagger(u)\mathbf{U}(u,v)\mathbf{U}_0(v)$.

In Eq. 2.5, the initial state is propagated to time t, where $\tilde{\mathbf{c}}_x(t)$ is applied, then to time t', where $\tilde{\mathbf{c}}_{x'}^\dagger(t')$ is applied, before being propagated back to time 0, where it is projected onto its original value. Keldysh described this motion on a closed-path contour in time [79]. As illustrated in Fig. 2.1, the contour has a forward branch $0 \to t_\mathrm{M} \equiv \max(t,t')$, and a backward branch $t_\mathrm{M} \to 0$. Note that t_M can be extended anywhere further than t or t', even to infinity, simply because $\tilde{\mathbf{U}}(t',t) = \tilde{\mathbf{U}}(t',+\infty)\tilde{\mathbf{U}}(+\infty,t)$.

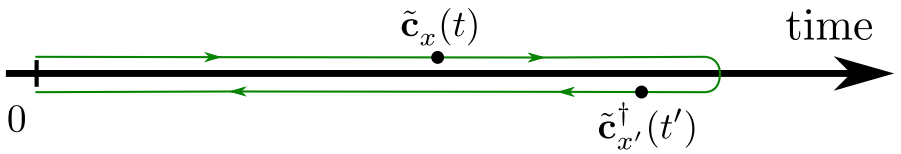

Figure 2.1: The closed-path Schwinger–Keldysh time contour, here with $t' > t$. It starts and ends at time 0, where interactions have been switched on. The contour can be extended to times arbitrary larger then t and t', but for simplicity it is taken as small as possible, *i.e.* the turning point at $t_\mathrm{M} \equiv \max(t,t')$.

The interaction Hamiltonian has been isolated in the propagators $\tilde{\mathbf{U}}$. As we aim at expanding $G^<_{xx'}$ in powers of the interaction strength U, we need a way to regroup them. A time-ordering operator can be used to grant the possibility to (anti)commute the time-dependent $\tilde{\mathbf{c}}^\dagger$ and $\tilde{\mathbf{c}}$. But here, it is most natural to order operators along the two-branch contour, rather than along a single time-line. We thus define the contour time-ordering operator T^c, which regroups operators of the forward branch on the right-hand side, of the backward branch on the left-hand side, and which time-orders operators within the forward branch, and anti-time-orders those within the backward branch. As usual with time ordering, a -1 factor is introduced whenever two fermionic operators are swapped. The order of operators lying at the same point on the contour is kept unchanged from Eq. 2.5. The lesser Green's function then reads:

$$G^<_{xx'}(t,t') = i\left\langle T^\mathrm{c}\tilde{\mathbf{c}}_{x'}^\dagger(t')\tilde{\mathbf{c}}_x(t)\exp\left(-iU\int_\mathrm{c}\tilde{\mathbf{H}}_\mathrm{int}(u)\,\mathrm{d}u\right)\right\rangle \tag{2.6}$$

The propagator $\tilde{\mathbf{U}}$ has been written explicitly as a function of the interaction Hamiltonian in the interaction picture $\tilde{\mathbf{H}}_\mathrm{int}(u) \equiv \mathbf{U}_0^\dagger(u)\mathbf{H}_\mathrm{int}(u)\mathbf{U}_0(u)$. The contour integral is the sum of both branches integrals:

$$\int_\mathrm{c}\tilde{\mathbf{H}}_\mathrm{int}(u)\,\mathrm{d}u \equiv \int_0^{t_\mathrm{M}}\tilde{\mathbf{H}}_\mathrm{int}(u)\,\mathrm{d}u + \int_{t_\mathrm{M}}^0\tilde{\mathbf{H}}_\mathrm{int}(u)\,\mathrm{d}u \tag{2.7}$$

$$= \int_0^{t_\mathrm{M}}\tilde{\mathbf{H}}_\mathrm{int}(u)\,\mathrm{d}u - \int_0^{t_\mathrm{M}}\tilde{\mathbf{H}}_\mathrm{int}(u)\,\mathrm{d}u \tag{2.8}$$

Obviously, cancellations are prohibited by the ordering operator.

By expanding the exponential in its Taylor series, and by using Eq. 2.7, we obtain:

$$G^<_{xx'}(t,t') = i\sum_{n\geq 0}\frac{(-iU)^n}{n!}\int_0^{t_\mathrm{M}}\sum_{\{a_k\}}\prod_{k=1}^{n}[(-1)^{a_k}\,\mathrm{d}u_k] \quad \times$$
$$\left\langle T^\mathrm{c}\tilde{\mathbf{c}}_{x'}^\dagger(t')\tilde{\mathbf{c}}_x(t)\tilde{\mathbf{H}}_\mathrm{int}(u_1,a_1)\ldots\tilde{\mathbf{H}}_\mathrm{int}(u_n,a_n)\right\rangle \tag{2.9}$$

For a given set of times $u_1, \dots, u_n$, the $\tilde{\mathbf{H}}_{\text{int}}$ operators can be distributed between the forward and the backward branch in 2^n ways. For example, one of the contributions is shown in Fig. 2.2. a_k is 0 if $\tilde{\mathbf{H}}_{\text{int}}(u_k)$ is on the forward branch, 1 if on the backward branch. Note we introduced a_k in the parameters of $\tilde{\mathbf{H}}_{\text{int}}$ in order to keep track of which operator is on which branch, but its value does not depend on a_k. The sum over these $\{a_k\}$ — which we name Keldysh indices — account for these 2^n possibilities. Each $\tilde{\mathbf{H}}_{\text{int}}$ on the backward branch brings a -1 factor, which is at the origin of the $(-1)^{a_k}$.

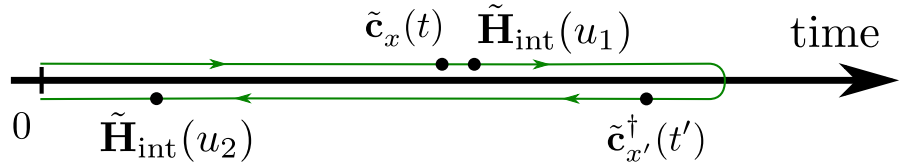

Figure 2.2: Representation on the contour of a contribution to $G^<_{xx'}(t,t')$ at order $n = 2$, with $u_1 > u_2$, $a_1 = 0$ (forward branch) and $a_2 = 1$ (backward branch).

Expression with Wick determinants

The next step is to expand the interaction Hamiltonian. For simplicity, we assume a density-density interaction:

$$\mathbf{H}_{\text{int}}(t) \equiv \sum_{xy} V_{xy}(t) \mathbf{c}^\dagger_x \mathbf{c}_x \mathbf{c}^\dagger_y \mathbf{c}_y \tag{2.10}$$

and without loss of generality we assume $V_{xy} = V_{yx}$. The following derivation is nevertheless easy to generalize to a generic interacting Hamiltonian such as Eq. 2.3.

Before going on, we introduce additional notations for clarity. We call a Keldysh point $X \equiv (x, t, a)$ the gathering of an orbital index x, a time t and a Keldysh index $a \in \{0, 1\}$. Using this, we can simply replace $\tilde{\mathbf{c}}^\dagger(X) \equiv \tilde{\mathbf{c}}^\dagger_x(t, a)$ and $\tilde{\mathbf{c}}(X) \equiv \tilde{\mathbf{c}}_x(t, a)$. Thus, using Eq. 2.10, the expression 2.9 becomes:

$$G^<_{xx'}(t,t') = i \sum_{n\geq 0} \frac{(-iU)^n}{n!} \int_0^{t_{\text{M}}} \sum_{\{a_k\}} \sum_{\{x_k, y_k\}} \prod_{k=1}^{n} [(-1)^{a_k} V_{x_k y_k}(u_k)\, \mathrm{d}u_k] \quad \times \\ \left\langle T^{\text{c}} \tilde{\mathbf{c}}^\dagger(X') \tilde{\mathbf{c}}(X) \tilde{\mathbf{c}}^\dagger(U_1) \tilde{\mathbf{c}}(U_1) \dots \tilde{\mathbf{c}}^\dagger(U_{2n}) \tilde{\mathbf{c}}(U_{2n}) \right\rangle \tag{2.11}$$

$U_1, \dots, U_{2n}$ are Keldysh points, which are defined for $1 \leq k \leq n$ as:

$$U_{2k-1} \equiv (x_k, u_k, a_k) \tag{2.12}$$
$$U_{2k} \equiv (y_k, u_k, a_k) \tag{2.13}$$

We also defined $X \equiv (x, t, 0)$ and $X' \equiv (x', t', 1)$. These notations are illustrated on the time contour in Fig. 2.3.

The quantum average in Eq. 2.11 is a *non-interacting* $(2n + 1)$-particles correlator. Wick's theorem will transform it into products of 1-particle correlators if the density matrix $\boldsymbol{\rho}$ represents a thermal state of a one-body Hamiltonian [39, 134]. For this reason, we choose the initial state to be a thermal state of $\mathbf{H}_0$ of temperature $k_{\text{B}}T \equiv 1/\beta$:

$$\boldsymbol{\rho} \equiv \frac{e^{-\beta \mathbf{H}_0}}{\text{Tr}(e^{-\beta \mathbf{H}_0})} \tag{2.14}$$

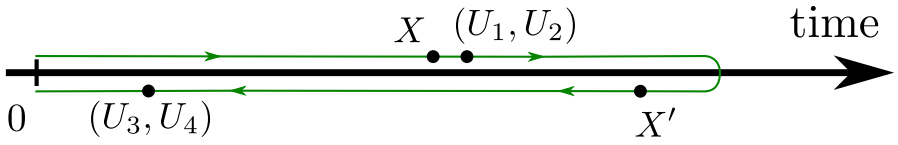

Figure 2.3: Same contribution as in Fig. 2.2 after expending the interaction Hamiltonian, and using the Keldysh point notations.

Note that Wick's theorem is slightly more general. It holds also for systems made of different baths with different chemical potentials and temperatures, where $\boldsymbol{\rho}$ represents the juxtaposition (tensor product) of thermal states of each bath [134]. This is typically applied in the two-terminal Anderson impurity model.

The application of Wick's theorem yields 1-particle correlators of the form $\left\langle T^{\mathrm{c}} \tilde{\mathbf{c}}^\dagger(A) \tilde{\mathbf{c}}(B) \right\rangle$ with A and B two Keldysh points. They are known exactly from the solution of the $\mathbf{H}_0$ problem, but cannot be simply related to the non-interacting retarded Green's function. Hence, we define a generalized Green's function which is specific to the real-time formalism. The Keldysh Green's function is defined for two Keldysh points $X \equiv (x, t, a)$ and $X' \equiv (x', t', a')$ as:

$$G(X, X') \equiv -i \left\langle T^{\mathrm{c}} \mathbf{c}(X) \mathbf{c}^\dagger(X') \right\rangle \tag{2.15}$$

where $\mathbf{c}$ and $\mathbf{c}^\dagger$ are in the Heisenberg picture. We use alternatively different notations:

$$G(X, X') \equiv G[(x, t, a), (x', t', a')] \equiv G^{aa'}_{xx'}(t, t') \tag{2.16}$$

As a result, the non-interacting Keldysh Green's functions read:

$$g(X, X') \equiv -i \left\langle T^{\mathrm{c}} \tilde{\mathbf{c}}(X) \tilde{\mathbf{c}}^\dagger(X') \right\rangle \tag{2.17}$$

Similar notations as 2.16 are used for g. We choose to apply Wick's theorem in its determinantal form, which gives:

$$\left\langle T^{\mathrm{c}} \tilde{\mathbf{c}}^\dagger(X') \tilde{\mathbf{c}}(X) \tilde{\mathbf{c}}^\dagger(U_1) \dots \tilde{\mathbf{c}}(U_{2n}) \right\rangle = -i^{2n+1} \begin{vmatrix} g(X, X') & g(X, U_1) & \dots & g(X, U_{2n}) \\ g(U_1, X') & g(U_1, U_1) & \dots & g(U_1, U_{2n}) \\ \vdots & \vdots & \ddots & \vdots \\ g(U_{2n}, X') & g(U_{2n}, U_1) & \dots & g(U_{2n}, U_{2n}) \end{vmatrix} \tag{2.18}$$

Note that definition 2.15 is ambiguous regarding equal time operators. The order of operators in the Hamiltonian 2.10 should be conserved to lift this ambiguity, explicitly:

$$g(U_{2k}, U_{2k}) = g^{01}_{y_k y_k}(u_k, u_k) \tag{2.19a}$$
$$g(U_{2k-1}, U_{2k-1}) = g^{01}_{x_k x_k}(u_k, u_k) \tag{2.19b}$$
$$g(U_{2k-1}, U_{2k}) = g^{10}_{x_k y_k}(u_k, u_k) \tag{2.19c}$$
$$g(U_{2k}, U_{2k-1}) = g^{01}_{y_k x_k}(u_k, u_k) \tag{2.19d}$$

To simplify notations, we will again introduce a new notation. For any Keldysh points $A_1, \dots, A_m$ and $B_1, \dots, B_m$, we define the *Wick determinant*:

$$\left[\!\!\left[\begin{matrix} A_1, \dots, A_m \\ B_1, \dots, B_m \end{matrix} \right]\!\!\right] \equiv \begin{vmatrix} g(A_1, B_1) & g(A_1, B_2) & \dots & g(A_1, B_m) \\ g(A_2, B_1) & g(A_2, B_2) & \dots & g(A_2, B_m) \\ \vdots & \vdots & \ddots & \vdots \\ g(A_m, B_1) & g(A_m, B_2) & \dots & g(A_m, B_m) \end{vmatrix} \tag{2.20}$$

We finally obtain:

$$G^{<}_{xx'}(t,t') = \sum_{n\geq 0} \frac{(iU)^n}{n!} \int_0^{t_\mathrm{M}} \sum_{\{a_k\}} \sum_{\{x_k,y_k\}} \prod_{k=1}^{n} [(-1)^{a_k} V_{x_k y_k}(u_k)\,\mathrm{d}u_k] \left[\!\!\left[\begin{matrix} X, U_1, \ldots, U_{2n} \\ X', U_1, \ldots, U_{2n} \end{matrix} \right]\!\!\right] \quad (2.21)$$

This is an explicit formula for the calculation of all perturbation orders for $\mathbf{G}^{<}$. The introduction of Keldysh points and Wick determinants does not bring anything new from a theoretical perspective — it is merely a relabeling of classic results — but it is adapted to practical numerical calculations. The "lists" notation for the Wick determinant is also very convenient for a general interaction Hamiltonian such as Eq. 2.3.

2.1.2 Consequences of the evolution along the time contour

The main feature of the real-time formalism that makes it different from equilibrium formalisms is the time contour. The fact that we consider a closed contour leads to important consequences for numerical calculations. These are naturally explained within the framework of Feynman diagrams.

Interpretation of the Keldysh Green's functions

A small parenthesis may be necessary to understand how the Keldysh Green's function is connected to other important quantities. Starting from its definition Eq. 2.15 we can distinguish the four choices of Keldysh indices for X and X' in a 2×2 matrix:

$$G^{aa'}_{xx'}(t,t') = \begin{pmatrix} G^{T}_{xx'}(t,t') & G^{<}_{xx'}(t,t') \\ G^{>}_{xx'}(t,t') & G^{\bar{T}}_{xx'}(t,t') \end{pmatrix}_{aa'} \quad (2.22)$$

The lesser Green's function $G^{<}$ is defined in Eq. 2.4 and the greater Green's function is defined as:

$$G^{>}_{xx'}(t,t') \equiv -i \left\langle \mathbf{c}_x(t) \mathbf{c}^{\dagger}_{x'}(t') \right\rangle \quad (2.23)$$

We introduced the time-ordered and anti-time-ordered Green's functions:

$$G^{T}_{xx'}(t,t') \equiv -i \left\langle T \mathbf{c}_x(t) \mathbf{c}^{\dagger}_{x'}(t') \right\rangle \quad (2.24)$$

$$G^{\bar{T}}_{xx'}(t,t') \equiv -i \left\langle \bar{T} \mathbf{c}_x(t) \mathbf{c}^{\dagger}_{x'}(t') \right\rangle \quad (2.25)$$

which are themselves related to the lesser and greater Green's functions through:

$$G^{T}_{xx'}(t,t') = \theta(t-t') G^{>}_{xx'}(t,t') + \theta(t'-t) G^{<}_{xx'}(t,t') \quad (2.26)$$

$$G^{\bar{T}}_{xx'}(t,t') = \theta(t-t') G^{<}_{xx'}(t,t') + \theta(t'-t) G^{>}_{xx'}(t,t') \quad (2.27)$$

T and $\bar{T}$ are the time-ordering and anti-time-ordering operators. There are in fact only two independent real-time Green's functions, which can be chosen to be the lesser and greater ones.

The retarded Green's function can be defined in the time domain as:

$$G^{R}_{xx'}(t,t') \equiv -i\theta(t-t') \left\langle \{\mathbf{c}_x(t), \mathbf{c}^{\dagger}_{x'}(t')\} \right\rangle \quad (2.28)$$

where $\{\mathbf{A}, \mathbf{B}\} \equiv \mathbf{AB} + \mathbf{BA}$ is the anticommutator. This definition matches the usual definition in the frequency domain (the limit $\eta \to 0^+$ is taken implicitly):

$$\mathbf{G}^R(\omega) \equiv \frac{1}{\omega + i\eta - \mathbf{H}} \tag{2.29}$$

It can be computed from the Keldysh Green's function through:

$$\mathbf{G}^R = \mathbf{G}^T - \mathbf{G}^< \tag{2.30}$$

Of particular importance, the imaginary part of $\mathbf{G}^R$ yields the spectral function $\mathbf{A}(\omega) \equiv -\operatorname{Im}[\mathbf{G}^R(\omega)]/\pi$. Its diagonal components $A_{xx}(\omega)$ are the local density of state on orbital x.

The lesser and greater Green's functions also have interesting interpretations. At equilibrium, it can be shown that $\mathbf{G}^<(\omega) = 2\pi i n_\mathrm{F}(\omega)\mathbf{A}(\omega)$ and $\mathbf{G}^>(\omega) = 2\pi i[1 - n_\mathrm{F}(\omega)]\mathbf{A}(\omega)$, with n_F the Fermi distribution. Their diagonal components are proportional to respectively the density (per unit energy) of electrons and holes. They are typically measured by (inverse) photoemission spectroscopy. Their interpretation is kept even out of equilibrium.

Real-time Feynman diagrams

Now that Green's functions on the Schwinger–Keldysh contour have been properly introduced, the result of Eq. 2.21 is easily generalized to $G^{aa'}_{xx'}(t, t')$ for any Keldysh indices a and a':

$$G^{aa'}_{xx'}(t,t') = \sum_{n\geq 0} \frac{(iU)^n}{n!} \int_0^{t_\mathrm{M}} \sum_{\{a_k\}} \sum_{\{x_k, y_k\}} \prod_{k=1}^{n} [(-1)^{a_k} V_{x_k y_k}(u_k)\, \mathrm{d}u_k] \left[\!\!\left[\begin{matrix} (x,t,a)\,, U_1, \ldots, U_{2n} \\ (x',t',a'), U_1, \ldots, U_{2n} \end{matrix} \right]\!\!\right] \tag{2.31}$$

where the definitions of U_k are unchanged.

This perturbative expansion can be understood as a sum of Feynman diagrams. By expanding a Wick determinant, one get a sum over all ways to link Keldysh points from the top row (in the $[\![\ldots]\!]$ notation) with the points of the bottom row. For instance:

$$\left[\!\!\left[\begin{matrix} A_1, \ldots, A_m \\ B_1, \ldots, B_m \end{matrix} \right]\!\!\right] = \sum_{\mathcal{P}} (-1)^{|\mathcal{P}|} g(A_1, B_{\mathcal{P}(1)}) \ldots g(A_m, B_{\mathcal{P}(m)}) \tag{2.32}$$

where the sum is over all permutations $\mathcal{P}$ of m elements, and $|\mathcal{P}|$ is the permutation parity. Each term is represented by a diagram. At order n, each diagram has n vertices made by pairs of Keldysh points (U_{2k-1}, U_{2k}) for $1 \leq k \leq n$ and labeled with the corresponding $(-1)^{a_k} V_{x_k y_k}(u_k)$. Two external Keldysh points X and X' form the external legs of the diagrams. Unperturbed Green's functions $g(A, B)$ label edges between Keldysh points A and B. Each diagram is a topologically different way to connect Keldysh points, respecting two edges for internal Keldysh points but only one for the two external points. Fig. 2.4 shows two typical diagrams at order $n = 2$. Vertices are attached to a time and a Keldysh index, and therefore can be placed onto the Schwinger–Keldysh contour. The relative position of vertices on the contour decides if the edges are labeled by $g^<$ or $g^>$.

A contribution is associated to each diagram. For every value given to the internal Keldysh points, the product of all labels from the edges $g(A, B)$ and vertices

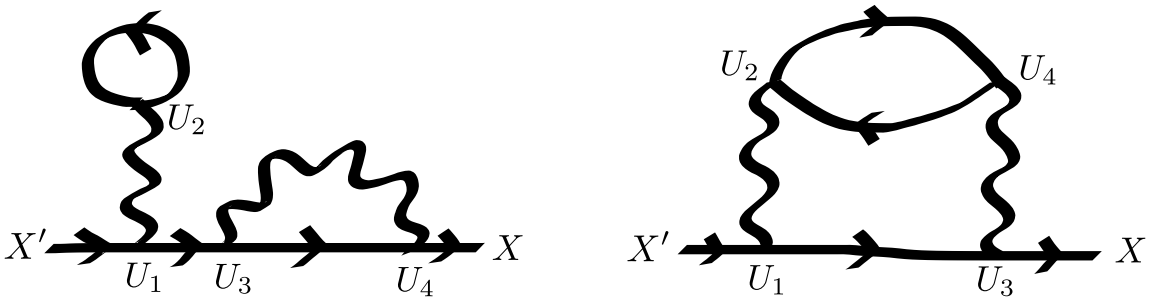

Figure 2.4: Two different connected diagrams for order $n = 2$. The U_i are the internal Keldysh points, X and X' are the external Keldysh points. Arrows between Keldysh points $B \to A$ represent unperturbed Green's functions $g(A, B)$. Wiggly lines are vertices.

$(-1)^{a_k} V_{x_k y_k}(u_k)$ is taken, and all summed together for all possible internal Keldysh points. The result is multiplied by $(iU)^n/n!$, and by -1 if the diagram contains an odd number of closed loops of Green's functions. Summing the contributions of all diagrams gives $G(X, X')$.

One can also define vacuum diagrams, which are diagrams with no external points. These appear in the expansion in powers of U of $\langle 1 \rangle = \mathrm{Tr}(\boldsymbol{\rho})$, following the same derivation as for the Green's function. Of course, $\mathrm{Tr}(\boldsymbol{\rho}) = 1$, so the sum of the vacuum diagrams is zero for any $n > 0$. This translates into:

$$\int_0^{t_\mathrm{M}} \sum_{\{a_k\}} \sum_{\{x_k, y_k\}} \prod_{k=1}^{n} [(-1)^{a_k} V_{x_k y_k}(u_k)\, \mathrm{d}u_k] \left[\!\!\left[\begin{matrix} U_1, \ldots, U_{2n} \\ U_1, \ldots, U_{2n} \end{matrix} \right]\!\!\right] = 0 \tag{2.33}$$

In fact, the contribution of each vacuum diagram is zero. But a stronger statement can be made. The contribution of each vacuum diagram is zero, even *before* integrating over times, orbitals and Keldysh indices, except for one Keldysh index. The proof is rather straightforward. For a given list of n vertices $(U_1, U_2), \ldots, (U_{2n-1}, U_{2n})$, consider the vertex with largest time and note a_p its Keldysh index. Flipping this index does not change the order of the vertices on the contour, so that the contribution is left unchanged, except for a factor -1. Hence, summing the contributions for $a_p = 0$ and $a_p = 1$ gives zero, independently of all other values of the Keldysh points. By considering all connections between vertices and summing over all Keldysh indices, we deduce the important following result. For $n \geq 1$, and any times $u_1, \ldots, u_n$ and orbital indices $x_1, \ldots, x_n$ and $y_1, \ldots, y_n$, we have:

$$\sum_{\{a_k\}} \prod_{k=1}^{n} (-1)^{a_k} \left[\!\!\left[\begin{matrix} U_1, \ldots, U_{2n} \\ U_1, \ldots, U_{2n} \end{matrix} \right]\!\!\right] = 0 \tag{2.34}$$

Diagrams can be grouped in two categories. The disconnected diagrams are those which can be separated in two unlinked parts. Connected diagrams are those which cannot. Following the same argument used for vacuum diagrams, disconnected diagrams must have a zero contribution, thanks to the sum over Keldysh indices.

The fact that vacuum and disconnected diagrams have zero contribution is an important feature of the real-time formalism. In equilibrium formalisms such as the imaginary time formalism, disconnected diagrams have non-zero contributions and must be eliminated from the sum of all diagrams. Here however, we are free to regroup all diagrams

into a Wick determinant — which is much easier to compute than an enumeration of diagrams — because the sum over Keldysh indices automatically eliminates disconnected diagrams.

Consequences on the long time limit: how to reach the steady state

At the beginning of this chapter, we introduced the necessity to start from a non-interacting system, to turn on interactions at $t = 0$ and to wait for the system to relax. It was said in particular that in some conditions, the way interaction is switched on does not matter. We now have a closer look into the validity of this scheme.

We consider the long time limit, when $t, t' \to +\infty$ and $|t - t'| \ll t_{\mathrm{M}}$. Assuming that the unperturbed system $\mathbf{H}_0$ is infinite and does not contain bound states, its excitations systematically relax, and any unperturbed Green's functions has to decay at long time, *i.e.* $g^{aa'}_{xx'}(u, u') \to 0$ when $|u-u'| \to +\infty$. In these conditions, a fundamental *clusterization property* arise: the following contribution to the integral in Eq. 2.31:

$$\sum_{\{a_k\}} \prod_{k=1}^{n} (-1)^{a_k} \left[\!\!\left[\begin{matrix} X, U_1, \ldots, U_{2n} \\ X', U_1, \ldots, U_{2n} \end{matrix} \right]\!\!\right] \tag{2.35}$$

does vanish when one or several u_k is far from t_{M} (*i.e.* close to the switching on of interaction at $t = 0$). In other worlds, the contributions are clustered around times t and t' in the n-dimensional integration domain. A proof is detailed in appendix D and shows that this is a consequence of the vacuum diagrams having zero contribution. Note that the sum over Keldysh indices is crucial, the Wick determinants themselves do not vanish but cancel each other. More details are given to this regard in section 3.2.1.

This will be an important property for the Monte Carlo method in chapter 3, but is also important to justify that the exact way interactions are switched on is irrelevant. Indeed, one can see from Eq. 2.31 that the values of the interaction $V_{xy}(u)$ close to the switching on time $u = 0$ do shape the integrand only where one or several u_k are close to 0. These parts of the integrand are however heavily damped by the clusterization property. The values of $V_{xy}(u \approx 0)$ are therefore "forgotten" in the long time limit. This is not true if the unperturbed system is finite or if it contains bound states: the clusterization property may not hold and the system may "remember" all its history.

If V is time-independent after its switching on, and if the clusterization property hold, all Green's functions become invariant by translation in time in the long time limit. This is the stationary limit that we will consider in all applications in this thesis. An interesting discussion on the role of relaxation in the real-time formalism can be found in Ref. [34].

2.1.3 Generalizations

Density-density interaction with quadratic compensation

The formalism can be extended to a perturbation Hamiltonian with density-density interaction and quadratic terms of the form:

$$\mathbf{H}_{\mathrm{int}}(t) \equiv \sum_{xy} V_{xy}(t)(\mathbf{c}^\dagger_x \mathbf{c}_x - \alpha_x)(\mathbf{c}^\dagger_y \mathbf{c}_y - \alpha_y) \tag{2.36}$$

where α are real numbers. These have been introduced in Ref. [145] to tame the sign problem in diagrammatic quantum Monte Carlo. Indeed, if α_x is chosen to be equal to

the unperturbed density on orbital x, this set to zero the contribution of many diagrams (those containing a tadpole diagram), thus avoiding cancellations.

It has been shown in Ref. [128] that the series expansion of Green's functions is the same as in Eq. 2.31, except that the Wick matrix diagonal elements are transformed in the following way:

$$g(U_{2k}, U_{2k}) \to g(U_{2k}, U_{2k}) - i\alpha_{y_k} \tag{2.37a}$$
$$g(U_{2k-1}, U_{2k-1}) \to g(U_{2k-1}, U_{2k-1}) - i\alpha_{x_k} \tag{2.37b}$$

This amounts to derive a modified Wick theorem which state that:

$$\begin{aligned}\left\langle T^{\mathrm{c}}\tilde{\mathbf{c}}^\dagger(X')\tilde{\mathbf{c}}(X)[\tilde{\mathbf{c}}^\dagger(U_1)\tilde{\mathbf{c}}(U_1) - \alpha_{x_1}]\dots[\tilde{\mathbf{c}}^\dagger(U_{2n})\tilde{\mathbf{c}}(U_{2n}) - \alpha_{y_n}]\right\rangle \\ = -i^{2n+1}\begin{vmatrix} g(X,X') & g(X,U_1) & \dots & g(X,U_{2n}) \\ g(U_1,X') & g(U_1,U_1) - i\alpha_{x_1} & \dots & g(U_1,U_{2n}) \\ \vdots & \vdots & \ddots & \vdots \\ g(U_{2n},X') & g(U_{2n},U_1) & \dots & g(U_{2n},U_{2n}) - i\alpha_{y_n} \end{vmatrix}\end{aligned} \tag{2.38}$$

which can be proved recursively as in Ref. [128] appendix A.

Therefore, to take the α into account, one needs only to use the replacements 2.37 whenever a correlator between identical Keldysh points is met. All derivations can be done by first ignoring α, then replacing the non-interacting Green's functions with these rules. For this reason and for readability, we will keep these replacements implicit in Wick matrices, but explicit otherwise.

Multiple particle Green's functions

The formula 2.31 can be extended to any m-particle Green's functions of the form:

$$G(X_1, \dots, X_m; X'_1, \dots, X'_m) \equiv (-i)^m \left\langle T^{\mathrm{c}}\mathbf{c}(X_1)\mathbf{c}^\dagger(X'_1)\dots\mathbf{c}(X_m)\mathbf{c}^\dagger(X'_m)\right\rangle \tag{2.39}$$

with X_i and X'_i any Keldysh points. Following the derivation of section 2.1.1, one can see that the only difference is that the Wick determinant must be replaced by:

$$\begin{bmatrix}\!\begin{bmatrix} X, U_1, \dots, U_{2n} \\ X', U_1, \dots, U_{2n} \end{bmatrix}\!\end{bmatrix} \to \begin{bmatrix}\!\begin{bmatrix} X_1, \dots, X_m, U_1, \dots, U_{2n} \\ X'_1, \dots, X'_m, U_1, \dots, U_{2n} \end{bmatrix}\!\end{bmatrix} \tag{2.40}$$

This formula is compatible with perturbation Hamiltonians such as Eq. 2.36.

Moreover, if for a given i the Keldysh points X_i and X'_i share the same time and orbital index x_i, then a further straightforward generalization is possible. Replacing $\mathbf{c}(X_i)\mathbf{c}^\dagger(X'_i) \to \mathbf{c}(X_i)\mathbf{c}^\dagger(X'_i) + \alpha_{x_i}$ in Eq. 2.39 amounts to replace $g(X_i, X'_i) \to g(X_i, X'_i) - i\alpha_{x_i}$ in the Wick determinant. Again, to improve readability, we will keep this replacement implicit in Wick matrices, but explicit otherwise.

2.2 Kernels of the Green's functions

Now that the formalism is in place, we use it to define the kernel K of a Green's function G. It is obtained by expanding the Wick determinant along one of the external Keldysh points (*e.g.* X) of G, so that K does not depend on it. G is finally the convolution between the kernel and the non-interacting Green's function. The kernel

is therefore a time-dependant function which contains all required information, and is naturally obtained within a Monte Carlo scheme similar to Ref. [128].

A higher order kernel L is also defined and its relation to G explained. The choice to compute K or L will yield different performances of the QMC. Finally, simplified relations for retarded Green's functions and kernels are derived. As this section is rather technical, a summary of the important formulas is provided at the end of this chapter (page 43).

In this section, and the rest of this work, we will consider a density-density interaction with quadratic compensation α_x. The implicit replacements in Wick matrices detailed in section 2.1.3 are effective.

2.2.1 Properties of Wick determinants

We first review some interesting properties of Wick determinants. Wick determinants inherits from the general properties of determinants: permutation of lines or columns only change the determinant by a factor ± 1. More precisely, if $\mathcal{P}$ and $\mathcal{Q}$ are two permutations of m elements, then:

$$\left[\!\!\left[\begin{matrix} A_1, \dots, A_m \\ B_1, \dots, B_m \end{matrix} \right]\!\!\right] = (-1)^{|\mathcal{P}|+|\mathcal{Q}|} \left[\!\!\left[\begin{matrix} A_{\mathcal{P}(1)}, \dots, A_{\mathcal{P}(m)} \\ B_{\mathcal{Q}(1)}, \dots, B_{\mathcal{Q}(m)} \end{matrix} \right]\!\!\right] \tag{2.41}$$

where $|\mathcal{P}|$ is the parity of the permutation $\mathcal{P}$.

It will be useful to work with the matrix underneath the determinant, that we call the *Wick matrix*, and denote its elements:

$$\left[\!\!\left[\begin{matrix} A_1, \dots, A_m \\ B_1, \dots, B_m \end{matrix} \right]\!\!\right]_{ij} \equiv g(A_i, B_j) \tag{2.42}$$

The determinant is assumed without the indices:

$$\left[\!\!\left[\begin{matrix} A_1, \dots, A_m \\ B_1, \dots, B_m \end{matrix} \right]\!\!\right] = \det \left[\!\!\left[\begin{matrix} A_1, \dots, A_m \\ B_1, \dots, B_m \end{matrix} \right]\!\!\right]_{ij} \tag{2.43}$$

We will use the usual expansion of a determinant along one row or one column in terms of the cofactor matrix. It takes the form:

$$\left[\!\!\left[\begin{matrix} A_1, \dots, A_m \\ B_1, \dots, B_m \end{matrix} \right]\!\!\right] = \sum_{k=1}^{m} (-1)^{k+1} g(A_k, B_1) \left[\!\!\left[\begin{matrix} A_1, \dots \cancel{A_k} \dots, A_m \\ \cancel{B_1}, B_2, \dots, B_m \end{matrix} \right]\!\!\right] \tag{2.44}$$

for the expansion along the first column and:

$$\left[\!\!\left[\begin{matrix} A_1, \dots, A_m \\ B_1, \dots, B_m \end{matrix} \right]\!\!\right] = \sum_{k=1}^{m} (-1)^{k+1} g(A_1, B_k) \left[\!\!\left[\begin{matrix} \cancel{A_1}, \dots\dots, A_m \\ B_1, \cancel{B_k}, \dots, B_m \end{matrix} \right]\!\!\right] \tag{2.45}$$

for the expansion along the first row. The notation $\cancel{A_k}$ ($\cancel{B_k}$) stands for the fact that the corresponding row or column must be removed from the Wick matrix.

Last, we will also make a systematic use of the fact that the cofactor matrix is directly related to the inverse of the matrix:

$$(-1)^{i+j} \left[\!\!\left[\begin{matrix} A_1, \dots \cancel{A_i} \dots, A_m \\ B_1, \dots \cancel{B_j} \dots, B_m \end{matrix} \right]\!\!\right] = \left[\!\!\left[\begin{matrix} A_1, \dots, A_m \\ B_1, \dots, B_m \end{matrix} \right]\!\!\right]^{-1}_{ji} \left[\!\!\left[\begin{matrix} A_1, \dots, A_m \\ B_1, \dots, B_m \end{matrix} \right]\!\!\right] \tag{2.46}$$

2.2.2 Definition of the kernel K for the one-particle Green's function

In Ref. [128], a Quantum Monte Carlo scheme was defined directly on Eq. 2.31 so that a single run could provide the value of $G^{aa'}_{xx'}(t,t')$ for a single pair of times t and t'. In order to extend the technique and obtain a full curve (as a function of t) in a single run, a different form must be used. Performing the expansion of Eq. 2.45 on Eq. 2.31, we obtain:

$$G^{aa'}_{xx'}(t,t') = g^{aa'}_{xx'}(t,t') + \sum_{n\geq 1} \frac{i^n U^n}{n!} \int_0^{t_\mathrm{M}} \sum_{\{a_k\}} \sum_{\{x_k,y_k\}} \prod_{k=1}^{n} [(-1)^{a_k} V_{x_k y_k}(u_k)\,\mathrm{d}u_k] \quad \times$$
$$\left(\sum_{p=1}^{2n} (-1)^p g\left[(x,t,a),U_p\right] \left[\!\!\left[\begin{matrix} U_1 & ,U_2,\ldots\ldots,U_{2n} \\ (x',t',a'),U_1,\ldots \not{U}_p \ldots,U_{2n} \end{matrix} \right]\!\!\right] + g\left[(x,t,a),(x',t',a')\right] \left[\!\!\left[\begin{matrix} U_1,\ldots,U_{2n} \\ U_1,\ldots,U_{2n} \end{matrix} \right]\!\!\right] \right) \tag{2.47}$$

The last term of the sum vanishes for $n > 0$ due to Eq. 2.34. Factorizing the g from the sum, we arrive at:

$$G^{aa'}_{xx'}(t,t') = g^{aa'}_{xx'}(t,t') + \int_0^{t_\mathrm{M}} \mathrm{d}u \sum_{b,y} (-1)^b g^{ab}_{xy}(t,u) K^{ba'}_{yx'}(u,t') \tag{2.48}$$

where the kernel $K^{ba'}_{yx'}(u,t') = K(Y,X')$ with $Y \equiv (y,u,b)$ is defined by:

$$K(Y,X') \equiv (-1)^b \sum_{n\geq 1} \frac{i^n U^n}{n!} \int_0^{t_\mathrm{M}} \sum_{\{a_k\}} \sum_{\{x_k,y_k\}} \prod_{k=1}^{n} [(-1)^{a_k} V_{x_k y_k}(u_k)\,\mathrm{d}u_k] \quad \times$$
$$\sum_{p=1}^{2n} (-1)^p \delta_c(Y,U_p) \left[\!\!\left[\begin{matrix} U_1,U_2,\ldots\ldots,U_{2n} \\ X',U_1,\ldots \not{U}_p \ldots,U_{2n} \end{matrix} \right]\!\!\right] \tag{2.49}$$

We introduced the contour Dirac delta notation:

$$\delta_c\left[(x,t,a),(x',t',a')\right] \equiv \delta(t-t')\delta_{aa'}\delta_{xx'}. \tag{2.50}$$

The essence of the kernel idea lies in Eq. 2.48 and 2.49. The expression for K shows that the Monte Carlo algorithm of Ref. [128] can be extended to compute it — although we agree this is not obvious at first sight, this will be detailed in the next chapter. Moreover, Eq. 2.48 shows that the Green's function is a simple convolution (along time and orbital and Keldysh indices) between K and g. In frequency domain, we can therefore obtain G, the target of the calculation, from K by a simple matrix product.

A symmetric kernel $\bar{K}$ may be derived following the exact same route but now expanding the Wick determinant along the first *column* using Eq. 2.44. We find:

$$G^{aa'}_{xx'}(t,t') = g^{aa'}_{xx'}(t,t') + \int_0^{t_\mathrm{M}} \mathrm{d}u \sum_{b,y} (-1)^b \bar{K}^{ab}_{xy}(t,u) g^{ba'}_{yx'}(u,t') \tag{2.51}$$

where the kernel $\bar{K}$ is defined by:

$$\bar{K}(X,Y) \equiv (-1)^b \sum_{n\geq 1} \frac{i^n U^n}{n!} \int_0^{t_{\mathrm{M}}} \sum_{\{a_k\}} \sum_{\{x_k,y_k\}} \prod_{k=1}^{n} [(-1)^{a_k} V_{x_k y_k}(u_k)\,\mathrm{d}u_k] \quad \times \\ \sum_{p=1}^{2n} (-1)^p \delta_c(Y,U_p) \left[\!\!\left[\begin{matrix} X, U_1, \ldots \not{U_p} \ldots, U_{2n} \\ U_1, U_2, \ldots\ldots\ldots, U_{2n} \end{matrix} \right]\!\!\right] \quad (2.52)$$

2.2.3 Definition of the kernel L of the F Green's function

We define a new Green's function with 4 operators, the F function. As we shall see, the F Green's function can also be represented in term of a kernel so that we will be able to design a direct QMC method to calculate it. Its interest stems from the fact that it can be used to reconstruct G while the corresponding QMC technique will be more precise at high frequency. It is defined as:

$$F^{aa'}_{xx'z}(t,t') \equiv (-i)^2 \left\langle T^{\mathrm{c}} \mathbf{c}(x,t,a) \mathbf{c}^\dagger(x',t',a') \left[\mathbf{c}^\dagger(z,t',a') \mathbf{c}(z,t',a') - \alpha_z \right] \right\rangle \quad (2.53)$$

We prove that F is essentially equal to $\bar{K}$ (up to interacting matrix elements). In other numerical methods, the function F is known to provide a better estimate of the Green's function. It has been used in the context of the Numerical Renormalization Group [18] as well as in imaginary time QMC methods as an *improved estimator* [51].

The expansion of F reads:

$$F^{aa'}_{xx'z}(t,t') = -\sum_{n\geq 0} \frac{i^n U^n}{n!} \int_0^{t_{\mathrm{M}}} \sum_{\{a_k\}} \sum_{\{x_k,y_k\}} \prod_{k=1}^{n} [(-1)^{a_k} V_{x_k y_k}(u_k)\,\mathrm{d}u_k] \quad \times \\ \left[\!\!\left[\begin{matrix} (x,t,a)\,, (z,t',a'), U_1, \ldots, U_{2n} \\ (x',t',a'), (z,t',a'), U_1, \ldots, U_{2n} \end{matrix} \right]\!\!\right] \quad (2.54)$$

To obtain the kernel of F, we expand the determinant along its first row using Eq. 2.45:

$$F^{aa'}_{xx'z}(t,t') = -\sum_{n\geq 0} \frac{i^n U^n}{n!} \int_0^{t_{\mathrm{M}}} \sum_{\{a_k\}} \sum_{\{x_k,y_k\}} \prod_{k=1}^{n} [(-1)^{a_k} V_{x_k y_k}(u_k)\,\mathrm{d}u_k] \quad \times \\ \left(\sum_{p=1}^{2n} (-1)^{p+1} g[(x,t,a),U_p] \left[\!\!\left[\begin{matrix} (z,t',a')\,, \quad U_1 \quad, U_2, \ldots\ldots\ldots, U_{2n} \\ (x',t',a'), (z,t',a'), U_1, \ldots \not{U_p} \ldots, U_{2n} \end{matrix} \right]\!\!\right] \right. \\ + g[(x,t,a),(x',t',a')] \left[\!\!\left[\begin{matrix} (z,t',a'), U_1, \ldots, U_{2n} \\ (z,t',a'), U_1, \ldots, U_{2n} \end{matrix} \right]\!\!\right] \\ \left. - g[(x,t,a),(z,t',a')] \left[\!\!\left[\begin{matrix} (z,t',a'), U_1, \ldots, U_{2n} \\ (x',t',a'), U_1, \ldots, U_{2n} \end{matrix} \right]\!\!\right] \right) \quad (2.55)$$

Identifying the two last terms with the corresponding expansion of G, we arrive at:

$$F^{aa'}_{xx'z}(t,t') = -g^{aa'}_{xx'}(t,t')[G^{<}_{zz}(t',t') - i\alpha_z] + g^{aa'}_{xz}(t,t') G^{<}_{zx'}(t',t') \\ - \int_0^{t_{\mathrm{M}}} \mathrm{d}u \sum_{b,y} (-1)^b g^{ab}_{xy}(t,u) L^{ba'}_{yx'z}(u,t') \quad (2.56)$$

where the kernel L is defined by:

$$L^{ba'}_{yx'z}(u,t') \equiv (-1)^b \sum_{n\geq 1} \frac{i^n U^n}{n!} \int_0^{t_\mathrm{M}} \sum_{\{a_k\}} \sum_{\{x_k,y_k\}} \prod_{k=1}^{n} [(-1)^{a_k} V_{x_k y_k}(u_k)\,\mathrm{d}u_k] \times \sum_{p=1}^{2n} (-1)^{p+1} \delta_c[(y,u,b),U_p] \left[\!\!\left[\begin{matrix} (z,t',a')\ , & U_1 & , U_2, \ldots\ldots\ldots, U_{2n} \\ (x',t',a'), (z,t',a'), & U_1, \ldots & \not{U_p} \ldots, U_{2n} \end{matrix} \right]\!\!\right] \quad (2.57)$$

The same conclusions can be said from these two last equations as in the previous section, except for the presence of $G^<(t',t')$ in Eq. 2.56. However, these will be obtained as by-product of the QMC algorithm to compute L. In the next section we see how to obtain G from F, and that it does not bring additional complexity.

2.2.4 Relation between F, $\bar{K}$ and G: equations of motion

The expressions for the different kernels can be formally integrated to provide connections between the different kernels and Green's functions. We arrive at expressions that are essentially what can be obtained directly using equations of motions.

We start from the expression of $\bar{K}$, Eq. 2.52. The first step is to realize that the sum over the $2n$ determinants provides identical contributions to the kernel. Indeed, odd $p = 2k-1$ and even $p = 2k$ values of p provide identical contributions due to the symmetry of V_{xy}. Similarly, odd values $p = 2k-1$ have the same contribution as $p = 1$ as can be shown by using the symmetry properties of the determinant and exchanging the role of $U_1 \leftrightarrow U_{2k-1}$ and $U_2 \leftrightarrow U_{2k}$ in the sums and integration. We arrive at:

$$\bar{K}^{ab}_{xy}(t,u) = (-1)^b \sum_{n\geq 1} \frac{i^n U^n}{n!} \int_0^{t_\mathrm{M}} \mathrm{d}u_1 \sum_{a_1} \sum_{x_1,y_1} (-1)^{a_1} V_{x_1,y_1}(u_1) \int_0^{t_\mathrm{M}} \sum_{\substack{\{a_k\} \\ k\geq 2}} \sum_{\substack{\{x_k,y_k\} \\ k\geq 2}} \prod_{k=2}^{n} [(-1)^{a_k} V_{x_k y_k}(u_k)\,\mathrm{d}u_k] 2n\, \delta_c[U_1,(y,u,b)] \left[\!\!\left[\begin{matrix} (x,t,a), U_2, U_3, \ldots, U_{2n} \\ U_1\ \ , U_2, U_3, \ldots, U_{2n} \end{matrix} \right]\!\!\right] \quad (2.58)$$

We can now perform explicitly the integral over u_1 where the delta function yields, for $u \in [0, t_\mathrm{M}]$ ($\bar{K}$ is zero otherwise):

$$\bar{K}^{ab}_{xy}(t,u) = 2iU \sum_{n\geq 1} \frac{i^{n-1} U^{n-1}}{(n-1)!} \sum_{y_1} V_{y,y_1}(u) \quad \times \int_0^{t_\mathrm{M}} \sum_{\substack{\{x_k,y_k\} \\ \{a_k\} \\ k\geq 2}} \prod_{k=2}^{n} [(-1)^{a_k} V_{x_k y_k}(u_k)\,\mathrm{d}u_k] \left[\!\!\left[\begin{matrix} (x,t,a), (y_1,u,b), U_3, \ldots, U_{2n} \\ (y,u,b), (y_1,u,b), U_3, \ldots, U_{2n} \end{matrix} \right]\!\!\right] \quad (2.59)$$

$$= 2iU \sum_{z} V_{y,z}(u) \sum_{n\geq 0} \frac{i^n U^n}{n!} \quad \times \int_0^{t_\mathrm{M}} \sum_{\substack{\{x_k,y_k\} \\ \{a_k\}}} \prod_{k=1}^{n} [(-1)^{a_k} V_{x_k y_k}(u_k)\,\mathrm{d}u_k] \left[\!\!\left[\begin{matrix} (x,t,a), (z,u,b), U_1, \ldots, U_{2n} \\ (y,u,b), (z,u,b), U_1, \ldots, U_{2n} \end{matrix} \right]\!\!\right] \quad (2.60)$$

$$= -2iU \sum_z V_{yz}(u) F^{ab}_{xyz}(t,u) \tag{2.61}$$

This shows the kernel $\bar{K}$ is no more than a sum of 2-particle Green's functions. The relation between $\bar{K}$ and G in Eq. 2.51 can then be transformed into:

$$G^{aa'}_{xx'}(t,t') = g^{aa'}_{xx'}(t,t') - 2iU \int_0^{t_\mathrm{M}} \mathrm{d}u \sum_{b,y} (-1)^b \sum_z V_{yz}(u) F^{ab}_{xyz}(t,u) g^{ba'}_{yx'}(u,t') \tag{2.62}$$

which can be used to reconstruct G from the knowledge of F. This relation is the well known equation of motion for G. It also shows that F is essentially the convolution of G with the self-energy, as we recognize the Dyson equation.

As a side note, we show in appendix B that the kernel L can also be expressed in terms of Green's functions by following the same formalism, in accordance with the equation of motion for F.

2.2.5 Retarded and advanced kernels

As the retarded (or advanced) Green's functions directly give the spectral functions, they are of particular interest. At equilibrium, they contain all information which can be obtained from the Keldysh Green's function. We show here simple relations to compute them from the kernels K, $\bar{K}$ or L.

The retarded and advanced Green's functions relate to the lesser and greater Green's functions as follows:

$$G^R_{xx'}(t,t') = \theta(t-t') \left(G^>_{xx'}(t,t') - G^<_{xx'}(t,t') \right) \tag{2.63}$$
$$G^A_{xx'}(t,t') = \theta(t'-t) \left(G^<_{xx'}(t,t') - G^>_{xx'}(t,t') \right) \tag{2.64}$$

where θ is the Heaviside function. From the definitions of the time-ordered and anti-time-ordered Green's functions, these can also be written as:

$$G^R_{xx'}(t,t') = G^{a0}_{xx'}(t,t') - G^{a1}_{xx'}(t,t') \tag{2.65}$$
$$G^A_{xx'}(t,t') = G^{0a}_{xx'}(t,t') - G^{1a}_{xx'}(t,t') \tag{2.66}$$

where a can be any Keldysh index. These are also valid for the non-interacting g. As $\bar{K}$ is a sum of Green's function, one may define in the same way a retarded version of $\bar{K}$, denoted $\bar{K}^R$. We can see from Eq. 2.61 and the definition of F in Eq. 2.53 that $\bar{K}^R$ follows the same properties:

$$\bar{K}^R_{xx'}(t,t') = \bar{K}^{a0}_{xx'}(t,t') - \bar{K}^{a1}_{xx'}(t,t') \tag{2.67}$$

We now show a simple relation between G^R, g^R and $\bar{K}^R$. Plugging Eq. 2.51 into Eq. 2.65, one gets:

$$G^R_{xx'}(t,t') = g^R_{xx'}(t,t') \quad + \\ \int_0^{t_\mathrm{M}} \mathrm{d}u \sum_y \left(\bar{K}^{00}_{xy}(t,u)[g^{00}_{yx'}(u,t') - g^{01}_{yx'}(u,t')] - \bar{K}^{01}_{xy}(t,u)[g^{10}_{yx'}(u,t') - g^{11}_{yx'}(u,t')] \right) \tag{2.68}$$

This simplifies into:

$$G^R_{xx'}(t,t') = g^R_{xx'}(t,t') + \int_0^{t_\mathrm{M}} \mathrm{d}u \sum_y \bar{K}^R_{xy}(t,u) g^R_{yx'}(u,t') \tag{2.69}$$

Similar relations may be derived with K, F and L. In fact, for any of the functions K, F and L, which all depend on two times and two Keldysh indices, we choose to define a retarded and advanced function in the same way as Eq. 2.63 and Eq. 2.64. As all of them are sums of Green's functions, one may show that they all verify similar properties as in Eq. 2.65 and 2.66. Then from Eq. 2.48 follows:

$$G^A_{xx'}(t,t') = g^A_{xx'}(t,t') + \int_0^{t_\mathrm{M}} \mathrm{d}u \sum_y g^A_{xy}(t,u) K^A_{yx'}(u,t') \tag{2.70}$$

and from Eq. 2.56 follows:

$$F^A_{xx'z}(t,t') = -g^A_{xx'}(t,t')[G^<_{zz}(t',t') - i\alpha_z] + g^A_{xz}(t,t') G^<_{zx'}(t',t) - \int_0^{t_\mathrm{M}} \mathrm{d}u \sum_y g^A_{xy}(t,u) L^A_{yx'z}(u,t') \tag{2.71}$$

We finish this chapter with a one page summary (next page) of the main formulas of interest for the calculation of the Green's function G from the kernel $\bar{K}$.

2.3 Kernels: Summary of formulas

For Keldysh points $X \equiv (x,t,a)$ and $X' \equiv (x',t',a')$, the expansion of the Green's function in powers of the interaction strength U is:

$$G(X,X') = \sum_{n\geq 0} \frac{(iU)^n}{n!} \int_0^{t_{\mathrm{M}}} \sum_{\{a_k\}} \sum_{\{x_k,y_k\}} \prod_{k=1}^{n} [(-1)^{a_k} V_{x_k y_k}(u_k)\,\mathrm{d}u_k] \left[\!\!\left[\begin{matrix} X, U_1, \ldots, U_{2n} \\ X', U_1, \ldots, U_{2n} \end{matrix} \right]\!\!\right] \quad (2.72)$$

where the Wick determinant is explicitly:

$$\left[\!\!\left[\begin{matrix} X, U_1, \ldots, U_{2n} \\ X', U_1, \ldots, U_{2n} \end{matrix} \right]\!\!\right] = \quad (2.73)$$

$$\begin{vmatrix}
g^{aa'}_{xx'}(t,t') & g^{aa_1}_{xx_1}(t,u_1) & g^{aa_1}_{xy_1}(t,u_1) & g^{aa_2}_{xx_2}(t,u_2) & g^{aa_2}_{xy_2}(t,u_2) & \ldots & g^{aa_n}_{xy_n}(t,u_n) \\
g^{a_1a'}_{x_1x'}(u_1,t') & g^{<}_{x_1x_1}(u_1,u_1) & g^{>}_{x_1y_1}(u_1,u_1) & g^{a_1a_2}_{x_1x_2}(u_1,u_2) & g^{a_1a_2}_{x_1y_2}(u_1,u_2) & \ldots & g^{a_1a_n}_{x_1y_n}(u_1,u_n) \\
g^{a_1a'}_{y_1x'}(u_1,t') & g^{<}_{y_1x_1}(u_1,u_1) & g^{<}_{y_1y_1}(u_1,u_1) & g^{a_1a_2}_{y_1x_2}(u_1,u_2) & g^{a_1a_2}_{y_1y_2}(u_1,u_2) & \ldots & g^{a_1a_n}_{y_1y_n}(u_1,u_n) \\
g^{a_2a'}_{x_2x'}(u_2,t') & g^{a_2a_1}_{x_2x_1}(u_2,u_1) & g^{a_2a_1}_{x_2y_1}(u_2,u_1) & g^{<}_{x_2x_2}(u_2,u_2) & g^{>}_{x_2y_2}(u_2,u_2) & \ldots & g^{a_2a_n}_{x_2y_n}(u_1,u_n) \\
g^{a_2a'}_{y_2x'}(u_2,t') & g^{a_2a_1}_{y_2x_1}(u_2,u_1) & g^{a_2a_1}_{y_2y_1}(u_2,u_1) & g^{<}_{y_2x_2}(u_2,u_2) & g^{<}_{y_2y_2}(u_2,u_2) & \ldots & g^{a_2a_n}_{y_2y_n}(u_1,u_n) \\
\vdots & \vdots & \vdots & \vdots & \vdots & \ddots & \vdots \\
g^{a_na'}_{y_nx'}(u_n,t') & g^{a_na_1}_{y_nx_1}(u_n,u_1) & g^{a_na_1}_{y_ny_1}(u_n,u_1) & g^{a_na_2}_{y_nx_2}(u_n,u_2) & g^{a_na_2}_{y_ny_2}(u_n,u_2) & \ldots & g^{<}_{y_ny_n}(u_n,u_n)
\end{vmatrix}$$

We define the kernel $\bar{K}$ by expanding this determinant along the first column:

$$\bar{K}(X,Y) \equiv (-1)^b \sum_{n\geq 1} \frac{i^n U^n}{n!} \int_0^{t_{\mathrm{M}}} \sum_{\{a_k\}} \sum_{\{x_k,y_k\}} \prod_{k=1}^{n} [(-1)^{a_k} V_{x_k y_k}(u_k)\,\mathrm{d}u_k] \quad \times$$
$$\sum_{p=1}^{2n} (-1)^p \delta_c(Y,U_p) \left[\!\!\left[\begin{matrix} X, U_1, \ldots \not{U_p} \ldots, U_{2n} \\ U_1, U_2, \ldots\ldots\ldots, U_{2n} \end{matrix} \right]\!\!\right] \quad (2.74)$$

with $Y \equiv (y,u,b)$. The kernel relates to the Green's function through:

$$G^{aa'}_{xx'}(t,t') = g^{aa'}_{xx'}(t,t') + \int_0^{t_{\mathrm{M}}} \mathrm{d}u \sum_{b,y} (-1)^b \bar{K}^{ab}_{xy}(t,u) g^{ba'}_{yx'}(u,t') \quad (2.75)$$

This relation simplifies further when considering retarded Green's functions. For this, we define a retarded kernel:

$$\bar{K}^R_{xx'}(t,t') = \bar{K}^{a0}_{xx'}(t,t') - \bar{K}^{a1}_{xx'}(t,t') \quad (2.76)$$

where the choice of the Keldysh index a is irrelevant. The relation between retarded Green's function and kernel is then:

$$G^R_{xx'}(t,t') = g^R_{xx'}(t,t') + \int_0^{t_{\mathrm{M}}} \mathrm{d}u \sum_{y} \bar{K}^R_{xy}(t,u) g^R_{yx'}(u,t') \quad (2.77)$$

which can be written using matrix notations as:

$$\mathbf{G}^R(t,t') = \mathbf{g}^R(t,t') + \bar{\mathbf{K}}^R * \mathbf{g}^R(t,t') \quad (2.78)$$

where $*$ is the time convolution product based on matrix product. In case of time-translational invariant quantities, a Fourier transform leads to a particularly simple form in the frequency domain:

$$\mathbf{G}^R(\omega) = \mathbf{g}^R(\omega) + \bar{\mathbf{K}}^R(\omega) \cdot \mathbf{g}^R(\omega) \quad (2.79)$$

Chapter 3

Quantum Monte Carlo

Having introduced the formalism and tools (the kernels), we now proceed to build our real-time diagrammatic Quantum Monte Carlo (QMC) which will enable us to compute for example the perturbation series of Fig. 1.6 (page 25) in a single run.

Monte Carlo algorithms are powerful methods often used in physics to solve systems with many degrees of freedom, because the scaling of their computational cost does not depend on this number. In the context of condensed matter physics, QMC methods provide approximation-free numerical solutions of quantum many-body Hamiltonians in a very generic way.

A pioneer in this domain was the Hirsh–Fye algorithm [66]. Since then, a large family of methods called diagrammatic QMC made important breakthrough in computing equilibrium properties of diverse fermionic systems directly in the thermodynamic limit [86, 131, 168]. These provide perturbation series by sampling directly the Feynman diagrams in the imaginary time (Matsubara) formalism. In many fermionic systems however, the sign problem — the curse of Monte Carlo methods, which arises when terms massively cancel each other — was prohibitive, particularly at low temperature. The bold diagrammatic QMC formed an improvement [32, 46, 70, 93, 94, 124, 129, 132, 139, 166, 167]. Based on the fact that diagrams can be regrouped to construct larger diagrams, it takes advantage of previously encountered diagrams to form in a self-consistent loop new diagrams of higher orders. Cancellations between diagrams are then treated in a more systematic way. Impurity QMC solvers, especially used within DMFT (see Ref. [45] for a review), regroup diagrams into determinants to tame the sign problem. They exist in different flavours [48], using *e.g.* a diagrammatic expansion in the bath–impurity hybridization (CT-HYB) [173], or in the interaction with auxiliary field (CT-AUX) [44] or without (CT-INT) [144, 145]. Modern diagrammatic QMC regroup diagrams into determinants (*e.g.* Wick determinants) and systematically eliminate vacuum diagrams, however with a number of operations growing exponentially with the perturbation order [109, 128, 142, 143, 160].

Some of these methods have been brought to non-equilibrium systems thanks to the real-time formalism [111, 112, 146, 147, 151, 174, 175]. However a strong dynamical sign problem appears when computing long time evolution. The inchworm [21, 22, 24–26] algorithm and the algorithm of Ref. [128] appear to have reduced this problem. The latter explicitly sums the Keldysh indices, rather than leaving the Monte Carlo sample them. This provides an exact elimination of vacuum diagrams and massive cancellations between other diagrams.

In this chapter, we introduce the Markov chain Monte Carlo method for computing

arbitrary multi-dimensional integrals. Using this, we review the algorithm of Ref. [128] before extending it to the computation of kernels (defined in chapter 2). At the end of this chapter, we will have the tools to compute Green's functions directly in the frequency domain, as perturbation series. In the next chapter, we will see how to get physical quantities as functions of U from this type of perturbation series.

3.1 Introduction to Markov chain Monte Carlo

3.1.1 Monte Carlo algorithm for evaluating integrals

Monte Carlo numerical methods can be used to compute the integral of a real or complex function f over a domain $\mathcal{D} \subset \mathbb{R}^d$. The general idea is to randomly sample $\mathcal{D}$ and cumulate the corresponding values of f. Assuming one has the possibility to generate independent samples of this domain distributed according to a probability density P, we model such samples with Independent and Identically Distributed (IID) random variables $X_1, \ldots, X_N$. The Monte Carlo method consists in computing:

$$I \equiv \frac{1}{N} \sum_i \frac{f(X_i)}{P(X_i)} \tag{3.1}$$

The random function I is an unbiased estimator of the integral of f:

$$\mathbb{E}[I] = \int_{\mathcal{D}} f(x)\,\mathrm{d}x \tag{3.2}$$

where $\mathbb{E}$ denotes the probabilistic expectation value. The error of this estimation can be evaluated from the standard deviation σ of I:

$$\sigma(I) \equiv \sqrt{\mathrm{Var}(I)} \tag{3.3}$$

Using the fact that the X_i are IID:

$$\sigma(I) = \frac{1}{\sqrt{N}}\,\sigma\left(\frac{f}{P}(X_1)\right) \tag{3.4}$$

The most important features of the Monte Carlo method lie in this expression for the error. In particular, the scaling with N is problem-independent, it does not depend on the dimensionality of $\mathcal{D}$ or the smoothness of f. The Monte Carlo error always scales as $1/\sqrt{N}$, where N is the number of *independent* function evaluations. The pre-factor to this scaling, $\sigma(f(X_1)/P(X_1))$, depends however on f in a non-trivial way, and can lead in practice to important slow-down of the algorithm.

These features are in contrast with quadrature integration methods, for which error estimations rely on smoothness hypothesis for f, and the number of function evaluations scales exponentially with dimension d for a given error. For a smooth enough f, the error scales as $1/N^{p/d}$, where p depends on the quadrature method (*e.g.* $p = 2$ for the trapezoid method, 4 for the Simpson method). For dimension $d > 2p$, the Monte Carlo has a better scaling. In practice, for $d > 10$, Monte Carlo methods are the only viable way to perform integrals. This comparison is however limited to regular integration space. Monte Carlo algorithms are able to compute integrals on any kind of geometry, continuous or discreet, as long as it can be sampled. This is a major advantage compared to quadrature methods.

The choice of P is crucial for the efficiency of the method, as it can greatly affect the pre-factor to the error $\sigma(f(X_1)/P(X_1))$. Any positive and normalized function can be chosen, as long as $P(x) \neq 0$ wherever $f(x) \neq 0$, to make sure f/P do not diverge. Such divergence can lead to an infinite variance of I and a never converging Monte Carlo. See [159] for an example in Quantum Monte Carlo. In practice, P is often chosen only up to a normalization factor Z:

$$P(x) \equiv \frac{W(x)}{Z} \tag{3.5}$$

$$Z \equiv \int_{\mathcal{D}} W(x)\,\mathrm{d}x \tag{3.6}$$

where the choice is upon W, called the weight function. Therefore, Z has to be calculated separately from the chosen weight W, *e.g.* by another Monte Carlo calculation. Then, the integral can be evaluated as:

$$\int_{\mathcal{D}} f(x)\,\mathrm{d}x = Z\left\langle \frac{f}{W} \right\rangle_P \tag{3.7}$$

where the brackets denote the weighted average over $\mathcal{D}$ with weight P.

Assuming Z can be computed exactly, we now show that an optimal weight function is $W(x) \propto |f(x)|$. Without loss of generality, we constrain W to be normalized, *i.e.* $Z = 1$, and for simplicity, strictly positive ($|f|$ can be considered strictly positive if the zeros of f are removed from $\mathcal{D}$). We want to minimize $\mathrm{Var}(f/P(X_1))$ with respect to P. We note first that the set of normalized strictly positive P is convex. Also, computing the variance:

$$V[P] \equiv \mathrm{Var}\left(\frac{f}{P}(X_1)\right) = \int_{\mathcal{D}} \frac{|f(x)|^2}{P(x)}\,\mathrm{d}x - \left|\int_{\mathcal{D}} f(x)\,\mathrm{d}x\right|^2 \tag{3.8}$$

we see it is a strictly convex functional of P, because $1/P(x)$ is a strictly convex function of $P(x)$. Therefore, as a strictly convex function defined on a convex set, V has a single minimum.

To find this minimum P_0, we perform small perturbations to it: $P = P_0 + \phi$. Note that $\int \phi = 0$ in order to respect the normalization of P. To first order in ϕ we have:

$$V[P] = V[P_0] - \int_{\mathcal{D}} \phi(x)\frac{|f(x)|^2}{P_0(x)^2}\,\mathrm{d}x \tag{3.9}$$

The minimum is reached when the first order perturbations are zero for all ϕ, which happens when $|f(x)|^2/P_0(x)^2$ is a constant. To enforce that P_0 be positive, it is necessary that $P_0(x') \propto |f(x')|$.

This choice of weight has good properties: it does not sample parts of the domain where f is zero, and does sample all parts where f is non-zero. Also, parts of $\mathcal{D}$ corresponding to large values of f, *i.e.* more contributions to the integral, are sampled with a higher probability than parts corresponding to small values of f. This is especially important if the support of f is localized in a specific region of $\mathcal{D}$ (*e.g.* as for a pulse in time domain). The Monte Carlo method will work even without prior knowledge of its location and the boundaries of the domain can be extended at will without affecting its efficiency. Nevertheless, this is assuming independent random variables can be generated at no cost. We will see in section 3.1.2 that this is not in general true.

Let us finally stress an important drawback of Monte Carlo integration methods. Even with an optimal weight, there are still functions f which yields a large pre-factor in the error in Eq. 3.4. In particular, we can see from **??** that integration of functions which are large in absolute value on substantial parts of the domain, while their integral is small, will be affected by a large sign problem. Typical cases include functions with many oscillations around zero. Using the optimal weight function, one can see in Eq. 3.1 that the Monte Carlo algorithm finally sums only the sign of f (or its phase factor for a complex function). The sign problem arises when the positive and the negative signs (or the different phases for a complex function) cancel each other almost exactly. Indeed, one needs to average a large number of $+1$ and -1 (or $e^{i\phi}$ for a complex function) to obtain a result of small magnitude.

3.1.2 The Metropolis–Hastings algorithm: sampling random variables

In section 3.1.1 we were assuming a set of IID random variables have been generated over the domain $\mathcal{D}$ according to a given distribution P. If there exists straightforward methods to generate univariate random numbers with an arbitrary P, it is however necessary to rely on more complex algorithms in higher dimensionality. One of the most widely used method to generate such numbers is the Metropolis–Hastings algorithm [53, 58, 104].

The Metropolis–Hastings algorithm implements a discrete-time Markov chain. The set of possible states (or configurations) of the process is $\mathcal{D}$, which we will call configuration space. The configuration space can be discrete or continuous. As we are interested in integration, we will consider only the latter. The Markov chain is built so that it reaches a stationary distribution of states which equals P. Once in the stationary regime, the succession of its states provides naturally random elements of $\mathcal{D}$ distributed according to P. The application of this algorithm to Monte Carlo is a form of Markov chain Monte Carlo.

More precisely, if we can build an irreducible aperiodic Markov chain (as defined in [53], chapter 9) with $x \to y$ transition probability $V(y, x)\,\mathrm{d}y$, such that:

$$P(y) = \int_{\mathcal{D}} V(y, x) P(x)\,\mathrm{d}x \tag{3.10}$$

then the distribution of configurations will always tend toward P with increasing time. P is a unique limit.

To construct it, we consider an arbitrary Markov chain, defined by its $x \to y$ transition probability $\tilde{V}(y, x)\,\mathrm{d}y$. The Markov chain corresponding to V is obtained by the following process. Take a configuration $x \in \mathcal{D}$ and chose randomly the next configuration y according to $\tilde{V}(y, x)$. Accept this move with a probability $P(y)\tilde{V}(x, y)/P(x)\tilde{V}(y, x)$. If this ratio is larger than one, accept it anyway. The next configuration is taken to be y if the move is accepted, and x again if the move is rejected.

By following this process, we simulate a Markov chain with $x \to y$ transition proba-

bility:

$$V(y,x)\,\mathrm{d}y = \eta(y,x)\tilde{V}(y,x)\,\mathrm{d}y + \delta(x-y)\,\mathrm{d}y \int_{\mathcal{D}} [1-\eta(z,x)]\tilde{V}(z,x)\,\mathrm{d}z \tag{3.11}$$

$$\text{with} \quad \eta(y,x) \equiv \min\left(1, \frac{P(y)\tilde{V}(x,y)}{P(x)\tilde{V}(y,x)}\right) \tag{3.12}$$

The first term in Eq. 3.11 represents accepted moves, while the second is for rejected moves. One can easily check that V is a probability density, namely $\int V(y,x)\,\mathrm{d}y = 1$. This Markov chain is reversible, *i.e.* it respects the detailed balance with the distribution P:

$$V(y,x)\,\mathrm{d}y\,P(x)\,\mathrm{d}x = V(x,y)\,\mathrm{d}x\,P(y)\,\mathrm{d}y \tag{3.13}$$

This is obvious for $y = x$. For $y \neq x$, we distinguish two cases: if $P(y)\tilde{V}(x,y) > P(x)\tilde{V}(y,x)$ then $\eta(x,y) < 1$ and $V(x,y) = \tilde{V}(y,x)P(x)/P(y)$; in the opposite case, $\eta(y,x) < 1$ which brings the same conclusion. Reversibility is a sufficient — although not necessary [77] — condition for P to be a stationary distribution: integrating the detailed balance over x indeed gives the relation 3.10.

An important advantage of the Metropolis–Hastings method is that it only requires *ratios* of the target distribution P. This means there is no need to know explicitly its normalization. Considering that in Monte Carlo integration this distribution typically depends on the integrand (see section 3.1.1), we therefore avoid computing another complicated integral.

In each application, one has to check if the V Markov chain is irreducible and aperiodic. For irreducibility it suffices to verify that there is a non-zero probability to reach any state from any other state in a finite number of steps. It is also good practice to ensure bilateral transitions, *i.e.* for any two states x, y we have $\tilde{V}(y,x) \neq 0 \Leftrightarrow \tilde{V}(x,y) \neq 0$.

With this algorithm, we are able to produce random numbers identically distributed according to an arbitrary distribution. However, they are not independent. The correlation between the state of the chain after n moves and its initial configuration decreases exponentially with n. Therefore, a typical number of steps, the correlation time, is required to obtain decorrelated configurations.

There is a large latitude in the choice of $\tilde{V}$, but it is crucial in order to find a minimal correlation time. First, it has to be ergodic, meaning that it gives a non-zero probability to reach any state from any other state in a finite (preferably small) number of steps. The smaller the number of steps between any two states, the shorter is the correlation time. Improving the correlation time is also done by avoiding rejected moves. An acceptance ratio can be defined as the number of accepted moves divided by the number of proposed moves. Optimizing this ratio amount to bring η as close as possible to 1, therefore to build $\tilde{V}$ as close as possible to V. In the end, the smaller is the correlation time, the more independent configurations the Markov chain can produce in a given amount of steps. The efficiency of the Monte Carlo method is thus intimately linked to the choice of $\tilde{V}$.

Due to correlations, the error calculated from Eq. 3.4 is too optimistic. Typical error estimation in Markov chain Monte Carlo rely on an estimation of the correlation time, using for instance logarithmic bunching (see [87] p. 59). This is particularly efficient when the length of the available Markov chain — limited by computation time — is only a few dozens of correlation times. In this work however we were far from this limit, hence we could rely on a simpler and more robust method: running a dozen of very long (converged) Markov chains and compute the variance of their results.

3.2 Monte Carlo for computing a single correlation

Coming back to the physical problem of computing Green's functions, we describe in this section how the principles of Markov chain Monte Carlo can be applied to the computation of a single value from a Green's function. The starting point is Eq. 2.31 which we write again here:

$$G^{aa'}_{xx'}(t,t') = \sum_{n\geq 0} \frac{(iU)^n}{n!} \int_0^{t_{\mathrm{M}}} \sum_{\{a_k\}} \sum_{\{x_k,y_k\}} \prod_{k=1}^{n} [(-1)^{a_k} V_{x_k y_k}(u_k)\, \mathrm{d}u_k] \left[\!\!\left[\begin{matrix} (x,t,a)\,, U_1, \ldots, U_{2n} \\ (x',t',a'), U_1, \ldots, U_{2n} \end{matrix} \right]\!\!\right] \tag{3.14}$$

Most of this section is based on the work of Profumo *et al.* [128]. In section 3.3, we will adapt the Monte Carlo scheme of [128] to compute kernels of the Green's function (introduced in the end of chapter 2), and thus be able to compute full Green's functions rather than a single correlator.

3.2.1 Importance of the explicit sum over Keldysh indices

In Eq. 3.14, three large sums are good candidates for being computed with a Monte Carlo algorithm: the multi-dimensional integral over times, the sum over Keldysh indices and the sum over orbital indices pairs. If the three of them are sampled, each Monte Carlo step would require to compute a single $(2n+1)\times(2n+1)$ determinant. However, this would lead to a very bad sign problem, as shown in Ref. [128]. Indeed, the sum over Keldysh indices is responsible for important cancellations of Wick determinants, giving rise to a clusterization property as seen in section 2.1.2.

We illustrate here this important aspect in Fig. 3.1, which is adapted from Ref. [128]. Different integrand are shown for the calculation at order $n = 2$ of $G^<(t = 10, t' = 10)$ on the impurity of the Anderson impurity model discussed in chapter 5. The left panel shows the imaginary part of the integrands before the Keldysh sum, *i.e.*:

$$\left[\!\!\left[\begin{matrix} X, U_1, U_2, U_3, U_4 \\ X', U_1, U_2, U_3, U_4 \end{matrix} \right]\!\!\right] \tag{3.15}$$

for all choices of Keldysh indices a_1 and a_2. These integrands do not vanish for times far from t and t'. However, when summed together they form the integrand shown in the right panel, and display a clear clusterization.

Sampling the Keldysh indices would perform very badly at computing such massive cancellations. It is preferred to sum explicitly the 2^n Keldysh indices values, even though this means computing 2^n determinants at each Monte Carlo step. Ref. [128] shows that, in the Anderson impurity problem, this cost is largely counter-balanced by the need for a much smaller statistics.

Moreover, Fig. 3.1 shows explicitly that the individual integrands of the left panel have extensive support which endlessly increases with t_{M}, while the sum integrand has a bounded support even for $t_{\mathrm{M}} = +\infty$. This is the clusterization property introduced in section 2.1.2 and proved in appendix D. The latter integrand is much better behaved and is preferred for a Monte Carlo integration. For these two reason it is important to explicitly sum the Keldysh indices instead of sampling them.

We note that, although the clusterization property is caused by the vacuum diagrams having zero contributions, these are not the only cancellations observed when summing

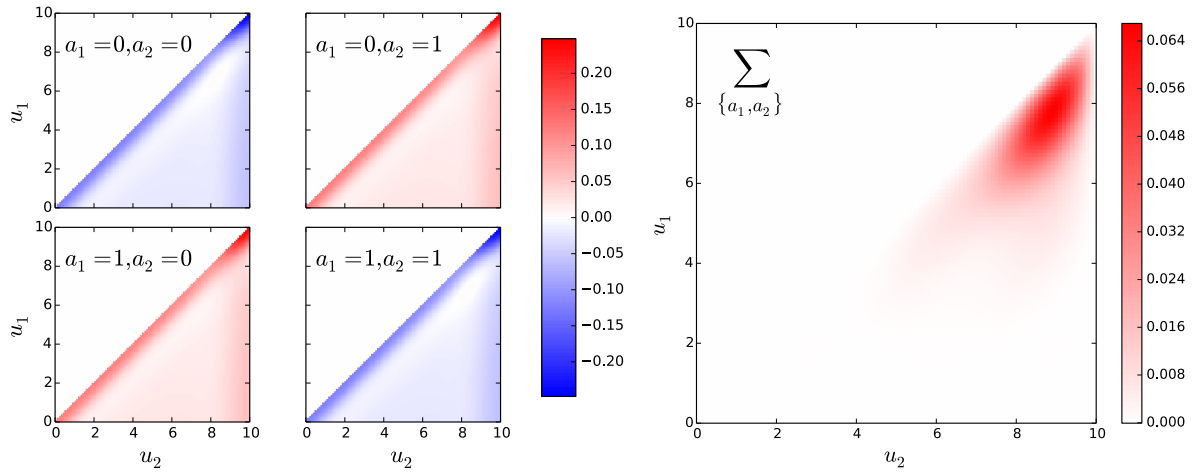

Figure 3.1: Comparison of the $n = 2$ integrand for $G^<(t = 10, t' = 10)$ before (left panel) and after (right panel) summing over Keldysh indices. Adapted from Ref. [128], where the system is the same as in chapter 5. Left panel shows the imaginary part of the integrands 3.15 for all choices of Keldysh indices a_1, a_2. The right panel shows the sum of them. Only the $u_2 > u_1$ part is shown, the other part can be recovered by symmetry.

over the Keldysh indices. Ref. [108] shows this in details, using a basis were vacuum diagrams are naturally absent, Moutenet *et al.* still found massive cancellations caused by the sum over Keldysh indices.

Computing a $(2n+1)\times(2n+1)$ determinant has a complexity proportional to n^3. We can reduce this cost by taking advantage from similarities between the 2^n determinants to be computed. Flipping a single Keldysh index changes only two lines and two columns of the determinant. From the previous determinant, a fast update algorithm — based on the Sherman–Morrison equality [127] — can obtain the new value with a complexity scaling as n^2 only. The Gray code ordering is used to go through all Keldysh indices values by flipping only one index at a time (see appendix C). As a result, the overall complexity of this Monte Carlo method scales as $2^n n^2$.

3.2.2 Sampling strategy

The structure of the Monte Carlo algorithm is based on the fact that Eq. 3.14 is a perturbation series:

$$G^{aa'}_{xx'}(t,t') = \sum_{n\geq 0} G_n U^n \tag{3.16}$$

Each coefficient contains an integral with increasing dimension with order n. We could make a different Monte Carlo for each coefficient, but a single Markov chain to sample the integration spaces of all coefficients at the same time is more efficient. In terms of diagrams, one goes from order n coefficient to $n+1$ by inserting a new vertex. If the first diagram has a strong contribution to G_n, it is likely that inserting a vertex would yield a diagram of strong contribution to G_{n+1} too. Thus, Profumo *et al.* used a Metropolis–Hastings algorithm which jumps between orders by inserting and removing vertices. This choice enhances acceptation ratio because of similarities between orders. It also limits

correlation if the chain frequently goes through the zero vertex state, which also ensures ergodicity.

The Monte Carlo method is used to perform the time integrals and sum over orbitals in Eq. 3.14. As we explained in the previous section, it is important to sum the Keldysh indices *explicitly*, and not to sample them. We therefore define a configuration $\mathcal{C}$ as:

- the order n_c,
- a set of times $\{u_k \in [0, t_{\mathrm{M}}]\}$ for $1 \leq k \leq n_c$,
- two sets of orbital indices $\{x_k\}$ and $\{y_k\}$ for $1 \leq k \leq n_c$.

We denote the Monte Carlo integrand as:

$$f(\mathcal{C}) \equiv \sum_{\{a_k\}} \prod_{k=1}^{n_c} \left[(-1)^{a_k} V_{x_k y_k}(u_k)\right] \left[\!\!\left[\begin{matrix} (x,t,a)\,, U_1, \ldots, U_{2n_c} \\ (x',t',a'), U_1, \ldots, U_{2n_c} \end{matrix} \right]\!\!\right] \tag{3.17}$$

The weight function is taken to be:

$$W(\mathcal{C}) \equiv U_{\mathrm{QMC}}^{n_c} \left| f(\mathcal{C}) \right| \tag{3.18}$$

and we denote $Z_{\mathrm{QMC}} = \sum_{\mathcal{C}} W(\mathcal{C})$ the normalization factor. U_{QMC} is a non-physical parameter which allows to adapt the amount of samples in each order. Note that order zero contains only one configuration and its weight is simply the non-interacting value of the correlator $|g^{aa'}_{xx'}(t,t')|$.

At each Monte Carlo step, $f(\mathcal{C})$ is evaluated and accumulated separately for each order. As the configuration space covers several orders, several quantities can be computed in the same Monte Carlo scheme. Namely, we compute:

$$\frac{U_{\mathrm{QMC}}^{n} G_n}{Z_{\mathrm{QMC}}} = \left\langle \delta_{n n_c} \frac{f(\mathcal{C})}{|f(\mathcal{C})|} \right\rangle_{W/Z_{\mathrm{QMC}}} \tag{3.19}$$

where $\langle \ldots \rangle$ stands for the statistical average over the probability $W(\mathcal{C})/Z_{\mathrm{QMC}}$. One can verify that G_n is the contribution to order U^n of the correlator $G^{aa'}_{xx'}(t,t')$.

We now need a way to evaluate Z_{QMC}. The Markov chain sampling all orders together is an elegant way to get rid of this normalization constant, without the pain to compute another multi-dimensional integral. If the sum of the weight function over some part of the configuration space is exactly known — here the order zero part — one only needs to measure the relative weight of this part to the whole space to obtain Z_{QMC}. This is easily measured by counting how many steps are spent in this part relatively to the whole space.

However, for this idea to accurately work, a substantial number of steps has to be spent in order zero. This requirement is in opposition with the need for many evaluations of the high order integrands. Indeed, the number of function evaluations required for a given error increases with order, which indicates that the complexity of the integrand increases with order too. Therefore, Profumo *et al.* constructed a "staircase" scheme: a sequence of Monte Carlo are run, each aiming at computing a different order n_{target} between 1 and $n_{\max}$, and each configuration space spans orders 0 to n_{target}. Each run aims at computing the ratio 3.19 and the relative weight of order n_{target} *versus* $n_{\mathrm{target}} - 1$. We include all orders $< n_{\mathrm{target}}$ to improve ergodicity. In each staircase run, U_{QMC} is

adjusted to make sure about half of function evaluations are spent in order n_{target} and a quarter in order $n_{\text{target}} - 1$. We indeed observed on most situations that the weight of configuration space evolves geometrically with order.

In practice, this scheme is performed as follows. We introduce:

$$c_n \equiv \sum_{\mathcal{C}} \delta_{nn_c} |f(\mathcal{C})| \tag{3.20}$$

the weight of order n normalized by U_{QMC}^n, so that c_n does not depend on this technical parameter. We also introduce:

$$p_n \equiv \langle \delta_{nn_c} \rangle \tag{3.21}$$

the overall probability to hit order n. p_n is estimated by counting the number of hits. The simple relation is verified:

$$p_n = U_{\text{QMC}}^n c_n / Z_{\text{QMC}} \tag{3.22}$$

As order zero weight is known exactly ($c_0 = |g_{xx'}^{aa'}(t,t')|$), the sequence of c_n is computed recursively from:

$$\frac{c_{n+1}}{c_n} = \frac{1}{U_{\text{QMC}}} \frac{p_{n+1}}{p_n} \tag{3.23}$$

c_n being independent of U_{QMC}, the different runs of the staircase scheme can use different values for U_{QMC}.

Each run of the staircase scheme also computes the average sign s_n at order n, by dividing the ratio 3.19 by p_n:

$$s_n \equiv \frac{1}{p_n} \left\langle \delta_{nn_c} \frac{f(\mathcal{C})}{|f(\mathcal{C})|} \right\rangle_{W/Z_{\text{QMC}}} \tag{3.24}$$

Note that data can be cumulated over all runs for this task to improve accuracy. Finally, the coefficient in U^n of the desired correlator is:

$$G_n = s_n c_n \tag{3.25}$$

3.2.3 Moves and detailed balance

The configuration space to sample is the space of a variable number of vertices, varying between 0 and n_{target}. This is very similar to the Fock space of identical quantum particles. To sample it, a Metropolis–Hastings algorithm is designed with two types of moves, with equal probability to be chosen.

- Insert a new vertex to go from order n to $n+1$. A new vertex $(u_{n+1}, x_{n+1}, y_{n+1})$ is created by choosing uniformly a random time $u_{n+1} \in [0, t_{\text{M}}]$ and random orbitals x_{n+1}, y_{n+1}. The overall probability to propose this move is:

$$\tilde{V}_{n\uparrow} \, \mathrm{d}u_{n+1} = \frac{\mathrm{d}u_{n+1}}{2t_{\text{M}} N_{\text{orb}}} \tag{3.26}$$

- Remove a vertex to go from order n to $n-1$. The vertex to be removed is selected uniformly in the list of n vertices in the starting configuration. The overall probability to propose this move is:

$$\tilde{V}_{n\downarrow} = \frac{1}{2n} \tag{3.27}$$

These moves are accepted with a probability $\eta_{n\uparrow}$ and $\eta_{n\downarrow}$, which should respect the detailed balance:

$$\tilde{V}_{n\uparrow}\,\mathrm{d}u_{n+1}\,\eta_{n\uparrow}P(\mathcal{C}_n)\prod_{i=1}^{n}\mathrm{d}u_i = \tilde{V}_{n+1\downarrow}\eta_{n+1\downarrow}P(\mathcal{C}_{n+1})\prod_{i=1}^{n+1}\mathrm{d}u_i \tag{3.28}$$

where $\mathcal{C}_n$ is a configuration at order n, and $P = W/Z_{\mathrm{QMC}}$. The Metropolis–Hastings algorithm prescribes:

$$\eta_{n\uparrow} = \min\left(1, \frac{\tilde{V}_{n+1\downarrow}P(\mathcal{C}_{n+1})}{\tilde{V}_{n\uparrow}P(\mathcal{C}_n)}\right) \tag{3.29}$$

$$\eta_{n\downarrow} = \min\left(1, \frac{\tilde{V}_{n-1\uparrow}P(\mathcal{C}_{n-1})}{\tilde{V}_{n\downarrow}P(\mathcal{C}_n)}\right) \tag{3.30}$$

Special cases occur for the "remove" move at order zero and the "insert" move at order n_{target}. As usually with the Metropolis–Hastings algorithm, a move going outside of the configuration space is properly handled by automatically refusing it [87]. These moves are however still proposed with the same probability as for valid ones.

3.3 Monte Carlo for the full Green's function

The previous algorithm, designed to compute the perturbation series of a single quantity, is now extended to compute the perturbation series of one of the kernels defined in chapter 2 on a whole time range. The Green's function is then deduced by convolution with the non-interacting Green's function.

Most of features are left unchanged. The configuration space, the moves and the staircase scheme are the same. The only differences lie on the choice of the weight and the quantities computed to replace s_n. This new Monte Carlo algorithm has been implemented using the TRIQS package [121].

3.3.1 Sampling of the kernel K

We first discuss the calculation of G using the kernel K. We rewrite Eq. 2.49 by explicitly separating the sum over Keldysh indices (which will be summed explicitly) and the sum over space and integral over time (which will be sampled using Monte Carlo). The kernel takes the form:

$$K(Y,X') = (-1)^b \sum_{n\geq 1}\int_0^{t_{\mathrm{M}}}\prod_{k=1}^{n}\mathrm{d}u_k \sum_{\{x_k,y_k\}}\sum_{p=1}^{2n}\sum_{a_p}(-1)^{a_p}\delta_c(Y,U_p)W_p^n(X',\{U_k\},a_p) \tag{3.31}$$

$$\begin{aligned} W_p^n(X',\{U_k\},a_p) \equiv \frac{i^n U^n}{n!}\left(\prod_{k=1}^{n}V_{x_k y_k}(u_k)\right)\sum_{\substack{\{a_k\}\\ k\neq p}}\left(\prod_{k\neq p}(-1)^{a_k}\right) \quad \times \\ (-1)^p\left[\!\!\left[\begin{matrix} U_1 & , U_2, \ldots\ldots\ldots, U_{2n} \\ (x',t',a'), U_1, \ldots \not{U_p} \ldots, U_{2n}\end{matrix}\right]\!\!\right] \end{aligned} \tag{3.32}$$

For practical purpose, the time integrals run over a finite interval $[0, t_M]$.

Using the same configurations $\mathcal{C}$ as in section 3.2.2, the kernel takes the form:

$$K(Y,X') = (-1)^b \sum_{\mathcal{C}} \left(\sum_{p=1}^{2n_c} \sum_{a_p} (-1)^{a_p} \delta_c(Y,U_p) W_p^{n_c}(X',\{U_k\},a_p) \right) \tag{3.33}$$

We observe that a single configuration provides contributions to K for $2n_c$ different points Y through the contour Dirac delta in the preceding expression. We choose the weight function to be:

$$W(\mathcal{C}) = \sum_{p=1}^{2n_c} \sum_{a=0,1} \left| W_p^{n_c}(X',\{U_k\},a) \right| \tag{3.34}$$

Noting $Z_{\mathrm{QMC}} \equiv \sum_{\mathcal{C}} W(\mathcal{C})$, the kernel can be rewritten as:

$$K(Y,X') = (-1)^b Z_{\mathrm{QMC}} \left\langle \sum_{p=1}^{2n_c} \sum_{a_p} (-1)^{a_p} \frac{W_p^{n_c}(X',\{U_k\},a_p)}{W(\mathcal{C})} \delta_c[(y,u,b),U_p] \right\rangle_{W/Z_{\mathrm{QMC}}} \tag{3.35}$$

where the average is taken over the distribution $W(\mathcal{C})/Z_{\mathrm{QMC}}$. Note that by construction, the weight $W(\mathcal{C})$ *controls* the measurement, *i.e.* $|W_p^{n_c}(X',\{U_k\},a)| \leq W(\mathcal{C})$. This is an essential property for a reweighting technique since it guarantees that the weight $W_p^{n_c}(X',\{U_k\},a)/W(\mathcal{C})$ does not diverge.

Each configuration $\mathcal{C}$ provides contributions to $2n_c$ values of $Y = (y,u,b)$ which are recorded by binning.

The partial weights $W_p^{n_c}$ possess an essential clusterization property, which generalizes the one for the Green's function discussed in section 2.1.2: if one or several times u_k goes far from t', then all $W_p^{n_c}$ go to 0. In other words the integrand is localized around t'. A detailed proof is provided in appendix D. The point $X' = (x',t',a')$ is kept fixed during the calculation to anchor the integral around this point.

Last, in order to calculate the factors W_p^n, we use the fact that they are made of the cofactors of the original matrix, hence can be rewritten as:

$$W_p^n(X',\{U_k\},a_p) = -\frac{i^n U^n}{n!} \left(\prod_{k=1}^{n} V_{x_k y_k}(u_k) \right) \sum_{\substack{\{a_k\} \\ k\neq p}} \left(\prod_{k\neq p} (-1)^{a_k} \right) \quad \times \\ \left[\!\!\left[\begin{matrix} X, U_1, \ldots, U_{2n} \\ X', U_1, \ldots, U_{2n} \end{matrix} \right]\!\!\right]_{p1}^{-1} \times \left[\!\!\left[\begin{matrix} X, U_1, \ldots, U_{2n} \\ X', U_1, \ldots, U_{2n} \end{matrix} \right]\!\!\right] \tag{3.36}$$

This last form is very convenient since a single Wick matrix (and its inverse) need to be stored and monitored during the calculation.

A last comment is needed about the c_n sequence. Adapting Eq. 3.20, it is now defined as $c_n \equiv \sum_{\mathcal{C}} \delta_{nn_c} W(\mathcal{C})/U_{\mathrm{QMC}}^n$. As order $n = 0$ is irrelevant to the kernel, the $n = 0$ weight is set to 1 as a default value, so that c_0 is now a constant $c_0 = 1$.

Toward the frequency domain: an illustration

To illustrate, we anticipate on application to the Anderson impurity model from chapter 5. We present the numerical data obtained with this QMC for the kernel K. The top raw of Fig. 3.2 shows an example of the bare data for the retarded kernel $K^R(t)$ as

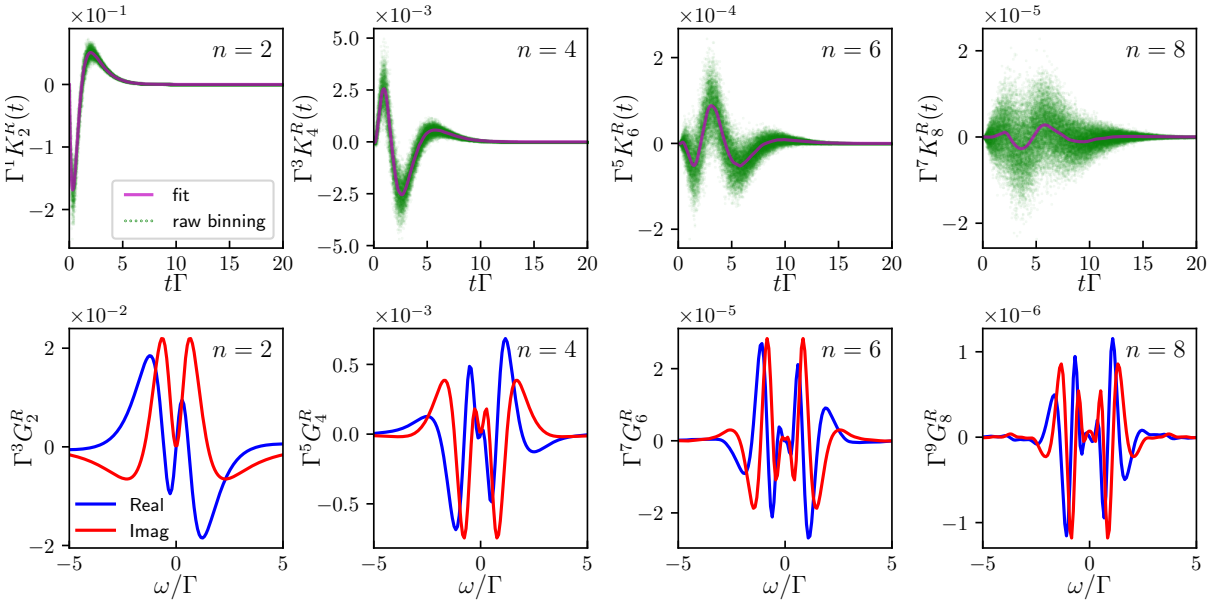

Figure 3.2: First non-zero orders of the retarded kernel in time (top row), and corresponding retarded Green's function in frequency (bottom row, same data as in Fig. 1.6), for the particle-hole symmetric Anderson impurity model at equilibrium (see chapter 5). The green dots in the top row correspond to the raw data of the binning with apparent noise arising at high frequencies. The purple lines are a fit of the kernel, shown for illustration purpose only, where the high frequency noise has been subtracted by smearing the cumulative function of the kernel. Maximum time is $t_M = 20/\Gamma$. One can see (upper right panel) that at order $n = 8$ a lower integration time would not capture the whole kernel, thus the steady state would not be reached.

they come out of the calculation for order U^2, U^4, U^6 and U^8 (left to right). Note that the noise in these data is mostly apparent, it corresponds to noise at very high frequency. This apparent noise reflects the fact that we have binned the curve $K^R(t)$ into a very fine grid (50 000 grid points in this calculation). An even finer grid would show even more apparent noise (since there would be even less Monte Carlo points per grid point). The corresponding cumulative function $\int_0^t K^R(u)du$ is however noiseless as can be seen from the example shown in Fig. 3.3 for $n = 8$.

The next step is to make a Fourier Transform of $K_n^R(t)$ (not shown). The resulting $K_n^R(\omega)$ is relatively noisy at high frequency. Last, we obtain $G_n^R(\omega) = g^R(\omega)K_n^R(\omega)$ for $n \geq 1$ (from Eq. 2.70) as shown in the bottom row of Fig. 3.2. The factor $g^R(\omega)$, which decays at high frequency, very efficiently suppresses the high frequency noise of the kernel data. The same noise-reduction mechanism has been reported in *e.g.* Ref. [44] in the context of auxiliary-field Monte Carlo. We emphasize one aspect of these data which is rather remarkable: even though the eight order contribution $G_8^R(\omega)$ is the result of an eight dimensional integral and is more than four orders of magnitude smaller than the second order contribution $G_2^R(\omega)$, it can be obtained with high precision (the error bars are of the order of the thickness of the lines here). This is due to the recursive way these integrals are calculated as discussed in section 3.2.2.

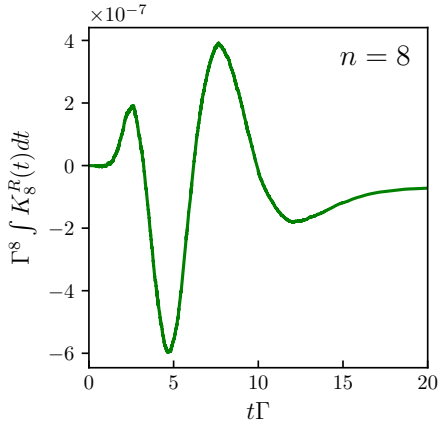

Figure 3.3: Cumulative function $\int_0^t K_8^R(u)\,\mathrm{d}u$ obtained by integrating the raw data of the upper right panel of Fig. 3.2. Taking the integral gets rid of the apparent noise of the raw data whose origin is simply the presence of the binning grid in time.

3.3.2 Sampling of the kernel L

Following the same route for L as was done for K, we can write:

$$L^{ba'}_{yx'z}(u,t') = (-1)^b \sum_{n\geq 1} \int \prod_{k=1}^{n} \mathrm{d}u_k \sum_{\{x_k,y_k\}} \sum_{p=1}^{2n} \sum_{a_p} (-1)^{a_p} \delta_c[(y,u,b),U_p] W^n_{p+2}(X',\{U_k\},a_p,z) \tag{3.37}$$

$$W^n_{p+2}(X',\{U_k\},a_p,z) \equiv \frac{i^n U^n}{n!} \left(\prod_{k=1}^{n} V_{x_k y_k}(u_k)\right) \sum_{\substack{\{a_k\}\\ k\neq p}} \left(\prod_{k\neq p} (-1)^{a_k}\right) \times (-1)^{p+1} \left[\!\!\left[\begin{matrix} (z,t',a'), & U_1 & ,U_2,\ldots\ldots,U_{2n} \\ (x',t',a'),(z,t',a'), & U_1,\ldots & \not{U_p}\ldots,U_{2n} \end{matrix} \right]\!\!\right] \tag{3.38}$$

thus defining W^n_p for $p = 3,4,\ldots,2n+2$. We also define W^n_1 and W^n_2 in the following way:

$$W^n_1(X',\{U_k\},z) \equiv -\frac{i^n U^n}{n!} \sum_{\{a_k\}} \left(\prod_{k=1}^{n} (-1)^{a_k} V_{x_k y_k}(u_k)\right) \left[\!\!\left[\begin{matrix} (z,t',a'),U_1,\ldots,U_{2n} \\ (z,t',a'),U_1,\ldots,U_{2n} \end{matrix} \right]\!\!\right] \tag{3.39}$$

$$W^n_2(X',\{U_k\},z) \equiv \frac{i^n U^n}{n!} \sum_{\{a_k\}} \left(\prod_{k=1}^{n} (-1)^{a_k} V_{x_k y_k}(u_k)\right) \left[\!\!\left[\begin{matrix} (z,t',a'),U_1,\ldots,U_{2n} \\ (x',t',a'),U_1,\ldots,U_{2n} \end{matrix} \right]\!\!\right] \tag{3.40}$$

These two extra values are necessary to compute $G^<_{zz}(t',t')$ and $G^<_{zx'}(t',t')$, which are needed to obtain F, as can be seen in Eq. 2.56. Moreover, they do not require extra computation time, as they are a direct by-product of the computation of the W^n_p for $p > 2$. Indeed, in the same spirit as Eq. 3.36, the determinant within any W^n_p (for $p = 1,\ldots,2n+2$) can be replaced by:

$$(-1)^{p+1} \left[\!\!\left[\begin{matrix} X,(z,t',a'),U_1,\ldots,U_{2n} \\ X',(z,t',a'),U_1,\ldots,U_{2n} \end{matrix} \right]\!\!\right]^{-1}_{p1} \times \left[\!\!\left[\begin{matrix} X,(z,t',a'),U_1,\ldots,U_{2n} \\ X',(z,t',a'),U_1,\ldots,U_{2n} \end{matrix} \right]\!\!\right] \tag{3.41}$$

Again, a single Wick matrix is needed to get contributions to all W^n_p (given a set of Keldysh indices), which is very convenient.

Configurations are defined in the same way as in the previous section, but the weight of a configuration $\mathcal{C}$ is now:

$$W(\mathcal{C}) = |W^{n_c}_1(X',\{U_k\},z)| + |W^{n_c}_2(X',\{U_k\},z)| + \sum_{p=1}^{2n_c} \sum_{a=0,1} \left|W^{n_c}_{p+2}(X',\{U_k\},a,z)\right| \tag{3.42}$$

We define again $Z_{\mathrm{QMC}} \equiv \sum_{\mathcal{C}} W(\mathcal{C})$ (which however has a different value than in the previous section). Finally, L can be written as:

$$L^{ba'}_{yx'z}(u,t') = (-1)^b Z_{\mathrm{QMC}} \left\langle \sum_{p=1}^{2n_c} \sum_{a_p} (-1)^{a_p} \frac{W^{n_c}_{p+2}(X', \{U_k\}, a_p, z)}{W(\mathcal{C})} \delta_c[(y,u,b), U_p] \right\rangle_{W/Z_{\mathrm{QMC}}} \tag{3.43}$$

and, from Eq. 2.31, we get that the values of $G^<_{zz}(t',t')$ and $G^<_{zx'}(t',t')$ (needed to compute F) are:

$$G^<_{zz}(t',t') = - Z_{\mathrm{QMC}} \left\langle \frac{W^{n_c}_1(X', \{U_k\}, z)}{W(\mathcal{C})} \right\rangle_{W/Z_{\mathrm{QMC}}} \tag{3.44}$$

$$G^<_{zx'}(t',t') = Z_{\mathrm{QMC}} \left\langle \frac{W^{n_c}_2(X', \{U_k\}, z)}{W(\mathcal{C})} \right\rangle_{W/Z_{\mathrm{QMC}}} \tag{3.45}$$

The Monte Carlo algorithm used to evaluate these averages is the same as in the previous section, except for the weight $W(\mathcal{C})$.

Comparison between the L and the K kernel methods

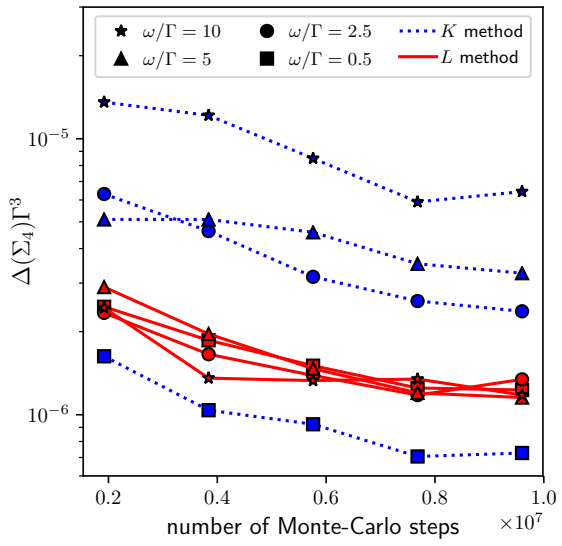

Figure 3.4: Statistical error of $\Sigma^R_4(\omega)$ in the particle-hole symmetric Anderson impurity model at equilibrium (see chapter 5), with increasing number of Monte Carlo steps. The K kernel method (dotted lines) and the L kernel method (plain line) are compared for different frequencies (different symbols). The error with the L method is constant with frequencies, whereas the K method accuracy worsen with increasing ω. At large frequencies ($\omega > \Gamma$) the error is smaller when using the L method.

We also computed the L kernel in the Anderson impurity model of chapter 5. The bare data is very similar to the one obtained with the kernel K method. By construction, the reconstruction of G with L involves $G_n(\omega) \sim g(\omega)^2 L_{n-1}(\omega)$ so that the high frequency noise is expected to behave better with L than with K (the factor $g(\omega)^2$ effectively suppresses the high frequency). This is particularly apparent in the retarded self-energy $\Sigma^R(\omega)$, which is defined from the (non-interacting and full) retarded Green's functions (g^R and G^R) as:

$$\Sigma^R(\omega) \equiv \frac{1}{g^R(\omega)} - \frac{1}{G^R(\omega)} \tag{3.46}$$

Fig. 3.4 shows a comparison of the errors obtained on $\Sigma^R_4(\omega)$ using the two methods. We find that the error using the L method is essentially frequency independent while the

error with the K method depends strongly on frequency. In most cases the L method is preferred, but at small frequency we have observed that the K method can provide smaller error bars.

Chapter 4

Summing diverging perturbation series

We presented so far a QMC algorithm to solve non-equilibrium quantum many-body problems. But it really provides only half of the solution, as it only yields truncated perturbation series F_0, F_1, ..., F_N in the interaction strength U of a physical quantity F, such as shown in Fig. 1.6 (page 25) where $F \equiv G^R$. In this chapter we construct a method to obtain physical quantities as functions of U from such power expansion.

The series formally defines the quantity F in the sense that:

$$F(U) = \sum_{n=0}^{+\infty} F_n U^n \tag{4.1}$$

whenever the sum converges. This is numerically correct in the perturbative regime, where $|U|$ is smaller than the convergence radius of the series R_F. Then, summing the series up to order N gives an accurate estimate of $F(U)$, with an error decreasing exponentially with N (like a geometric series since $F_n \sim (1/R_F)^n$). But for strong interaction $|U| > R_F$, the series diverges. Nevertheless, the series is not meaningless, and physical values can be recovered by various resummation methods.

Note that in some problems like the unitary Fermi gas, the series has a zero radius of convergence. We will not consider these cases, as they require other techniques than the ones presented here, *e.g.* Borel summation techniques [140].

For a given physical quantity F, we want to evaluate $F(U)$ from the first $N \sim 10$ coefficients of its Taylor series in $U = 0$. In the following, F will stand for the width of the Kondo peak, the Green's function G or the self-energy Σ of the impurity (defined precisely in chapter 5). In the latter cases, the coefficients are functions of the frequencies, $G_n(\omega)$ and $\Sigma_n(\omega)$. In the cases considered in this work (quantum impurity models), and in general for lattice models at finite temperature (such as the Hubbard model), the series for F is expected to have a non-zero radius of convergence R_F. Note that R_F not only depends on the chosen physical quantity F, but may also depend on frequency, voltage, temperature, *etc.*

The mathematical problem of series resummation is a quite old topic, (see *e.g.* Ref. [56]). Various techniques have been used in physics problems including Padé approximants [16], Lindelöf extrapolation [97, 166] or Cesàro-Riesz technique [129]. In diagrammatic QMC, this is typically a post-processing step: the Monte Carlo produces the values of the various orders of the expansion, and one then attempts to sum the series to obtain the final result. However, the situation is quite different if we want to use such technique to solve

quantum impurity models in the context of quantum embedding methods like DMFT. Indeed, in such cases, the method require multiple solutions of impurity model to solve their self-consistency loop. Therefore, it is necessary to develop more robust methods to sum the perturbative series for impurity systems, which could be automatized.

We also want to know, for a given physical quantity F and interaction U, how many orders N_0 are needed to obtain $F(U)$ at a given precision. Since the cost of the diagrammatic QMC approach is exponential in N_0, the answer to this question gives the ultimate limit of the method.

In this work, we consider the series summation problem as the problem of reconstructing the function $F(U)$ in the complex U plane. The divergence of the series is due to the presence of singularities in the complex U plane, starting on the circle $|U| = R_F$. The question is to reconstruct F *beyond* the radius of convergence.

4.1 General theory

To extrapolate perturbation series out of their convergence disk in a reliable way, we designed a three features method based on elementary complex analysis and bayesian inference. The first axis of the method is the transformation of the series through a smooth change of variable $U \to W$ *via* a conformal transform of the U complex plane. Such tranformations can radically change the analytical structure of the series and bring points inside the convergence disk. The second feature is the detection of poles in the U complex plane, which are, alongside more complex singularities, responsible for the finite convergence radius. This is necessary to control the choice of the conformal transform. The last feature is the addition of non-perturbative information using bayesian inference. Extra information allows to avoid the explosion of error bars during the resummation. Although this step is optionnal, it appeared very powerful and critical when extrapolating quantites to infinite U.

The technique is first described in details and then illustrated on the Kondo temperature series for the Anderson impurity model.

4.1.1 Conformal transforms in the U complex plane

Conformal transformations can be used to deform the complex plane and bring points of interest into the convergence disk of the transformed series. This technique was used a long time ago *e.g.* in statistical physics [49]. In [128], Profumo *et al.* have shown that a simple conformal Euler transform allows to compute the density on the impurity up to $U = \infty$, at very low temperature, from the first 12 coefficients of the series. However, this Euler transform is not always successful in resumming other quantities like the Green's function and the self-energy, and needs to be generalized.

Suppose that we aim at evaluating $F(U)$ at $U = U_0$ with U_0 real, positive and $U_0 > R_F$. First, we assume a *separation property*, *i.e.* that we can find a simply connected domain delimited by a curve $\mathcal{C}$ containing 0 and U_0 but no singularities of the function F, as illustrated in the left panel of Fig. 4.1. The singularities of the function $F(U)$ are located outside the domain $\mathcal{C}$. We then proceed as follows:

- First, according to the Riemann mapping theorem, we can construct a biholomorphic change of variable $W(U)$ such that *i)* $W(0) = 0$, *ii)* it maps the interior of $\mathcal{C}$ into a disk $D_{\mathcal{C}}$ centered at 0 in the W plane (see the right panel in Fig. 4.1). In

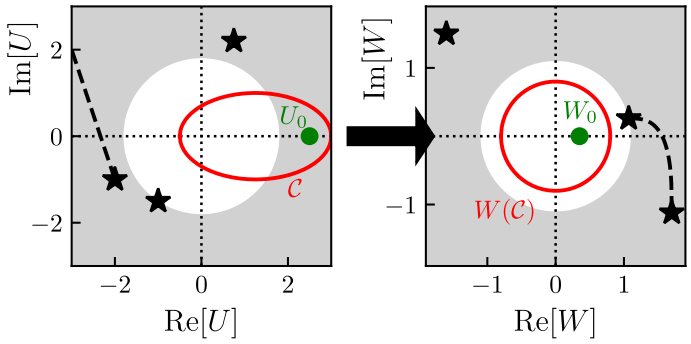

Figure 4.1: Illustration of the general computation scheme developed in this work. A physical quantity $F(U)$ (*e.g.* the current through a quantum dot) presents singularities in the U complex plane (left panel), such as poles (stars) or branch cuts (dashed line), hampering proper convergence of perturbative approaches for values of U outside the convergence disk (grey area). After defining a broad singularity-free contour $\mathcal{C}$ (red line) that encircles both $U = 0$ and a targeted U_0 value, a conformal map $U \to W(U)$ is defined in order to bring $W_0 = W(U_0)$ inside the convergence disk of $F[U(W)]$ (right panel). Resummation techniques can then be applied in a controlled way.

---

practice, we seek $\mathcal{C}$ to separate the singularities from the half straight line of real positive U. In the following, we will use two simple transformations, but in general we could use a Schwarz–Christoffel map if $\mathcal{C}$ is a polygon [35], composed with a Möbius transformation of the disk to enforce *i)* .

- Second, we form the series for the reciprocal function $U(W)$ of $W(U)$ which is defined term by term by the equation $U(W(U)) = U$. We then construct the series $\bar{F}(W) \equiv \sum_p \bar{F}_p W^p$ defined by the composition $\bar{F}(W) = F(U(W))$. Since $W(0) = 0$, the first N terms of $F(W)$ can be computed from the first N terms of $F(U)$.

- We evaluate the series $\bar{F}(W_0)$ at the point of interest $W_0 = W(U_0)$. Indeed, by construction $W_0 \in D_{\mathcal{C}}$ and, since $\bar{F}(W)$ is holomorphic in $D_{\mathcal{C}}$, $D_{\mathcal{C}}$ is included in the convergence disk of the series $\bar{F}$. Hence the series $\bar{F}$ converges at W_0.

The result is independent of the choice of the domain $\mathcal{C}$ but the speed of convergence of the series for $\bar{F}(W_0)$ versus N is not, since it is determined by the relative position of W_0 compared to the radius of convergence $R_{\bar{F}}$ of $\bar{F}$, *i.e.* $\eta_{\mathcal{C}} \equiv |W_0/R_{\bar{F}}|$. Therefore, there are ways to optimize the domain $\mathcal{C}$. For example, we can not simply take a narrow domain close to the real axis, for the convergence in W would be very slow: we need to have U_0 and 0 as "far" as possible from the curve $\mathcal{C}$ (the precise meaning of "far" being given by $\eta_{\mathcal{C}}$). For each domain $\mathcal{C}$ satisfying the separation property, there is a minimum number of orders $N_{\mathcal{C}}$ needed to obtain the result at a given precision ϵ. There is therefore an optimal domain, which minimize $N_{\mathcal{C}}$ to $N_{opt} = \min_{\mathcal{C}} N_{\mathcal{C}}$. This is the absolute minimum of orders needed to sum the series, and therefore determine *in fine* the complexity of the diagrammatic QMC algorithm. Our next goal will be to approach such optimum.

Note that a failure of the separation assumption, *i.e.* the choice of a domain containing singularities, may result simply in the divergence of the series $\bar{F}$ at W_0, hence a clear

failure of the method rather than a wrong result. Conversely the study of the convergence radius of the $\bar{F}(W)$ series provides direct information on the singularity-free regions of the U plane. Indeed, the region of the U plane that maps towards the inside of the convergence radius of $\bar{F}(W)$ are singularity/branch cut free. Hence, using several conformal transforms, one may perform a step by step construction of the domain $\mathcal{C}$. Another note is that, as a consistency check, one can also check the stability of the final result upon small deformations of the domain (or the $W(U)$ function), as was discussed in details in Ref. [128] for the Euler transform.

The existence of the domain $\mathcal{C}$ and the transformation $W(U)$ has a direct consequence on the algorithmic complexity of diagrammatic Quantum Monte Carlo. It was shown in Ref. [141] that, for values of U *inside* the convergence radius, connected diagrammatic quantum Monte Carlo techniques provide a systematic route for calculating the many-body quantum problem in a computational time that only increases *polynomially* with the requested precision. The result also applies to the Keldysh diagrammatic QMC. The core of the argument of Ref. [141] is as follows: inside the radius of convergence R, the precision of a calculation ϵ increases exponentially with the number of orders N used $\epsilon \sim (U/R)^N$. Hence, although the computational time C increases exponentially with N, $C \sim a^N$, the overall computational time scales as $C \sim (1/\epsilon)^{\log a/\log(R/U)}$, *i.e.* polynomially. For a given U_0 and domain $\mathcal{C}$, we now have to sum the transformed series $\bar{F}$ inside the radius of convergence. Hence the same argument also apply for this series, and therefore we conclude that, *even outside the disk of convergence*, we expect the algorithm to have a polynomial complexity as a function of the precision. Let us emphasize however that this result is largely academic, since in practice the power law can be large. Moreover, as we will discuss, for some physical quantities the transformation to W can lead to a dramatic increase of the noise which induces a large computation time for a given precision.

4.1.2 Location of singularities in the U complex plane

In order to choose $\mathcal{C}$ properly, we need to have some information on the location of the singularities in the U plane. We use the following technique to approximately locate the poles of $F(U)$ in the complex plane:

- We form an inverse of F of the form $K(U) = 1/(F(U) + a)$ as a formal series (*i.e.* order by order). a is a constant that we choose at our convenience. In order for the series $K(U)$ to exist, we must have $F_0 + a \neq 0$.

- We estimate the radii of convergence R_F (resp. R_K) of F (resp. K), by plotting $|F_n|$ and $|K_n|$ versus n, and fitting the asymptote $|F_n| \sim (1/R_F)^n$.

- In most of situations we found $R_F \neq R_K$. If not, we used a different a so as to obtain $R_F \neq R_K$. Without loss of generality, let us assume that R_K is the largest. We use the truncated polynomial of the series, $\sum_{p=0}^{N} K_p U^p$ to compute $K(U)$ within its disk of convergence and therefore locate its zeros, which are the poles of F. They will appear as the accumulation of the zeros of the polynomials at large enough N. If $R_F > R_K$, we simply reverse the roles of the series and reconstruct $K(U)$.

This technique has a quite large degree of generality, but also limitations. It assumes for example that the leading singularities in F are poles and that the radius of convergence of F and K are different. Also it does not give us indications of poles that would be far

from the origin but close to the real axis. However, in practice, we will see below that for the quantities and the physical problem considered in this work (Green's function and self-energy in real frequency, and Kondo temperature), this technique is sufficient. Finally, once $F(U)$ has been resummed, it can be used to locate its zeros, hence for the resummation of $K(U)$ which provides another consistency check of the method.

4.1.3 Controlling noise amplification with Bayesian inference

The transformation from F_n to $\bar{F}_p$ is a linear one (with a lower triangular matrix), for a given transformation $W(U)$. Depending on the eigenvalues of the corresponding matrix, the Monte Carlo error bar in F_n may be strongly amplified by the transformation. As a result, the method may become unusable at strong coupling, as will be illustrated below in section 4.2.3.

However, if we add some *non-perturbative information*, such as the fact that the Kondo temperature vanishes at infinite U, or a sum rule, we can construct a Bayesian inference technique that may be used to decrease the statistical uncertainty. Bayesian inference provides a systematic and rigorous way to incorporate this information into the results and improve their accuracy.

Consider a series $F(U) = \sum_{n=0}^{N} F_n U^n$ where the F_n are known with a finite precision. We note $F = \{F_0, F_1, \dots F_N\}$ the corresponding (vectorial) random variable. We calculate the mean values and the errors of the F_n within the quantum Monte Carlo technique. We assume that the coefficients F_n are given by independent Gaussian variables. This forms the "prior" distribution $P_{\text{prior}}(F = f)$ in the absence of additional information. Let us note the additional information X. X is a random variable that can be directly calculated from the series, $X = g(F)$ but whose actual value is also known very precisely by other means. In the example below, X will be the value of $F(U)$ at large U. Bayesian inference amounts to replacing the prior distribution with the posterior distribution $P(F = f|X = x_0)$ that incorporates the knowledge of the actual value of X (we note $P(A|B)$ the conditional probability of event A knowing event B). The value of X is often known exactly. However, due to the presence of truncation errors, its value cannot be enforced exactly, and we suppose that it is known with a small error ε. Eventually, we take the limit $\varepsilon \to 0$. Hence, we assign to X a Gaussian probability distribution $P_X(X = x) = 1/(\varepsilon\sqrt{2\pi}) \exp[-(x - x_0)^2/(2\varepsilon^2)]$ and define the posterior distribution as:

$$P_{\text{posterior}}(F = f) \equiv \int dx P(F = f|X = x) P_X(X = x) \tag{4.2}$$

Using Bayes formula $P(F = f|X = x) = P(X = x|F = f) P_{\text{prior}}(F = f)/P_{\text{prior}}(X = x)$ and the deterministic relation $P(X = x|F = f) = \delta[x - g(f)]$, one arrives at:

$$P_{\text{posterior}}(F = f) = \frac{P_X(X = g(f)) P_{\text{prior}}(F = f)}{P_{\text{prior}}(X = g(f))} \tag{4.3}$$

In practice, one proceeds as follows: (i) one generates many series according to $P_{\text{prior}}(F = f)$ (this is straightforward since all the coefficients are assumed to be Gaussian and independent). (ii) One construct a histogram of the values of X to obtain $P_{\text{prior}}(X = g(f))$. (iii) Each series is given a weight $P_X(X = g(f))/P_{\text{prior}}(X = g(f))$ which is used to calculate other observables such as the value of $F(U)$ at different values of U. In practice the results are insensitive to the choice of ε as long as it is chosen large enough so that a finite fraction of the sample contributes to the final statistics.

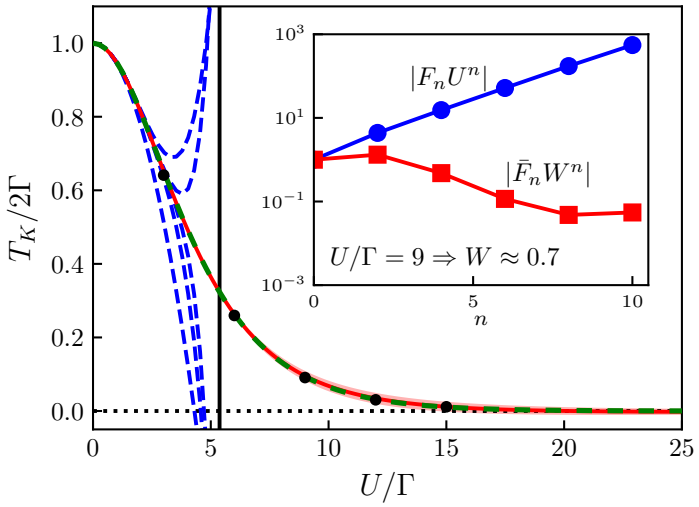

Figure 4.2: Resummation of the Kondo temperature (as defined in Eq. 4.4) in the particle-hole symmetric Anderson impurity model defined in chapter 5. Plain red line: resummation technique including Bayesian inference, using the Euler transform (error bar shown as red shaded area); dashed thick green line: exact result from Bethe ansatz [69]; black circles: reference NRG results; dashed blue lines: truncated series including up to $N = 2, 4, 6, 8$ and 10 terms. The vertical line shows the estimated convergence radius of the series. Inset: evolution of F_nU^n with n for $U = 9\Gamma$ in log-linear scale (blue circles); evolution of the series $\bar{F}_nW^n$ obtained after conformal transformation (red squares). The value $W = 0.7$ is obtained by applying the conformal transformation to $U = 9\Gamma$. The $\bar{F}_nW^n$ decreases exponentially, indicating convergence of the transformed series while the original series (blue circles) diverges.

4.2 Illustration with the Kondo temperature

To illustrate the method, we anticipate the QMC calculation of the series for the Kondo temperature T_K in the particle-hole symmetric Anderson impurity model presented in the next chapter. In this section T_K corresponds to F. T_K is roughly the width of the low energy Kondo peak, and is defined more specifically in this work as the dimensionful Fermi liquid quasi-particle weight extracted from the retarded self-energy at low energy:

$$T_\mathrm{K}(U) \equiv \frac{2\Gamma}{1 - \partial_\omega \mathrm{Re}\Sigma^R(U,\omega)|_{\omega=0}}. \tag{4.4}$$

Our first goal is to illustrate how the method actually works, and benchmark it against the calculation of the same quantity from the Numerical Renormalization Group (NRG) technique and Bethe ansatz [69]. Details of the NRG implementation can be found in section 5.2.2.

4.2.1 Singularities in the U complex plane

The dashed blue lines of Fig. 4.2 shows the truncated series of $T_\mathrm{K} = \sum_{n=0}^{N} F_nU^n$ for various orders $N \leq 10$. These truncated series diverge around $R_{T_\mathrm{K}} \approx 5\Gamma$ which is the

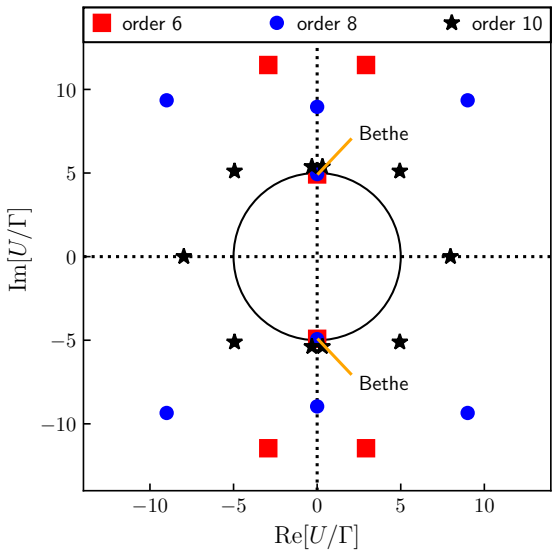

Figure 4.3: Poles of $T_K(U)$ identified from the zeros of the $1/T_K(U)$ function. These are found by looking for the zeros of its truncated series. Here they are shown in the U/Γ complex plane with truncation at order 6 (red squares), 8 (blue points) and 10 (black stars). The black circle corresponds to $|U| = R_{T_K}$ where R_{T_K} is the radius of convergence of the series of T_K. The stable points close to $\pm i5\Gamma$ correspond to true non-perturbative poles of $T_K(U)$. The exact zeros (small orange arrows) have been computed from the exact $1/T_K$ series found with Bethe ansatz [69].

convergence radius of the series for these parameters. Increasing the value of N helps to obtain a reliable value of T_K closer to R_{T_K}. However, as expected, even with a very large number of terms, the bare series cannot be summed near or above R_{T_K}. Anticipating the final results, the plain red line corresponds to the results after resummation which matches very well what was obtained with our benchmark NRG calculation.

The inset of Fig. 4.2 shows the value of $|F_n U^n|$ (blue circles) as a function of n for $U/\Gamma = 9$ which lies above the convergence radius of the series. The log-linear plot shows an exponential increase of $|F_n U^n| \sim (U/R_{T_K})^n$ with n which we use to extract the convergence radius of the series. Note that for other series, it can happen that $|F_n|$ oscillates with n. Whenever F_n changes sign, it becomes close to zero which provides deviations from the clear exponential behaviour shown in the inset of Fig. 4.2. Hence, to obtain convergence radii which are robust to these outliers, we used a robust regression method on the $\log|F_n|$ versus n data (we compute the regression slope as the median of all slopes between pairs of data points, this is known in statistics as the Theil-Sen estimator [163]).

We now compute the first 10 terms of the series of $1/T_K(U)$. This series has a radius of convergence of the order of 10Γ. We look for the zeros, in the complex plane, of the series $1/T_K(U)$ truncated at order N. Since the truncated series is a polynomial, it has (generically) N zeros, which are shown in Fig. 4.3 for $N = 6$ (red squares), $N = 8$ (blue circles) and $N = 10$ (stars). One pair of zeros $U \approx \pm i5\Gamma$ is converged for all the truncations, hence corresponds to a true zero of $1/T_K(U)$, *i.e.* to a pole of $T_K(U)$. Fig. 4.3 also shows the circle $|U| = R_{T_K}$ extracted from the analysis of the $T_K(U)$ series done in the inset of Fig. 4.2. We find that the two poles $\pm i5\Gamma$ do indeed lie right on this circle.

4.2.2 Conformal transform

We now turn to the conformal transformation $W(U)$, which maps the two poles $\pm i5\Gamma$ away and brings the values of interest $U > 0$ (real) closer to zero. We illustrate the

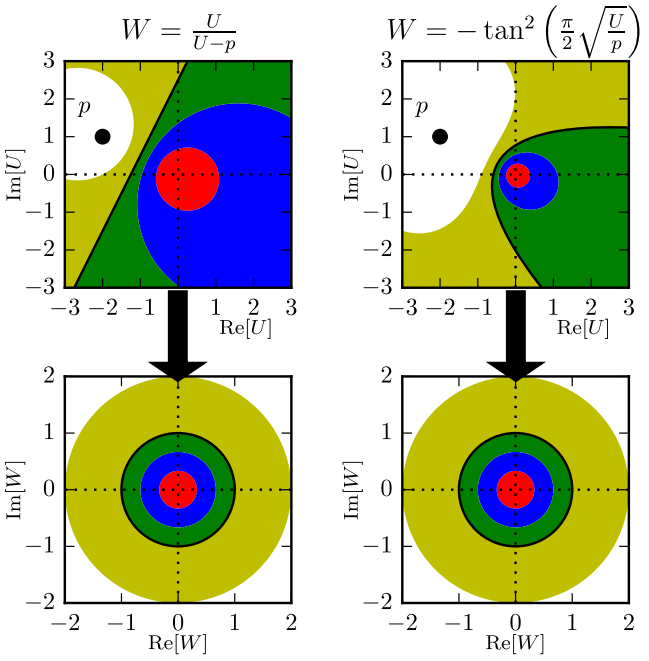

Figure 4.4: Left panels: Euler map. Right panels: parabola map. Upper panels: complex U plane. Lower panels: complex W plane. The transformation maps the upper regions of various colors onto the lower regions of matching colors. In particular the thick straight line (upper left) and the parabola (upper right) are mapped onto the unit circles (lower left and right respectively).

technique with two maps: the Euler map defined by

$$W = \frac{U}{U-p} \tag{4.5}$$

and the "parabola" map which is defined as

$$W = -\tan^2\left(\frac{\pi}{2}\sqrt{\frac{U}{p}}\right) \tag{4.6}$$

where p is an adjustable complex parameter.

Fig. 4.4 shows the various regions (different colors) in the U plane that are mapped onto concentric disks of the W plane. 0 is mapped onto 0 and p onto ∞ in both transforms. The Euler map (left column) maps one half of the plane into the unit disk and the other half into the outside of the unit disk (separated by a black line). The parabola transform (right column) maps the inside of a parabola (black line) into the unit disk and the outside of the parabola into the outside of the unit disk. In the case where there are no singularities on the positive half plane $\mathrm{Re}[U] > 0$, the Euler transform should be preferred since real values of $U > 0$ are typically mapped closer to $U = 0$ than with the parabola transform (compare the size of the blue region of the parabola and Euler case for instance). However, the parabola map is more agnostic about the positions of the singularities and will work even if there are singularities on the positive half plane $\mathrm{Re}[U] > 0$ as long as they lie outside the parabola.

We now perform the resummation of $T_\mathrm{K}(U)$. The series contains only even power of U due to particle-hole symmetry, so that it can be considered as a function of U^2. The two poles $U = \pm i5\Gamma$ correspond to a single one $U^2 = -25\Gamma^2$. In the U^2 plane, the pole being on the negative real axis, the Euler maps works very effectively. The resummation can also be performed with the parabola transform.

Once the conformal map is selected, we form the series $\bar{F}_p$ in the W variable, as explained above. The inset of Fig. 4.2 shows $\bar{F}_n W_0^n$ (red squares) as a function of n

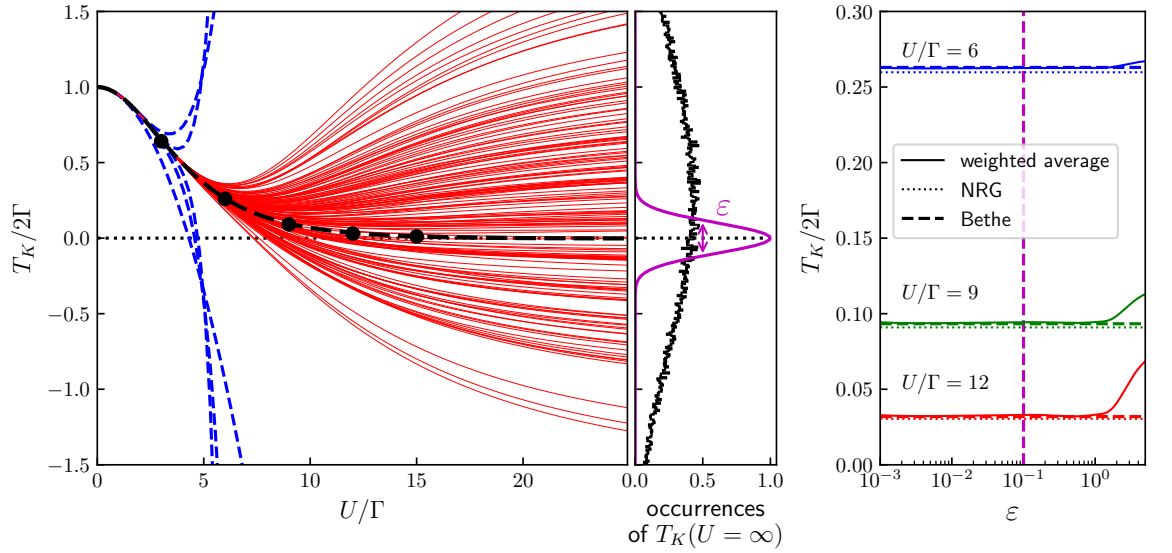

Figure 4.5: Reduction of the statistical noise on the resummed $T_{\rm K}(U)$ series by Bayesian inference. Left panel: Kondo temperature as a function of U. The bundle of red lines correspond to different samples of our series after resummation (see text). The thick line shows the final result after Bayesian inference while the circles show our reference NRG calculations. The dashed blue lines show the bare results without resummation, which diverge for $U > 5\Gamma$. Middle panel: histogram of the values of $T_{\rm K}(U = \infty)$ obtained from our samples (black line), histogram of its assumed distribution with tolerance ε (purple line). Right panel: final result after inference as a function of ε for three values of $U/\Gamma = 6, 9$ and 12 (thin lines), reference NRG result (dotted lines).

for $W_0 = 0.7 = W(U_0 = 9\Gamma)$, using the Euler map with $p = -35\Gamma^2$ (the parabola yields similar results with $p = -15\Gamma^2$). As expected, U_0 is way beyond the radius of convergence in the original variable U, while W_0 lies within the disk of convergence of $\bar{F}(W)$ whose radius is found to be $R_{\bar{F}} \approx 2$. The final result $T_{\rm K}(U)$ using both transforms is shown in Fig. 4.2 and agrees quantitatively with the reference NRG results.

In this work, singularities were never found near the real positive axis, so that all $U > 0$ can be reached using the conformal transforms of Fig. 4.4, given that enough orders of the series are known. However, one may very well build a conformal transform to reach a regime *beyond* a singularity by considering a *concave* contour $\mathcal{C}$, as it is shown in section 4.3. This may become interesting if a phase transition occurs when interaction is increased.

4.2.3 Noise reduction with Bayesian inference

We now apply the Bayesian inference technique described above to the computation of $T_{\rm K}(U)$. In the left panel of Fig. 4.5 we have re-sampled the series for the Kondo temperature, *i.e.* we have generated many series within error bars given by the QMC calculation (typically 10^3 to 10^5 samples). For each sample we perform the conformal transformation and plot the result for the Kondo temperature as a function of U (thin red lines). While we find that all results agree for $U \leq 6\Gamma$, the bundle of curves start to diverge

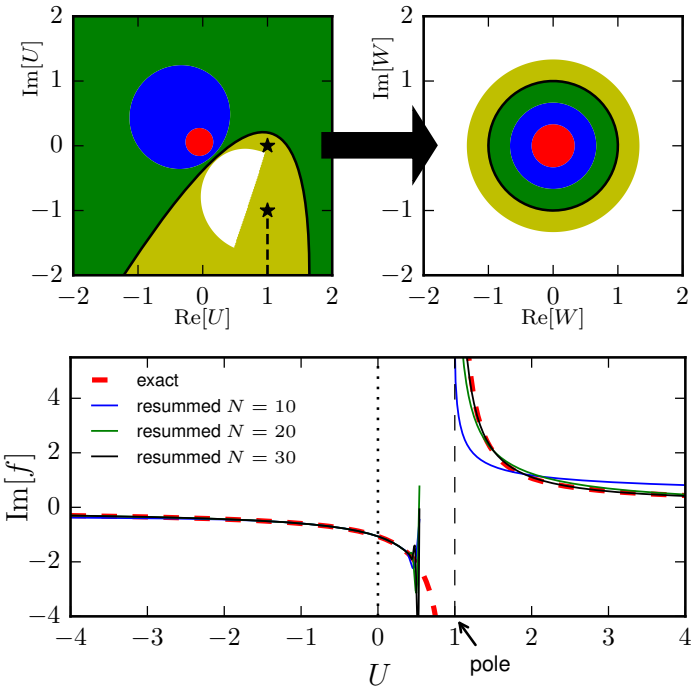

Figure 4.6: Resummation of the series of $f(U) = 1/\ln(i(1-U)+1)$ beyond a pole on the real positive axis. f has a pole at $U = 1$ and a branch cut starting at $U = 1-i$ and going in straight line toward $1-i\infty$ (stars and dashed line in upper left panel). We isolated these singularities by applying a conformal map $W = \frac{\chi(U)-\chi(0)}{\chi(U)-\chi(0)^*}$, with $\chi(U) = i\sqrt{(U-1)/p} - i$. It maps the inside of a parabola into the outside of the unit disk (upper panels). p controls the direction and width of the parabola. Here $p = 0.2e^{i\pi\times 0.4}$. Lower panel: with $N = 30$ terms, one can compute f for all real U (black plain line) except a narrow band around the pole (dashed black vertical line).

for larger values of U. In the middle panel, we plot (black thin line) the corresponding histogram of the values obtained for $T_K(U = \infty)$, which is $P_{\text{prior}}(T_K = g(f))$.

We use the non-perturbative relation $\lim_{U\to\infty} T_K(U) = 0$. Hence we want to "post-select" the configuration of F_n which give a vanishing Kondo temperature at large U, at precision ϵ. Following the procedure described in section 4.1.3, our final result is obtained by averaging the different traces (thin red lines) with the weight given by Eq. 4.3. The right panel of Fig. 4.5 shows the result for three different values of U as a function of ε which confirms that the results are insensitive to the actual value of ε. We find a very good agreement with the results obtained from NRG even at large values of U, noting that NRG spectra have typical relative error bars of a few percents.

4.2.4 Benchmark with the Bethe Ansatz exact solution

The series expansion for $1/T_K(U)$ has been calculated explicitly and exactly using the Bethe Ansatz technique by Horvatić and Zlatić [69]. Ref. [69] provides an iterative formula for calculating the coefficients of the expansions and shows that the corresponding series has an infinite radius of convergence. This provide another independent benchmark

of the calculation of $T_K(U)$ as well as of the method itself. We checked that the 10 first coefficients of this series agree with the one that we computed with QMC.

Fig. 4.2 shows our final result together with the NRG result (black circles) and the Bethe ansatz results. At this scale, the agreement is perfect. Using the exact series for $1/T_K(U)$ (truncated to around 50 coefficients), we studied its zeros which are the poles of $T_K(U)$. We find that they are situated on the imaginary axis. The poles closest to the origin are $U/\Gamma \approx \pm 4.89059579i$ in agreement with our findings (see Fig. 4.3). The next poles are $U/\Gamma \approx \pm 13.79i$, $\pm 21.77i$, $\pm 29.89i$, $\pm 37.87i$ and $\pm 45.9i$ but are too far to be accessible with only the first ten coefficients. The right panel of Fig. 4.5 provides a detailed benchmark of our results versus both NRG and the exact Bethe Ansatz solution.

We find that the QMC results for T_K are slightly more accurate than NRG, because the extraction of T_K from the NRG self-energy (see Eq. 4.4) contains inherent broadening errors. The agreement between all three methods is nevertheless excellent. In addition, we can extract from the Bethe Ansatz the exact QMC error, and this error matches the measured 1 sigma statistical error bars.

4.3 Singularity on the real axis: a toy model

To conclude this chapter, we wish to give a rough idea of the possibilities opened by conformal transforms, given knowledge of the singularities. One limitation of series resummation may happen if a singularity lies on the real positive U axis, *i.e.* for a physical value. This is expected at a phase transition for instance. Using a toy function with this caracteristic, we show in Fig. 4.6 how it can be recovered *beyond the singularity*. Even if the physical validity of such bypass is not clear for a phase transition, this gives an idea of the potential of resummation techniques.

The toy function is $f(U) = 1/\ln(i(1-U)+1)$ and has a pole on the real axis at $U = 1$ as well as a branch cut on the curve $U = 1 - i(1+x)$ with $x \in [0, \infty]$. We use the conformal map $W = \frac{\chi(U)-\chi(0)}{\chi(U)-\chi(0)^*}$, with $\chi(U) = i\sqrt{(U-1)/p} - i$ that maps the inside of a parabola into the outside of the unit disk (see the upper left and right panels of Fig. 4.6). The lower panel of Fig. 4.6 shows the corresponding resummed series using $N = 10, 20$ and 30 terms in the expansion of $f(U)$. Although we cannot calculate close to the singularity $U = 1$, we find that with as little as $N = 20$ terms in the expansion of $f(U)$, we can recover an accurate description of $f(U)$ for $U > 1.2$ from an expansion around $U = 0$.

Chapter 5

Application to the Anderson impurity model

Now that the methodology has been described, we apply it to the two-terminal single orbital Anderson impurity model both at and out-of equilibrium. We observe a strong Kondo effect at equilibrium and its transformation when voltage bias is increased. By computing the kernel of the Green's function, we are able to obtain the density of state, such as shown in the introduction, in a single Monte Carlo run. We reach strong interaction regimes by using the resummation scheme presented in the previous chapter, and we benchmark the results against state-of-the-art NRG calculations. Thus, as will be illustrated at the end of this chapter, we are now in position to study the interplay between strong interactions and non-equilibrium physics through full spectrum, distribution functions, or other frequency-dependent quantities.

5.1 Description of the model

The Hamiltonian of the two-terminal single orbital Anderson impurity model under study is:

$$\mathbf{H} = \sum_{i=-\infty}^{+\infty} \sum_{\sigma} \gamma_i \mathbf{c}_{i,\sigma}^{\dagger} \mathbf{c}_{i+1,\sigma} + h.c. + \epsilon_d(\mathbf{n}_{\uparrow} + \mathbf{n}_{\downarrow}) + U\theta(t)\left(\mathbf{n}_{\uparrow} - \frac{1}{2}\right)\left(\mathbf{n}_{\downarrow} - \frac{1}{2}\right) \tag{5.1}$$

It connects an impurity on site 0 to two semi-infinite electrodes $i < 0$ and $i > 0$. The impurity corresponds to a single level artificial atom as sketched in Fig. 5.1. Here ϵ_d is the on-site energy of the impurity (relative to the particle-hole symmetric point), $\mathbf{n}_{\sigma} = \mathbf{c}_{0,\sigma}^{\dagger}\mathbf{c}_{0,\sigma}$ is the impurity density of spin σ electrons. $\mathbf{c}_{i,\sigma}^{\dagger}$ and $\mathbf{c}_{i,\sigma}$ are the creation and annihilation operators for electrons on site i with spin σ. In this chapter we use $\hbar = e = 1$. $\theta(t)$ is the Heaviside function: we switch the interaction on at time $t = 0$, as it is required in the Keldysh formalism (see section 2.1.1). Calculations have been performed for large times so that the system has relaxed to its stationary regime. The hopping parameters are given by $\gamma_i = 1$ except for $\gamma_0 = \gamma_{-1} = \gamma$ which connect the impurity to the electrodes. The calculations can be performed for arbitrary values of γ. However, since we are not interested in the large energy physics of the electrodes, we suppose that $\gamma \ll 1$, *i.e.* that the tunneling rate from the impurity to the electrodes is energy independent $\Gamma = 2\pi\gamma^2\rho_{\mathrm{F}}$ where ρ_{F} is the density of states of the electron reservoirs at the Fermi level. As we are in the infinite bandwidth limit, there are no bound state in the non-interacting

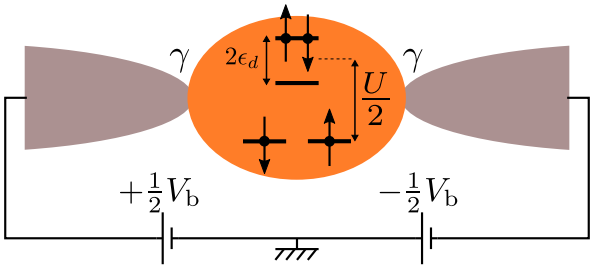

Figure 5.1: The two-terminal Anderson impurity model describing a single level quantum dot. The level with energy ϵ_d is subject to a finite Coulomb interaction U, and is hybridized with a tunnel coupling γ to two leads that are biased with voltage V_b.

problem [128], so our QMC algorithm can be applied safely. The two electrodes have a chemical potential symmetric with respect to zero $\pm V_\mathrm{b}/2$ which corresponds to a voltage bias V_b. They share the same temperature that we take very low $k_\mathrm{B}T = 10^{-4}\Gamma$.

Solution of the non-interacting model

The non-interacting retarded Green's function of the impurity is given by:

$$g^R_{\sigma\sigma'}(\omega) = \frac{\delta_{\sigma\sigma'}}{\omega + i\eta - \epsilon_d - \Sigma_\mathrm{L} - \Sigma_\mathrm{R}} \tag{5.2}$$

for spins σ and σ'. $\Sigma_\mathrm{X} = -i\Gamma/2$ is the hybridization of the lead X to the dot. We will only consider $\sigma = \sigma' = \uparrow$ for simplicity and omit them in further notation. Hence:

$$g^R(\omega) = \frac{1}{\omega - \epsilon_d + i\Gamma} \tag{5.3}$$

This contains all information about the equilibrium one-body problem. In particular, the density of state on the dot $-\operatorname{Im} g^R(\omega)/\pi$ is a Lorentzian of width Γ centered on ϵ_d. Γ is the important energy scale in the non-interacting model.

Out of equilibrium, a complete description of the one-body physics require two additional green's functions $g^<$ and $g^>$ (in fact, only these are required, as g^R can be deduced from them). Within the standard non-equilibrium Keldysh formalism [161], they are given by:

$$g^<(\omega) = \frac{i\Gamma\left[n_F\left(\omega + \frac{V_\mathrm{b}}{2}\right) + n_F\left(\omega - \frac{V_\mathrm{b}}{2}\right)\right]}{(\omega - \epsilon_d)^2 + \Gamma^2} \tag{5.4}$$

$$g^>(\omega) = \frac{i\Gamma\left[n_F\left(\omega + \frac{V_\mathrm{b}}{2}\right) + n_F\left(\omega - \frac{V_\mathrm{b}}{2}\right) - 2\right]}{(\omega - \epsilon_d)^2 + \Gamma^2} \tag{5.5}$$

where $n_F(\omega) = 1/(e^{\omega/k_\mathrm{B}T} + 1)$ is the Fermi function. $g^>(\omega)$ and $g^<(\omega)$ are the starting point for the expansion in power of U that was performed with the real-time diagrammatic quantum Monte Carlo algorithm described in chapter 3.

Definition of the quantities of interest

The quantities of interest are the impurity interacting Green's functions for spin up electrons:

$$G^R(t,t') = -i\theta(t-t')\left\langle\left\{\mathbf{c}_{0\uparrow}(t), \mathbf{c}^\dagger_{0\uparrow}(t')\right\}\right\rangle \tag{5.6a}$$

$$G^<(t,t') = i\left\langle\mathbf{c}^\dagger_{0\uparrow}(t')\mathbf{c}_{0\uparrow}(t)\right\rangle \tag{5.6b}$$

$$G^>(t,t') = -i\left\langle\mathbf{c}_{0\uparrow}(t)\mathbf{c}^\dagger_{0\uparrow}(t')\right\rangle \tag{5.6c}$$

where the operators have been written in Heisenberg representation. Since we will restrict ourselves to the stationary limit, these functions depend on $t-t'$ only and can be studied in the frequency domain. Of particular interest is the spectral function (or interacting local density of state) given by:

$$A(\omega) = -\frac{1}{\pi}\operatorname{Im}[G^R(\omega)] \tag{5.7}$$

The out-of-equilibrium spectral function can be used for the computation of the current–voltage characteristic using the Wingreen–Meir formula [102]:

$$I = \frac{\Gamma}{2}\int A(\omega)\left[n_F\left(\omega+\frac{V_\mathrm{b}}{2}\right) - n_F\left(\omega-\frac{V_\mathrm{b}}{2}\right)\right]\mathrm{d}\omega \tag{5.8}$$

The retarded self-energy $\Sigma^R(\omega)$ is defined from the interacting Green's function by:

$$G^R(\omega) = \frac{1}{\omega - \epsilon_d + i\Gamma - \Sigma^R(\omega)} \tag{5.9}$$

Physical quantities have systematic expansion in powers of U:

$$G^R(t-t') = \sum_{n=0}^{+\infty} G^R_n(t-t')U^n \tag{5.10}$$

from which we obtain the corresponding quantity in the frequency domain by Fourier transform:

$$G^R(\omega) = \sum_{n=0}^{+\infty} G^R_n(\omega)U^n \tag{5.11}$$

We obtain the functions $G^R_n(\omega)$ using the QMC algorithm of chapter 3. The expansion of the self-energy:

$$\Sigma^R(\omega) = \sum_{n=0}^{+\infty} \Sigma^R_n(\omega)U^n \tag{5.12}$$

is obtained from the $G^R_n(\omega)$ using a formal series expansion order by order of the Dyson equation 5.9:

$$\Sigma^R_n(\omega) = [g^R(\omega)]^{-2}G^R_n(\omega) - \sum_{k=1}^{n-1}\Sigma^R_k(\omega)G^R_{n-k}(\omega)g^R(\omega)^{-1} \tag{5.13}$$

for $n > 1$ with $\Sigma^R_1(\omega) = [g^R(\omega)]^{-2}G^R_1(\omega)$.

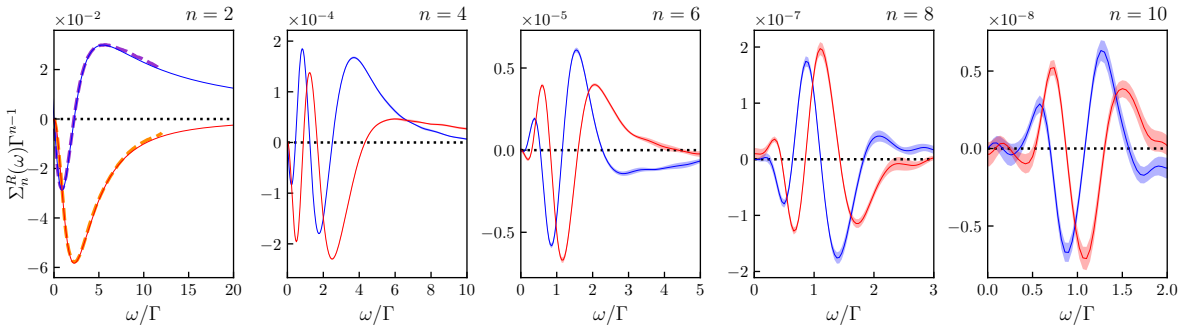

Figure 5.2: First terms $\Sigma_n^R(\omega)$ of the expansion of the retarded self-energy in the particle-hole symmetric case ($\epsilon_d = 0$) for $n = 2, 4, 6, 8$ and 10. (plain lines, real part in blue and imaginary part in red). This curves are obtained in a single Monte Carlo run. Error bars are shown as shaded areas. A previous result at order two from Yamada [183] is shown in dashed lines. Note the decreasing scale with n. Maximum integration time is $t_M = 20/\Gamma$.

5.2 The impurity in equilibrium

At equilibrium, we expect to observe the Kondo resonance in the spectral function getting increasingly thinner as U is increased. We show the application of our QMC algorithm, the results in the perturbative regime following a bare sum of the series, and how the resummation procedure is applied to reach the strong interaction regime.

5.2.1 Monte Carlo results: perturbation series order by order

Data obtained by QMC for the K kernel in the symmetric model ($\epsilon_d = 0$) and the Green's function derived from it have already been shown in section 3.3.1 (Fig. 3.2 page 56). Due to particle-hole symmetry, odd orders are zero and are not shown. However, they are globally less accurate than those obtained with the L kernel, as has been discussed in section 3.3.2. As a result we show hereafter only data obtained with the L kernel.

We compute the self-energy from the Green's function using the recursive formula 5.13. The coefficients of the self-energy in the symmetric model are shown in Fig. 5.2 where we plot $\Sigma_n^R(\omega)$ for $n = 2, 4, 6, 8$ and 10. The error bars increases with the order n which we attribute to the fact that, since the self-energy only contains one-particle irreducible diagrams — diagrams which cannot be split into two by cutting one edge — it is subject to many cancellations of terms. Indeed, one finds that the decay of $\Sigma_n^R(\omega)$ with n is rather rapid with seven orders of magnitude between the first and the tenth order.

Our first benchmark uses a reference perturbative calculation made by Yamada [183] and Bethe ansatz results from Horvatić & Zlatić [69]. The result at order 2 is compared with the result of Yamada in the left panel of Fig. 5.2 and found to be in excellent agreement. In his seminal work Yamada also provided analytical calculations at order 2 and 4 in the form of a low frequency expansion for the particle-hole symmetric impurity:

$$\Sigma^R(U,\omega) = \Gamma \sum_{n,m} i^{m+1} s_{n,m} \left(\frac{\omega}{\Gamma}\right)^m \left(\frac{U}{\Gamma}\right)^n \tag{5.14}$$

	$m=0$	$m=1$	$m=2$	$m=3$	$m=4$
$n=2$ (Q)	$0 \pm 1\times10^{-5}$	$5.39(4)\times10^{-2}$	$5.03(6)\times10^{-2}$	$3.67(5)\times10^{-2}$	$2.17(2)\times10^{-2}$
$n=2$ (Y)	0	5.3964×10^{-2}	5.0660×10^{-2}		
$n=2$ (B)	0	5.3964×10^{-2}			
$n=4$ (Q)	$0 \pm 2\times10^{-6}$	$5.7(0)\times10^{-4}$	$1.9(9)\times10^{-3}$	$4.3(4)\times10^{-3}$	$6.2(4)\times10^{-3}$
$n=4$ (Y)	0	5.6771×10^{-4}	2.0079×10^{-3}		
$n=4$ (B)	0	5.6482×10^{-4}			
$n=6$ (Q)	$0 \pm 1\times10^{-7}$	$2.(1)\times10^{-6}$	$3.(1)\times10^{-5}$	$1.(5)\times10^{-4}$	$4.7(1)\times10^{-4}$
$n=6$ (B)	0	2.5119×10^{-6}			

Table 5.1: First coefficients $s_{n,m}$ (real) of the self-energy Taylor series $\Sigma(U,\omega)/\Gamma = \sum_{n,m} i^{m+1} s_{n,m} (U/\Gamma)^n (\omega/\Gamma)^m$ on the equilibrium symmetric model $\epsilon_d = 0$. Coefficients in powers of ω have been obtained by fitting the bare data by a polynomial. We find a good agreement between our QMC results (Q), analytical calculations from Yamada [183] (Y), and Bethe ansatz exact calculations from Horvatić & Zlatić [69] (B). The figure in parentheses is uncertain.

Table 5.1 shows the results of Yamada ($m = 1, 2$ and $n = 2, 4$, (Y) rows) as well as ours (obtained by fitting our numerical data at low frequency, (Q) rows). We also compare to exact results using a Bethe ansatz from Ref. [69] for the linear term in frequency ((B) rows). We find a good quantitative agreement with Yamada results and the Bethe ansatz. Yamada also provided numerical results at $n = 4$ which are almost featureless and in very poor agreement with our data.

5.2.2 Density of state from bare series summation

Once the Green's function or self-energy has been obtained up to a certain order, the last task is to extract the physical information from this expansion. The most naive approach is to compute the truncated series up to a certain maximum order N:

$$\Sigma^R(U,\omega) \approx \sum_{n=1}^{N} \Sigma_n^R(\omega) U^n \tag{5.15}$$

We find that the self-energy series has a convergence radius $U_c \approx 6\Gamma$ at the particle symmetry point $\epsilon_d = 0$ while this convergence radius decreases down to $U_c \approx 4\Gamma$ in the asymmetric case $\epsilon_d = \Gamma$. These convergence radii fix the maximum strength of U that one can study using the naive truncated series approach.

The data for the self-energy and corresponding spectral functions are shown in Fig. 5.3 for the symmetric case (left panels, $\epsilon_d = 0$ and $U = 5\Gamma$) and asymmetric case (right panels, $\epsilon_d = \Gamma$ and $U = 3\Gamma$). For these values of interaction, the error in our calculation is dominated by the finite truncation of the series (negligible error due to the statistical Monte Carlo sampling) and is of the order of the line width. Fig. 5.3 also shows the NRG results that we use to benchmark our calculations and that are in excellent agreement with our data. Note that in order to obtain this agreement, the precision of the NRG calculations had to be pushed much further than what is typically done in the field, indicating that the QMC method is very competitive, in particular at large frequencies.

Qualitatively, the strength of interaction that could be reached using the truncated series corresponds to the onset of the Kondo effect: one observes in the upper left panel

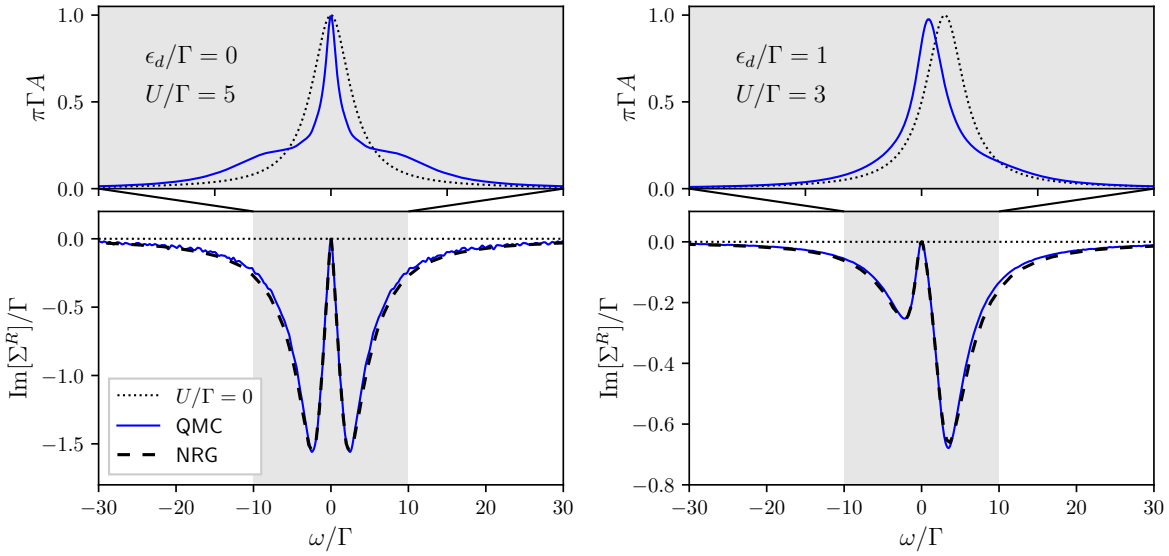

Figure 5.3: Sum of the truncated series for the self-energy $\Sigma^R(\omega)$ at $\epsilon_d = 0$ and $U = 5\Gamma$ (lower left panel) and $\epsilon_d = \Gamma$ and $U = 3\Gamma$ (lower right panel) up to $N = 10$ orders in perturbation theory. The upper panels show the corresponding spectral function. The Monte Carlo results (blue plain lines) are consistent with non-perturbative NRG calculations (dashed lines). The non-interacting situation is shown as dotted lines. Maximum integration time is $t_{\mathrm{M}} = 20/\Gamma$.

of Fig. 5.3 that the Kondo peak starts to form around $\omega = 0$, its width is significantly narrower than without interaction and the premisses of the side peaks at $\pm U/2$ can be seen. In order to observe well established Kondo physics, one must therefore go beyond the convergence radius wall. This is in fact rather natural, the convergence radius corresponds to poles or singularities in the complex U plane which themselves correspond to the characteristic energy scales of the system. Getting past this "convergence radius wall" is therefore crucial.

Details of the NRG implementation

Important details of the NRG implementation which was used to benchmark our QMC calculations, which was realised by Serge Florens, are presented in this short section. As is seen along this chapter, NRG was used both to benchmark the bare QMC results at weak U and to test the reliability of the series resummation method for reaching strong U, in the equilibrium Anderson impurity model for various ϵ_d. In order to obtain precise NRG data for the spectral function of the Anderson impurity model, the computations were performed using several improvements over the simplest implementations of the NRG.

First, the full density matrix formulation of NRG [67] was used to reduce finite size effects due to the NRG truncation. Second, symmetries of the problem were heavily exploited [164], allowing to reduce significantly the Hilbert space dimension of various multiplets. In the particle-hole symmetric case, the full $\mathrm{SU}(2)_{\mathrm{charge}} \otimes \mathrm{SU}(2)_{\mathrm{spin}}$ symmetry was used, while the charge sector was reduced to $\mathrm{U}(1)_{\mathrm{charge}}$ away from particle-hole symmetry. Third, the impurity Green's function was extracted from a direct computation

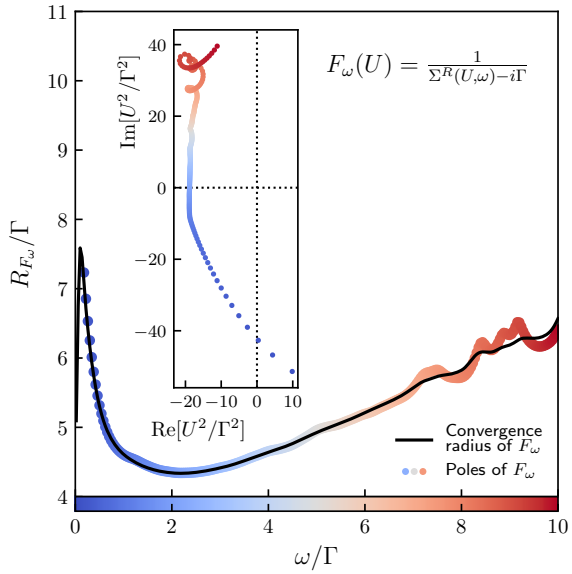

Figure 5.4: Main frame: convergence radius R_{F_ω} of $F_\omega(U) = 1/(\Sigma^R(U,\omega) - i\Gamma)$ (thin line) in the equilibrium symmetric Anderson impurity model. The color circles show the absolute value of the pole of $F_\omega(U)$. Inset: position of the pole of $F_\omega(U)$ in the U^2 complex plane for different frequencies. The color blue to red corresponds to increasing frequency, as in the main frame. At high frequency, the statistical uncertainty prevents an accurate localization of the poles.

of the d-level self-energy $\Sigma^R(\omega)$ [18], according to its exact representation as the ratio of two retarded correlation functions in the frequency domain:

$$\Sigma^R(\omega) = U\frac{F^R(\omega)}{G^R(\omega)} \tag{5.16}$$

where $G^R(t) = -i\theta(t)\,\langle\{\mathbf{c}_{0\uparrow}(t), \mathbf{c}^\dagger_{0\uparrow}(0)\}\rangle$ is the usual single particle retarded Green's function in the time domain, and:

$$F^R(t) = -i\theta(t)\,\langle\{\mathbf{c}_{0\uparrow}(0)\mathbf{c}^\dagger_{0\downarrow}(0)\mathbf{c}_{0\downarrow}(0), \mathbf{c}^\dagger_{0\uparrow}(t)\}\rangle \tag{5.17}$$

is a composite fermionic correlation function. In practice, $\mathrm{Im}[G^R(\omega)]$ and $\mathrm{Im}[F^R(\omega)]$ are computed from the Källén–Lehmann representation using the broadened NRG spectra, and the real parts of both $G^R(\omega)$ and $F^R(\omega)$ are obtained via a Kramers–Kronig relation.

Finally, the truncation parameters of the NRG simulations were taken to model as closely as possible a continuous density of states for the electronic bath. Although the use of the logarithmic Wilson discretization grid, $\omega_n = D\Lambda^{-n}$, is inherent to the practical success of NRG, we found that values of Λ as low $\Lambda = 1.4$ could be managed in practice within the NRG, taking a very large number $N_{\mathrm{kept}} = 3200$ of kept multiplets. Up to $N_{\mathrm{iter}} = 120$ NRG iterations were used, so that the effective temperature can be considered to be practically zero. With such small value of Λ, the broadening parameter b of the discrete NRG spectra could be decreased down to $b = 0.2$, without z-averaging, which further enhanced the spectral resolution of the Hubbard satellites in the spectral function.

5.2.3 Density of state in the strong interaction regime

In order to reach stronger interaction regime, we apply the resummation technique discussed in chapter 4 to the full Green's function $G^R(\omega, U)$ and self-energy $\Sigma^R(\omega, U)$. First, we observe that the convergence radius of G^R and Σ^R depends on frequency ω, so it is caused by a singularity in the U complex plane which is moving with ω. It is therefore necessary to apply the resummation technique distinctly for each frequency.

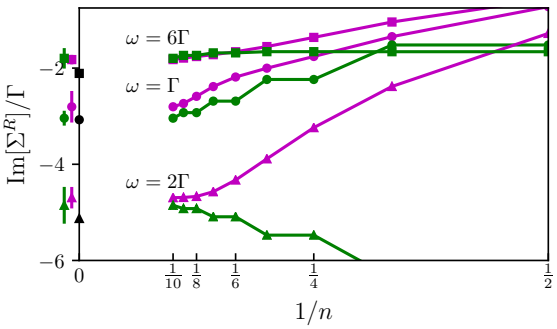

Figure 5.5: Resummation of the self-energy in the equilibrium symmetric Anderson impurity model at $U = 9\Gamma$. The imaginary part of $\Sigma^R(\omega)$ is shown as a function of the number n of terms kept in the resummation, for three frequencies $\omega = \Gamma$ (circles), 2Γ (triangles) and 6Γ (squares). The independent resummation of $F_\omega(U)$ (green line) and of $\Sigma^R(\omega) - i\Gamma$ (purple line) converge with one another. The results with truncation and statistical errors are shown on the left of the y-axis, along with NRG results (black symbols).

Frequency-dependent resummation of Green's functions

We focus on the quantity $\Sigma^R(\omega) - i\Gamma$ and denote its inverse $F_\omega(U) = 1/(\Sigma^R(\omega) - i\Gamma)$. The retarded Green's function can be recovered from $F_\omega(U)$ using $G^R(\omega) = 1/(\omega - F_\omega(U)^{-1})$ (using $\omega - \Sigma^R(\omega) + i\Gamma$ turns out to be less convenient especially at high frequency). Fig. 5.4 shows the convergence radius of $F_\omega(U)$ as a function of frequency, extracted from a study of the exponential decay of the corresponding series with n. We have also performed a systematic study of the zeros of $\Sigma^R(\omega) - i\Gamma$ in order to localize the poles of $F_\omega(U)$. We find one pair of poles at each frequency. The results are shown in the inset of Fig. 5.4 for a set of frequencies from $\omega = 0$ to $\omega = 10\Gamma$ in the complex plane for U^2. The absolute value of the poles of $F_\omega(U)$ is also plotted in the main frame of Fig. 5.4 as a function of frequency (circles of varying colors from blue to red). We observe a perfect match with our estimation of the convergence radius reflecting the fact that these poles are responsible for the divergence of the series. It is important to note here that working in the real frequency domain is very helpful: we found a single pole per frequency (at least for the range of interactions that we could study). Hence, we expect that performing the resummation in real time or imaginary frequencies could be more complex, since all these poles would be involved simultaneously.

The results after conformal transform for three frequencies ($\omega/\Gamma = 1, 2$ and 6) are given in Fig. 5.5. We show the convergence of the imaginary part of the self-energy using two different resummed series: $F_\omega(U)$ (green symbols) and $1/F_\omega(U)$ (purple symbols). The former has been resummed with an Euler transform with a frequency dependant p set close to the poles shown in Fig. 5.4. The latter, for which our method did not detect poles, has been resummed with the parabola transform (in the U plane) with $p = -4.5\Gamma$. Again, Bayesian inference has been used to enforce $\lim_{U\to\infty} G(U, \omega) = 0$ for all $\omega \neq 0$. For comparison, we also include the NRG results (which are very accurate at small frequency and possibly less accurate at large frequency). The slight difference between the purple and green curves is due to the truncation error. We find that the series which has (initially) the largest convergence radius is less sensitive to truncation error or

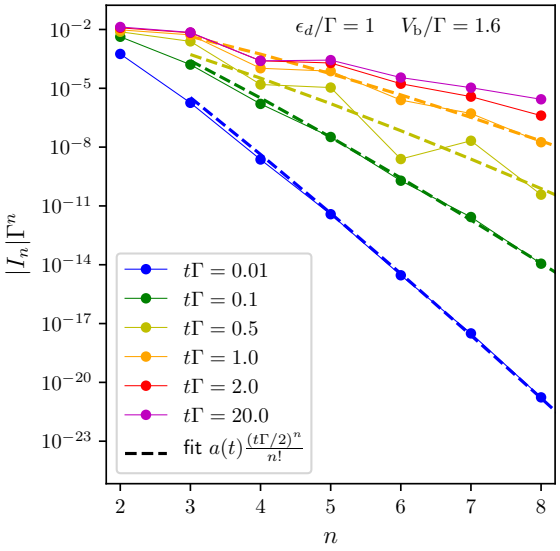

Figure 5.6: Coefficients (absolute value) of the series for the current (circles with plain lines) in the asymmetric model ($\epsilon_d = \Gamma$, $V_b = 1.6\Gamma$) computed at different times t (different colors). The apparent convergence radius decreases with time. For small values of t, we can observe that the series coefficients decrease faster than exponentially, which indicates an infinite convergence radius. The thick dashed line shows the corresponding fit with $(t\Gamma/2)^n/n!$. For large enough t, the series converges toward the steady state limit.

statistical noise than the other. We attribute the small discrepancy between the QMC results and NRG at large frequency to a lack of convergence of the latter. These results are obtained for a rather strong interaction $U = 9\Gamma$. At smaller interaction the QMC and NRG results become undistinguishable. At larger interactions, the QMC results become increasingly inaccurate due to truncation errors.

Note on the long time limit *versus* high order limit

Before presenting the main results, we wish to note an important point concerning the long time limit. In the Keldysh formalism, interactions are switched on at an initial time, and we assume here that the system relaxes to a steady state at long time. Let us consider the average of an operator $\mathbf{O}$ as a function of time, and its expansion $\langle \mathbf{O}(t) \rangle = \sum_n O_n(t) U^n$ (the extension of the following arguments to Green's function is straightforward).

At finite time t, the radius of convergence of this series is infinite, as shown in appendix E. Each order in the perturbation expansion $O_n(t)$ relaxes with t to a long time limit, but the time $t_{\text{relax}}(n)$ it takes to reach this limit can increase with n. The long time and large n limit do not commute in general:

$$\lim_{n\to\infty} \lim_{t\to\infty} O_n(t) \neq \lim_{t\to\infty} \lim_{n\to\infty} O_n(t) \tag{5.18}$$

This behaviour was already noted in Fig. 14 of Ref. [128]. It is also illustrated on Fig. 5.6, which shows various orders n of the expansion of the current through the dot versus n, for different times. We observe that at small times the orders I_n decreases faster than exponentially with n, consistent with the bound mentioned above. The coefficients converge to the steady state limit at long time.

At finite time t, since the series converges, it is sufficient to have enough orders. In the steady state, as explained above, we have a minimal order N_0 needed to compute the quantity at a given precision. One should then simply compute at a time $t > t_{\text{relax}}(N_0)$.

In the Anderson model, some quantities like the spectral function are known to relax on a long time scale $t_K \sim T_K^{-1}$, see *e.g.* Ref. [118]. The previous remarks explain how

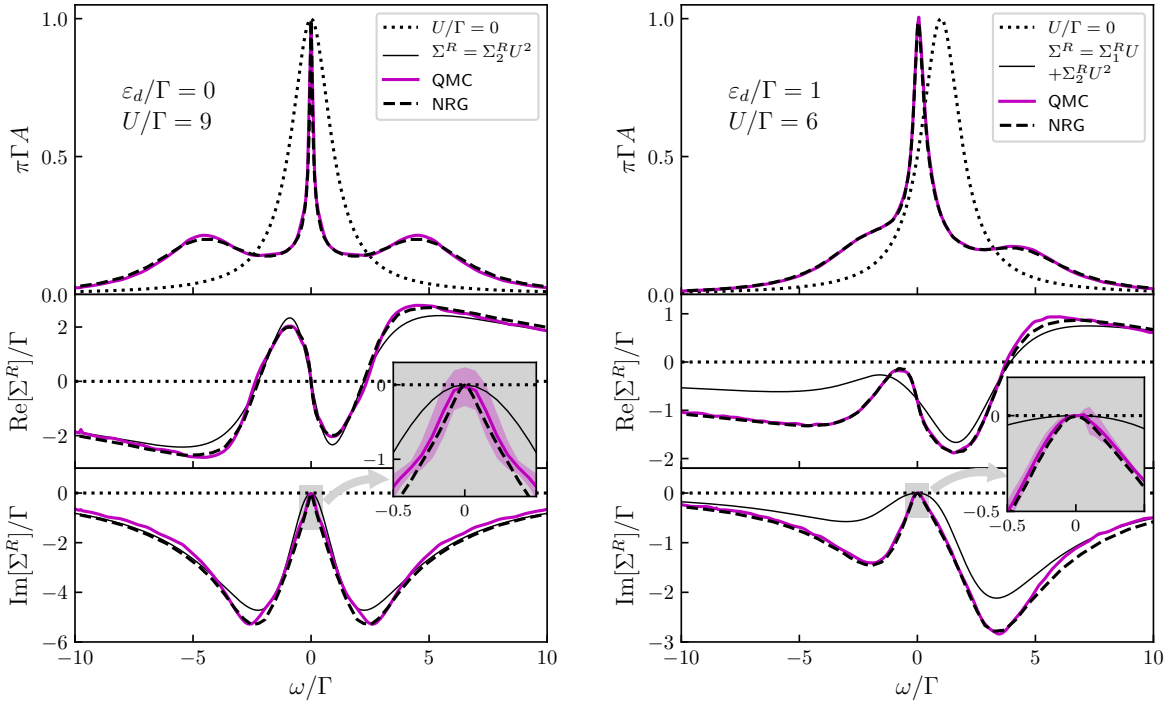

Figure 5.7: Resummed equilibrium spectral function (upper panels), real part (middle panels) and imaginary part (lower panels) of the retarded self-energy $\Sigma^R(\omega)$ for the Anderson impurity. Left column is for the symmetric model $\epsilon_d/\Gamma = 0$ at $U = 9\Gamma$. Right column for the asymmetric model $\epsilon_d/\Gamma = 1$ at $U = 6\Gamma$. Purple line: resummed result from 10 orders of perturbation theory; dashed line: NRG; dotted line: non-interacting result; thin black line: second order perturbation theory for the self-energy. Inset: zoom of the imaginary part at small energy with error bars.

the algorithm deals with this long time. For a given U, we need $N_0(U)$ orders, hence to compute at a time larger than $t_{\mathrm{relax}}(N_0(U))$. The larger U is, the longer this time becomes. However, it is still finite at fixed U, and since the computation effort to get the perturbative expansion do not grow with time, this is not an issue. However, the existence of the Kondo time indicates that the number of orders necessary to compute *e.g.* the low frequency spectral function at a given U increases with U (otherwise the relaxation time of the physical quantity would be bounded at large U).

Formation of the Kondo peak

The left column of Fig. 5.7 shows the spectral function as well as the imaginary and real part of the self-energy for the symmetric Anderson impurity in the strong correlation regime $U = 9\Gamma$ (same data as the purple curve of Fig. 5.5). The spectral function shows a clear Kondo peak and the two satellites at $\omega \simeq \pm 4.5\Gamma = \pm U/2$ in good agreement with the NRG data. For this calculation, a simple second order calculation of the self-energy already provides a reasonably good result (thin black line), due to near cancellations in higher order diagrams in the peculiar case of particle-hole symmetry.

The right column of Fig. 5.7 shows the same plot in the asymmetric case $\epsilon_d = 1$ at $U = 6\Gamma$. This case is more complex because the resonance at $U = 0$ is offset with respect

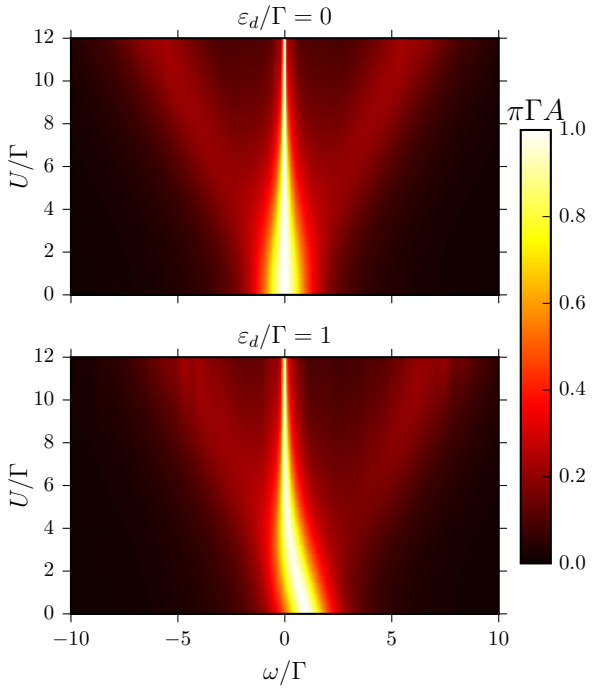

Figure 5.8: Color plot of the spectral density $A(\omega, U)$ in the symmetric case ($\epsilon_d/\Gamma = 0$, upper panel) and asymmetric case ($\epsilon_d/\Gamma = 1$, lower panel) as a function of ω and U. The data from each panel has been obtained in a single QMC run.

to the Fermi level, hence to the position of the Kondo peak. We note that previous real time QMC techniques suffered from a strong sign problem and could not access the asymmetric regime [174]. We also stress that the second order approximation is now very different from the correct result. The comparison to the NRG data is still excellent.

An advantage of the techniques described in this thesis is that a single QMC run provides the full dependence in both ω and U, which is very time consuming in NRG. This is illustrated in Fig. 5.8 where the color map shows the spectral function as a function of ω and U. One can clearly observe the formation of the Kondo peak (which gets thinner as one increases U and shifts toward $\omega = 0$ in the asymmetric case) as well as the Hubbard bands at $\omega = \pm U/2$. Note that the results are perfectly well behaved (qualitatively correct) up to very large U (even above $U = 12\Gamma$ shown in the plot) but become quantitatively inaccurate at too large values of U. Improving them would require the use of higher perturbation orders.

5.3 The impurity under a voltage bias

We finally turn to the out-of-equilibrium regime, and present some accurate computation of current-voltage characteristics, as well as novel predictions for dynamical observables in presence of a finite voltage bias.

5.3.1 Splitting of the Kondo peak

The left panel of Fig. 5.9 shows the spectral function of the symmetric impurity in the presence of various voltage differences from $V_\mathrm{b} = 0$ to 4Γ. The results were obtained using the parabolic map on the series in U^2 of $\Sigma^R(\omega, U^2) - i\Gamma$ (with an optimized frequency dependent parameter $p/\Gamma^2 \in [-25, -200]$). Upon increasing the bias voltage, we find as expected from NCA [182] and perturbative [38] calculations that the Kondo resonance

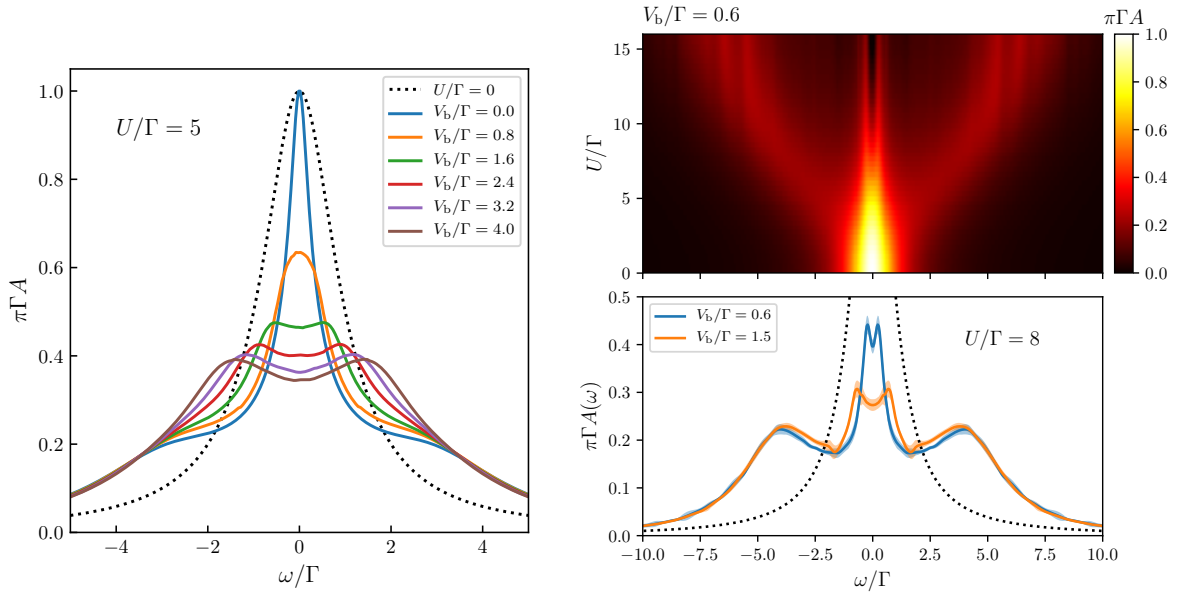

Figure 5.9: Splitting of the Kondo peak in the symmetric ($\epsilon_d/\Gamma = 0$) model under a symmetric voltage bias V_b. Left panel: Out-of-equilibrium spectral functions with interaction strength $U/\Gamma = 5$, at zero temperature, for different V_b. Lower right panel: Out-of-equilibrium spectral functions with interaction strength $U/\Gamma = 8$, at temperature $T = \Gamma/50$, for two bias $V_b = 0.6\Gamma$ (blue line) and $V_b = 1.5\Gamma$ (orange line). Error bars are shown as shaded areas. The dotted line shows the non-interacting density. The self-energy series has been resummed in a similar fashion as for the previous results. Upper right panel: color plot of the spectral density as a function of ω and U for $V_b = 0.6\Gamma$. No Bayesian inference has been used. Integration time is $20/\Gamma$.

simultaneously broadens and get split into two peaks. Previous results on the spectral function [24] were based on the bold diagrammatic approach and were calculated at relatively high temperature ($k_B T = \Gamma/3$) while using a third terminal for computing the spectral function.

Most of the results presented in this chapter have been obtained at very low temperature. We emphasize however that increasing the temperature makes the calculations easier: indeed at finite temperature, the non-interacting Green's functions decrease exponentially as $e^{-\pi k_B T t}$ instead of the algebraic decay at zero temperature. It follows that the support of the integrals to be calculated is smaller, hence the convergence of the calculation is faster. We show a calculation at finite temperature in the right column of Fig. 5.9 where we have computed the spectral density of the symmetric impurity at temperature $T = \Gamma/50$ under a voltage bias $V_b = 0.6\Gamma$ and $V_b = 1.5\Gamma$. A single Monte Carlo run allows to observe the splitting of the Kondo resonance as U is increased (upper panel). The result is quantitatively accurate up to $U \approx 8\Gamma$ (lower panel) but remains qualitatively meaningful at higher interaction (upper panel).

The fate of the Kondo resonance out-of-equilibrium, in presence of a voltage bias, can be understood qualitatively from the interplay of two phenomena. On the one hand, the voltage bias induces a splitting of the Fermi energies of the two reservoirs, hence one expects a corresponding splitting of the Kondo resonance. On the other hand, the

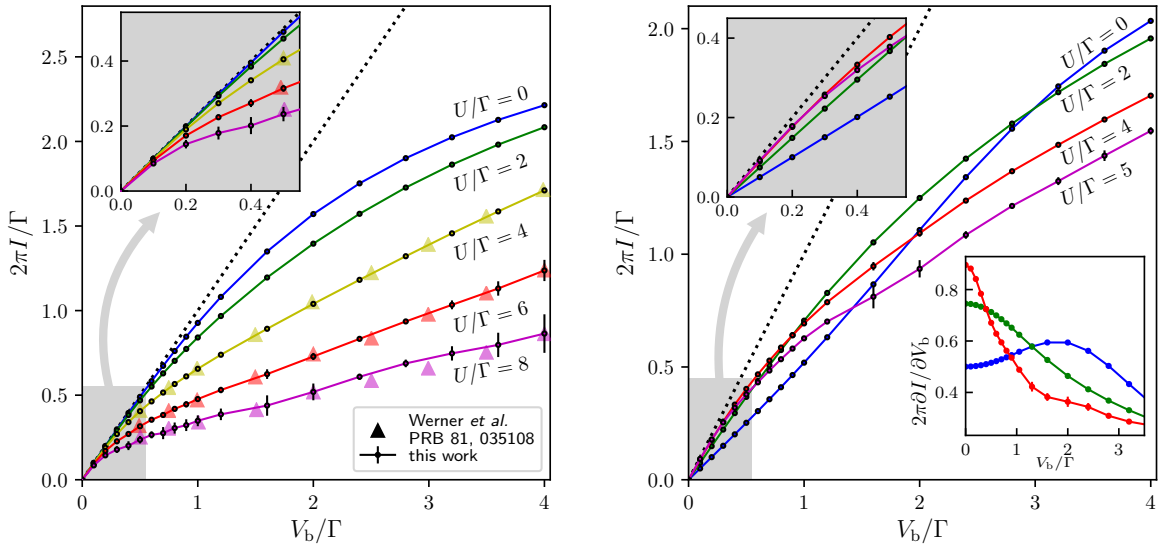

Figure 5.10: Left panel: current-voltage characteristics at different interaction strengths in the symmetric case $\epsilon_d = 0$. Perturbation series for the current have been computed using the Landauer formula Eq. 5.8, then resummed. The results are consistent with a weak-coupling Quantum Monte Carlo calculation from Werner *et al.* [174] (triangles), but extends further down in bias. Right panel: Current-voltage characteristics at different interaction strengths in the asymmetric model ($\epsilon_d/\Gamma = 1$). The bottom-right inset shows the development of the zero-bias anomaly in the differential conductance when U increases ($U/\Gamma = 0$ in blue, 2 in green and 4 in red).

voltage, like the temperature, increases the energy and phase space for the spin fluctuations, leading eventually to the disappearance of the Kondo resonance [4, 61, 62]. The competition between both effects leads to the appearance of the splitting only above a finite voltage threshold (about $V_b \simeq \Gamma$ in the left panel of Fig. 5.9).

5.3.2 Application to transport: I–V characteristics

From the out-of-equilibrium density of state one can compute the series for the current through the impurity from Eq. 5.8. The left panel in Fig. 5.10 shows the results obtained for the I–V characteristics in the symmetric case $\epsilon_d = 0$. The resummation has been done for the series of $1/I(U^2)$ using a parabolic transform with $p = -40\Gamma^2$. At small bias, we recover a perfect transmission $I = (e^2/h)V_b$ due to the unitary Kondo resonance, while for $eV_b > k_B T_K$ the conductance experiences an extra suppression by the interaction (Coulomb blockade). We find a very good match with a previous calculation from Ref. [174]. The present technique allows one to lift the main limitations that Ref. [174, 175] was facing: we can now access long times (here we have used $t_M \sim 20/\Gamma$ but it could be increased further if necessary) to be compared with maximum times of the order of $\sim 3/\Gamma$ to $5/\Gamma$ in Ref. [174]. As a consequence, we can reach the low bias regime, which was not accessible in Ref. [174]. Another important point is that the method is not limited to the symmetry point as we now demonstrate.

The right panel in Fig. 5.10 shows the I–V characteristics for an *asymmetric* model

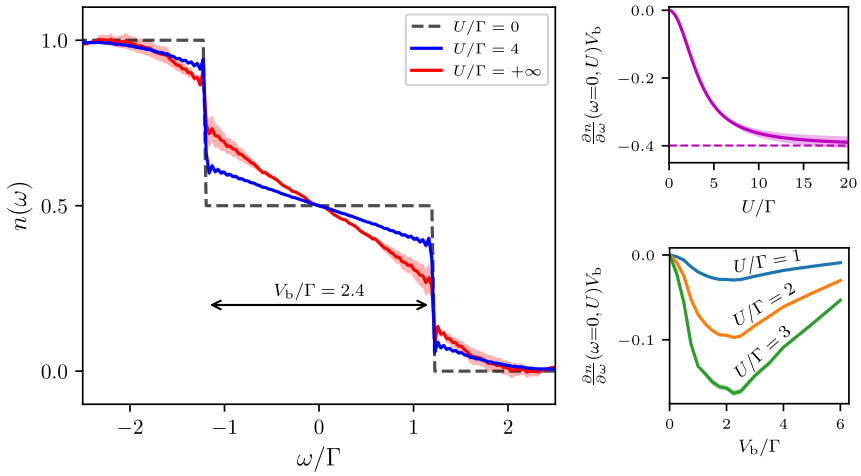

Figure 5.11: Left panel: out-of-equilibrium electron distribution function on the impurity ($\epsilon_d/\Gamma = 0$) under a voltage bias $V_b = 2.4\Gamma$. The distribution function is defined as in Eq. 5.19. Increasing the interaction strength ($U/\Gamma = 4$ blue line, $U/\Gamma = +\infty$ red line) leads to a softening of the characteristic double-step of the non-interacting distribution function (dashed line). It is linear between the Fermi levels of the two leads. The Euler transform has been used for resummation and the result has not been submitted to Bayesian inference. Right panels: normalized slope of the distribution function near $\omega = 0$ as a function of V_b (bottom panel) and U (top panel, for $V_b = 2.4\Gamma$). For intermediate interaction, the normalized slope reaches an extremum near $V_b = 2\Gamma$. At strong interaction, the normalized slope saturates.

with $\epsilon_d/\Gamma = 1$. The results have been obtained from the resummation of $1/I(U)$ with a parabolic transform ($p = -6\Gamma$) and no Bayesian inference. The I–V characteristics is particularly interesting because, due to the asymmetry, the non-interacting low bias transmission is modified by interactions and one must first build up the Kondo resonance to approach $I \simeq (e^2/h)V_b$ (note that the unitary limit is strictly exact only at $\epsilon_d = 0$, and the conductance is slightly lower than e^2/h otherwise in the Kondo regime). This behavior leads to a non monotonous current versus U: as one increases U, the current first increases until the Kondo resonance is fully built (see the bottom panel of Fig. 5.8). As one increases further U, the Kondo width T_K shrinks and the current decreases as Coulomb blockade starts to set in.

5.3.3 Non-equilibrium electron distribution function

Finally, we discuss the out-of-equilibrium distribution function of the impurity, *i.e.* its energy-dependent probability of occupation. We define the distribution function $n(\omega)$ as:

$$n(\omega) = \frac{G^<(\omega)}{2\pi i A(\omega)} \tag{5.19}$$

so that at equilibrium $n(\omega)$ is simply the Fermi function $n_F(\omega)$. Without interaction, the distribution function amounts (at zero temperature) to a double step function $n(\omega)_{U=0} = [n_F(\omega - V_b/2) + n_F(\omega + V_b/2)]/2$. We want to investigate the behaviour of $n(\omega)$ as U

increases, a question that was not addressed in previous literature to the best of our knowledge.

The results are shown in Fig. 5.11. In this particular case, the series are fully alternated which means that the singularity lies on the negative real axis. We could sum the series using an Euler transform ($p = -8\Gamma^2$) up to $U = +\infty$. We find that the function $n(\omega)$ is not thermal, *i.e.* it can not be fitted by a Fermi function n_{F} with an effective temperature. In particular, it still exhibits discontinuities at the position of the lead Fermi surfaces, which we expect to be rounded at finite temperature. Interestingly, these discontinuities are comparable to the equilibrium quasiparticle weight for $U = 4\Gamma$, and do not seem to vanish in the limit $U = \infty$. Also very striking is the quasi-linear behavior of $n(\omega)$ that is observed for $-V_b/2 < \omega < V_b/2$.

Experiments that measure the non-equilibrium distribution function quantity typically use a third (for instance superconducting) terminal weakly coupled to the system as a probe [10, 23, 71, 125]. To the best of our knowledge, this quantity has not been measured in quantum dots, and we hope that the present prediction may stimulate some experimental activity.

Conclusion

In this work, we provided a generic exact method to compute time-dependent quantities in an interacting system in or out of equilibrium, using a real-time diagrammatic QMC and a robust resummation method for the strong interaction regime.

Our real-time diagrammatic QMC is an improved version of the one implemented in Ref. [128]. Profumo *et al.* gave a key element to avoid one source of sign problem in diagrammatic QMC on the Schwinger–Keldysh contour: the explicit sum over Keldysh indices in order to perform massive cancellations *before* the random sampling. We generalized this work to the computation of full Green's functions on a whole time range by defining and computing kernels of the Green's functions. The added computational cost is very reasonable compared to the quantity of information gained: full density of states have been obtained on a large frequency range in a single QMC run. Moreover, the complexity of the algorithm is independent of time, allowing to compute directly in the steady state regime. As for most QMC, it is generic to many Hamiltonians (geometry, type of interactions) and provides reliable error bars.

To reach strong interaction regimes, a robust resummation scheme for divergent series was introduced. We considered the resummation problem with the point of view of analytic continuation in the complex plane. The main novelty of our method is to use the location of the singularities causing the divergence, *i.e.* the analytical structure of the series. This information gives the possibility to construct tailor-made conformal transforms in order to move the singularities away from the origin of the complex plane. This appeared essential in the task of resumming a large number of series (one for each frequency). Optionally, additional non-perturbative information can be used to reduce error bars thanks to a Bayesian technique. The combination of singularity location, conformal transform crafting and Bayesian inference provides a robust and generic resummation methodology. We also show that, under the separability hypothesis — *i.e.* if a suitable conformal transform can be found — diagrammatic QMC allows to compute physical quantities with a computation time which is polynomial with the accuracy. This result is an extension of the argument provided by Rossi *et al.* [141] to the outside of the convergence disk.

We computed dynamical quantities in the Anderson impurity model from weak to strong interaction regimes, at and out of equilibrium. The precision at large interaction U has reached the level of a state-of-the-art NRG, even though our QMC yields perturbation series in U. Long time steady state and low temperatures were reached without sign problem. We obtained improved or novel results on the biased impurity and the fate of the Kondo effect under a bias voltage.

The limitations of the method are mostly yet to be explored. The extension to larger systems could lead to difficulties with the QMC algorithm. A resurgence of the sign problem when including more interacting orbitals is always possible. More certainly, relaxation processes are essential to the convergence of the QMC at long times, as it

is a condition for the clusterization property. Hence, connexion to a bath to absorb the energy introduced by the quenching of the system is necessary, and the presence of bound states is expected to break this relaxation. Systems with a phase transition or a non-Fermi liquid fixed point at low temperature could lead to difficulties in the resummation process, as singularities on the real positive U axis might appear.

A careful exploration of larger systems will shed new light to the limitations of the method. However, one may already think of fruitful applications in nanoelectronics and beyond. In nanoelectronics, the study of electronic correlations in Quantum Point Contact (QPC) by QMC is of particular interest, in order to understand the mysterious 0.7-anomaly [105]. Beyond nanoelectronics, this work may find applications within the Dynamical Mean Field Theory (DMFT), whose cornerstone is the numerical solution of impurity models with an arbitrary bath. DMFT maps an interacting lattice model (*e.g.* the Hubbard model) onto a self-consistent impurity problem. By automatizing the resummation process, our method would provide an impurity solver working directly in real frequencies. This would be valuable, as most of current solvers work in Matsubara imaginary frequencies, and physical values must be obtained by analytical continuation, introducing errors which are difficult to assess. We note, however, that real-time QMC do not provide so far a suitable solver for studying insulating phases, as the absence of bath state at the Fermi level inhibit relaxation. Other quantum embedding methods such as cluster-DMFT [99] or Trilex [14, 15] could also be considered. Application to DMFT would also provide a systematic way to study correlated materials driven out of equilibrium, by computing the real time response to a pulse or an electric field [13]. This perspective is probably the most exciting one, as it would aim at discovering new states of matter with no equilibrium equivalent.

Appendix A

Derivation of the s-d model

The Hamiltonian of a local magnetic moment coupled to the spin degree of freedom of the conduction electrons can simply be written as:

$$\mathbf{V} = -J\vec{\mathbf{S}} \cdot \vec{\mathbf{s}} \tag{A.1}$$

$\vec{\mathbf{S}}$ is the spin operator of the local moment, $\vec{\mathbf{s}}$ is the spin operator of the conduction electrons projected onto the position of the local moment. Both are in units of the Bohr magneton. J is a positive constant for ferromagnetic coupling, or negative for antiferromagnetic coupling.

In second quantization, the conduction electrons spin operator is expressed in terms of the annihilation and creation operators for an electron of spin σ (along the z axis) at the position of the local moment, which we denote $\mathbf{c}_\sigma$ and $\mathbf{c}_\sigma^\dagger$. Hence, the $i = x, y$ or z component of $\vec{\mathbf{s}}$ reads:

$$\mathbf{s}_i = \begin{pmatrix} \mathbf{c}_\uparrow^\dagger & \mathbf{c}_\downarrow^\dagger \end{pmatrix} \boldsymbol{\tau}_i \begin{pmatrix} \mathbf{c}_\uparrow \\ \mathbf{c}_\downarrow \end{pmatrix} \tag{A.2}$$

where $\boldsymbol{\tau}_i$ is the i^{th} Pauli matrix.

Introducing the ladder spin operators $\mathbf{s}^\pm \equiv \mathbf{s}_x \pm i\mathbf{s}_y$, we then have:

$$\mathbf{s}^+ = 2\mathbf{c}_\uparrow^\dagger \mathbf{c}_\downarrow \tag{A.3}$$

$$\mathbf{s}^- = 2\mathbf{c}_\downarrow^\dagger \mathbf{c}_\uparrow \tag{A.4}$$

$$\mathbf{s}_z = \mathbf{c}_\uparrow^\dagger \mathbf{c}_\uparrow - \mathbf{c}_\downarrow^\dagger \mathbf{c}_\downarrow \tag{A.5}$$

Finally, writing the conduction electrons operators in momentum space and using $\vec{\mathbf{S}} \cdot \vec{\mathbf{s}} = \frac{1}{2}\mathbf{S}^+\mathbf{s}^- + \frac{1}{2}\mathbf{S}^-\mathbf{s}^+ + \mathbf{S}_z\mathbf{s}_z$, we obtain:

$$\mathbf{V} = -J \sum_{\vec{\mathbf{k}}\vec{\mathbf{k}}'} \left[\mathbf{S}^+ \mathbf{c}_\downarrow^\dagger(\vec{\mathbf{k}}) \mathbf{c}_\uparrow(\vec{\mathbf{k}}') + \mathbf{S}^- \mathbf{c}_\uparrow^\dagger(\vec{\mathbf{k}}) \mathbf{c}_\downarrow(\vec{\mathbf{k}}') + \mathbf{S}_z \Big(\mathbf{c}_\uparrow^\dagger(\vec{\mathbf{k}}) \mathbf{c}_\uparrow(\vec{\mathbf{k}}') - \mathbf{c}_\downarrow^\dagger(\vec{\mathbf{k}}) \mathbf{c}_\downarrow(\vec{\mathbf{k}}') \Big) \right] \tag{A.6}$$

Appendix B

Expression of the kernel L as a sum of Green's functions

We show here that the kernel L can be expressed in terms of Green's functions. Starting from its definition Eq. 2.57, we follow the same steps as in section 2.2.4. We first use the fact (due to determinant symmetry) that all terms of the sum over p have the same contribution:

$$L^{ba'}_{yx'z}(u,t') = (-1)^b \sum_{n\geq 1} \frac{i^n U^n}{n!} \int_0^{t_{\mathrm{M}}} \sum_{\{a_k\}} \sum_{\{x_k,y_k\}} \prod_{k=1}^{n} [(-1)^{a_k} V_{x_k y_k}(u_k)\,\mathrm{d}u_k] \quad \times \\ 2n\,\delta_c\Big((y,u,b),U_1\Big) \left[\!\!\left[\begin{matrix} (z,t',a'), & U_1 & , U_2, \ldots, U_{2n} \\ (x',t',a'), & (z,t',a'), & U_2, \ldots, U_{2n} \end{matrix} \right]\!\!\right] \tag{B.1}$$

Then we sum out the Dirac delta:

$$L^{ba'}_{yx'z}(u,t') = 2iU \sum_{z'} V_{yz'}(u) \sum_{n\geq 0} \frac{i^n U^n}{n!} \sum_{\{a_k\}} \sum_{\{x_k,y_k\}} \int_0^{t_{\mathrm{M}}} \prod_{k=1}^{n} [(-1)^{a_k} V_{x_k y_k}(u_k)\,\mathrm{d}u_k] \quad \times \\ \left[\!\!\left[\begin{matrix} (z,t',a'), (y,u,b), (z',u,b), U_1, \ldots, U_{2n} \\ (x',t',a'), (z,t',a'), (z',u,b), U_1, \ldots, U_{2n} \end{matrix} \right]\!\!\right] \tag{B.2}$$

The pattern of a 3-particle Green's function can be recognized:

$$L^{ba'}_{yx'z}(u,t') = 2iU \sum_{z'} V_{yz'}(u) E^{ba'}_{yx'zz'}(u,t') \tag{B.3}$$

where E is defined as:

$$E^{ba'}_{yx'zz'}(u,t') \equiv \\ (-i)^3 \left\langle T^{\mathrm{c}} \mathbf{c}(y,u,b)\mathbf{c}^\dagger(x',t',a') \left[\mathbf{c}^\dagger(z,t',a')\mathbf{c}(z,t',a') - \alpha_z\right] \left[\mathbf{c}^\dagger(z',u,b)\mathbf{c}(z',u,b) - \alpha_{z'}\right] \right\rangle \tag{B.4}$$

Appendix C

Gray code

Given a set of N bits $b = b_1 b_2 \dots b_N$ (in base 2), the Gray code is an algorithm which allows to go through all possible 2^N values of b by changing one bit at a time. It is such that all values are visited in 2^N steps, *i.e.* no value is visited twice.

It goes as follows. Start with all bits set to 0. Steps are numbered between 0 and $2^N - 1$. At step number k, flip the bit b_p, where p is the position of the least significant bit of k (when written in base 2) set to 0. If k does not have any zero (last step), flip b_1. This last step should bring back to the original step where all bits of b are 0, so that it is ready to run another Gray code.

The following table shows an example for $N = 4$. The least significant bit of k set to 0 and the changed bit in b is emphasised in bold.

k	in base 2	b after step k
0	000**0**	000**1**
1	00**0**1	00**1**1
2	001**0**	001**0**
3	0**0**11	0**1**10
4	010**0**	011**1**
5	01**0**1	01**0**1
6	011**0**	010**0**
7	**0**111	**1**100
8	100**0**	110**1**
9	10**0**1	11**1**1
10	101**0**	111**0**
11	1**0**11	1**0**10
12	110**0**	101**1**
13	11**0**1	10**0**1
14	111**0**	100**0**
15	1111	**0**000

Appendix D

Proof of the clusterization property

In this appendix, we prove the clusterization property for the Green's functions (as done in [128]) and we extend it to the kernels K, $\bar{K}$ and L. We want to show that, if some of the times u_i are sent to infinity in the integral in Eq. 2.31, 2.49, 2.52 and 2.57, the Keldysh sum under the integral vanishes (while each determinant taken individually does not). We will not try to prove here the stronger property that the integrals do indeed converge but we observe it empirically in the numerical computations.

Let us restart from the clusterization proof of Ref. [128] for Eq. 2.31 and examine the sum over the Keldysh indices:

$$S \equiv \sum_{\{a_k\}} \prod_{k=1}^{n} (-1)^{a_k} \left[\!\!\left[\begin{matrix} (x,t,a) \\ (x',t',a') \end{matrix}, U_1, \dots, U_{2n} \right]\!\!\right] \tag{D.1}$$

$$= \sum_{\{a_k\}} \prod_{k=1}^{n} (-1)^{a_k} \begin{vmatrix} g(X,X') & g(X,U_1) & \dots & g(X,U_{2n}) \\ g(U_1,X') & g(U_1,U_1) & \dots & g(U_1,U_{2n}) \\ \vdots & \vdots & \ddots & \vdots \\ g(U_{2n},X') & g(U_{2n},U_1) & \dots & g(U_{2n},U_{2n}) \end{vmatrix} \tag{D.2}$$

If some u_i are sent to infinity, we can relabel them $u_{p+1}, \dots, u_n$. Since g vanishes at large time (due to the presence of the bath), the determinants in the sum become diagonal by block:

$$S \approx \sum_{\{a_k\}} \prod_{k=1}^{n} (-1)^{a_k} \quad \times$$

$$\begin{vmatrix} g(X,X') & g(X,U_1) & \dots & g(X,U_{2p}) & 0 & \dots & 0 \\ g(U_1,X') & g(U_1,U_1) & \dots & g(U_1,U_{2p}) & 0 & \dots & 0 \\ \vdots & \vdots & \ddots & \vdots & \vdots & \ddots & \vdots \\ g(U_{2p},X') & g(U_{2p},U_1) & \dots & g(U_{2p},U_{2p}) & 0 & \dots & 0 \\ 0 & 0 & \dots & 0 & g(U_{2p+1},U_{2p+1}) & \dots & g(U_{2p+1},U_{2n}) \\ \vdots & \vdots & \ddots & \vdots & \vdots & \ddots & \vdots \\ 0 & 0 & \dots & 0 & g(U_{2n},U_{2p+1}) & \dots & g(U_{2n},U_{2n}) \end{vmatrix} \tag{D.3}$$

The upper-left determinant does not depend on $a_{p+1}, \dots, a_n$, so we can apply Eq. 2.34 to the bottom-right determinant and the sum S vanishes.

Let us now turn to the kernel K defined in Eq. 2.49. The situation is slightly different. First, with a simple relabelling, we can restrict ourselves to the case $p = 1$ in Eq. 2.49.

Let us first split the U into two subsets:

$$S = \sum_{\{a_k\}} \prod_{k=1}^{n} (-1)^{a_k} \quad \times$$
$$\begin{vmatrix} g(U_1, X') & g(U_1, U_2) & \dots & g(U_1, U_{2p}) & g(U_1, U_{2p+1}) & \dots & g(U_1, U_{2n}) \\ \vdots & \vdots & \ddots & \vdots & \vdots & \ddots & \vdots \\ g(U_{2p}, X') & g(U_{2p}, U_2) & \dots & g(U_{2p}, U_{2p}) & g(U_{2p}, U_{2p+1}) & \dots & g(U_{2p}, U_{2n}) \\ g(U_{2p+1}, X') & g(U_{2p+1}, U_2) & \dots & g(U_{2p+1}, U_{2p}) & g(U_{2p+1}, U_{2p+1}) & \dots & g(U_{2p+1}, U_{2n}) \\ \vdots & \vdots & \ddots & \vdots & \vdots & \ddots & \vdots \\ g(U_{2n}, X') & g(U_{2n}, U_2) & \dots & g(U_{2n}, U_{2p}) & g(U_{2n}, U_{2p+1}) & \dots & g(U_{2n}, U_{2n}) \end{vmatrix} \tag{D.4}$$

Some u_i go to infinity. We distinguish two cases.

1. If u_1 does not go to infinity, we can relabel the indices so that $u_{p+1}, \dots, u_n$ go to infinity.

2. If u_1 goes to infinity, we can relabel the indices so that $u_1, \dots, u_p$ go to infinity.

In both cases, the upper-right part of the matrix vanishes and we get a block-trigonal determinant

$$S \approx \sum_{\{a_k\}} \prod_{k=1}^{n} (-1)^{a_k} \quad \times$$
$$\begin{vmatrix} g(U_1, X') & g(U_1, U_2) & \dots & g(U_1, U_{2p}) & 0 & \dots & 0 \\ \vdots & \vdots & \ddots & \vdots & \vdots & \ddots & \vdots \\ g(U_{2p}, X') & g(U_{2p}, U_2) & \dots & g(U_{2p}, U_{2p}) & 0 & \dots & 0 \\ g(U_{2p+1}, X') & g(U_{2p+1}, U_2) & \dots & g(U_{2p+1}, U_{2p}) & g(U_{2p+1}, U_{2p+1}) & \dots & g(U_{2p+1}, U_{2n}) \\ \vdots & \vdots & \ddots & \vdots & \vdots & \ddots & \vdots \\ g(U_{2n}, X') & g(U_{2n}, U_2) & \dots & g(U_{2n}, U_{2p}) & g(U_{2n}, U_{2p+1}) & \dots & g(U_{2n}, U_{2n}) \end{vmatrix}$$

$$= \left(\sum_{a_1, \dots, a_p} \prod_{k=1}^{p} (-1)^{a_k} \left[\!\!\left[\begin{matrix} U_1, U_2, \dots, U_{2p} \\ X', U_2, \dots, U_{2p} \end{matrix} \right]\!\!\right] \right) \times \left(\sum_{a_{p+1}, \dots, a_n} \prod_{k=p+1}^{n} (-1)^{a_k} \left[\!\!\left[\begin{matrix} U_{2p+1}, \dots, U_{2n} \\ U_{2p+1}, \dots, U_{2n} \end{matrix} \right]\!\!\right] \right) \tag{D.5}$$

since the first determinant does not depend on $a_{p+1}, \dots, a_n$. The second term cancels because of Eq. 2.34.

≈

Appendix E

Convergence of the perturbation series at finite time

In this appendix, we show that at *finite* time t, the radius of convergence of the perturbation series for an operator $\mathbf{O}$ is infinite, for a system with an interaction on a finite number of sites and an infinite bath. Indeed, the average is given by:

$$\langle \mathbf{O}(t) \rangle \propto \left\langle T^{\mathrm{c}} e^{-iU \int \mathbf{H}_{\mathrm{int}}(u) \mathrm{d}u} \mathbf{O}(t) \right\rangle \tag{E.1}$$

where the integral goes along the forward-backward Schwinger–Keldysh contour $0 \to t \to 0$, the operators are taken in the interaction representation, T^{c} is the usual contour ordering operator and $\mathbf{H}_{\mathrm{int}}(u)$ is the interacting part of the Hamiltonian.

More precisely, each of the 2^n terms of the expansion of the exponential has the form:

$$\frac{U^n}{n!} \int_{[0,t]^n} \mathrm{d}u_1 \dots \mathrm{d}u_n \, \langle \mathbf{O}(t) C(u_1, \dots, u_n) \rangle \tag{E.2}$$

where C is a product of $\mathbf{c}$, $\mathbf{c}^\dagger$, and unitary time evolution operators.

The terms $\langle \mathbf{O}(t) C(u_1, \dots, u_n) \rangle$ are amplitudes of probability for quantum processes and are therefore bounded. Introducing eigenstates $|\psi\rangle$ of $\mathbf{H}_0$, we have explicitly:

$$\langle \mathbf{O}(t) C(u_1, \dots u_n) \rangle = \mathrm{Tr} \left(\frac{e^{-\beta \mathbf{H}_0}}{Z_0} \mathbf{O}(t) C(u_1, \dots, u_n) \right) \tag{E.3}$$

$$= \sum_\psi \langle \psi | \frac{e^{-\beta \mathbf{H}_0}}{Z_0} \mathbf{O}(t) C(u_1, \dots, u_n) | \psi \rangle \tag{E.4}$$

$$|\langle \mathbf{O}(t) C(u_1, \dots, u_n) \rangle| \leq \sum_\psi \frac{e^{-\beta E_\psi}}{Z_0} \| \mathbf{O}(t) C(u_1, \dots, u_n) \psi \| \times \| \psi \| \tag{E.5}$$

$$\leq \sum_\psi \frac{e^{-\beta E_\psi}}{Z_0} \| \mathbf{O}(t) C(u_1, \dots, u_n) \| \times \| \psi \|^2 \tag{E.6}$$

$$\leq \| \mathbf{O} \| \tag{E.7}$$

where $\|v\|$ is the norm for a vector and the induced norm for an operator. We note that the norm is not modified by the unitary evolution $\left\| e^{i\mathbf{H}_0 u} \mathbf{A} e^{-i\mathbf{H}_0 u} \right\| = \|\mathbf{A}\|$ for any operator $\mathbf{A}$, and for the canonical operators $\|\mathbf{c}\| = 1$, as can be checked in the Fock basis,

independently of the size of the bath. Since the norm is sub-multiplicative, we obtain the last inequality.

Therefore, the term of order n in the expansion of Eq. E.1 is controlled by a bound $\|\mathbf{O}\|(2UtL)^n/n!$ (where L is the number of terms in $\mathbf{H}_{\text{int}}$), so the series has an infinite radius of convergence. Note that this argument is valid because the electron-electron interaction is present on a finite number of sites only. It would not apply directly to *e.g.* the Hubbard model in the thermodynamic limit.

Bibliography

[1] A. A. Abrikosov, "Electron scattering on magnetic impurities in metals and anomalous resistivity effects", **Physics Physique Fizika 2, 5–20 (1965)** (cit. on p. 14).

[2] I. L. Aleiner, P. W. Brouwer, and L. I. Glazman, "Quantum effects in Coulomb blockade", **Physics Reports 358, 309–440 (2002)** (cit. on p. 22).

[3] S. Andergassen, V. Meden, H. Schoeller, J. Splettstoesser, and M. R. Wegewijs, "Charge transport through single molecules, quantum dots and quantum wires", **Nanotechnology 21, 272001 (2010)** (cit. on p. 22).

[4] F. B. Anders, "Steady-state currents through nanodevices: a scattering-states numerical renormalization-group approach to open quantum systems", **Phys. Rev. Lett. 101, 066804 (2008)** (cit. on pp. 9, 24, 85).

[5] F. B. Anders and A. Schiller, "Real-time dynamics in quantum-impurity systems: a time-dependent numerical renormalization-group approach", **Phys. Rev. Lett. 95, 196801 (2005)** (cit. on pp. 9, 24).

[6] F. B. Anders and A. Schiller, "Spin precession and real-time dynamics in the Kondo model: time-dependent numerical renormalization-group study", **Phys. Rev. B 74, 245113 (2006)** (cit. on p. 24).

[7] P. W. Anderson, "A poor man's derivation of scaling laws for the Kondo problem", **Journal of Physics C: Solid State Physics 3, 2436–2441 (1970)** (cit. on pp. 11, 15).

[8] P. W. Anderson, "Localized magnetic states in metals", **Phys. Rev. 124, 41–53 (1961)** (cit. on pp. 10, 19, 20).

[9] N. Andrei, "Diagonalization of the Kondo Hamiltonian", **Phys. Rev. Lett. 45, 379–382 (1980)** (cit. on pp. 7, 18).

[10] A. Anthore, F. Pierre, H. Pothier, and D. Esteve, "Magnetic-field-dependent quasiparticle energy relaxation in mesoscopic wires", **Phys. Rev. Lett. 90, 076806 (2003)** (cit. on p. 87).

[11] A. E. Antipov, Q. Dong, and E. Gull, "Voltage quench dynamics of a Kondo system", **Phys. Rev. Lett. 116, 036801 (2016)** (cit. on pp. 9, 25).

[12] A. E. Antipov, Q. Dong, J. Kleinhenz, G. Cohen, and E. Gull, "Currents and Green's functions of impurities out of equilibrium: Results from inchworm quantum Monte Carlo", **Phys. Rev. B 95, 085144 (2017)** (cit. on pp. 9, 25).

[13] H. Aoki, N. Tsuji, M. Eckstein, M. Kollar, T. Oka, and P. Werner, "Nonequilibrium dynamical mean-field theory and its applications", **Rev. Mod. Phys. 86, 779–837 (2014)** (cit. on pp. 8, 90).

[14]T. Ayral and O. Parcollet, "Mott physics and spin fluctuations: A unified framework", **Phys. Rev. B 92, 115109 (2015)** (cit. on pp. 8, 90).

[15]T. Ayral, J. Vučičević, and O. Parcollet, "Fierz convergence criterion: A controlled approach to strongly interacting systems with small embedded clusters", **Phys. Rev. Lett. 119, 166401 (2017)** (cit. on pp. 8, 90).

[16]G. Baker and P. Graves-Morris, *Padé approximants*, Encyclopedia of Mathematics and its Applications (Cambridge University Press, 1996) (cit. on pp. 9, 61).

[17]B. J. Berne and D. Thirumalai, "On the simulation of quantum systems: path integral methods", **Annu. Rev. Phys. Chem. 37, 401–424 (1986)** (cit. on p. 24).

[18]R. Bulla, A. C. Hewson, and T. Pruschke, "Numerical renormalization group calculations for the self-energy of the impurity Anderson model", **J. Phys.: Condens. Matter 10, 8365 (1998)** (cit. on pp. 21, 39, 79).

[19]R. Bulla, T. A. Costi, and T. Pruschke, "Numerical renormalization group method for quantum impurity systems", **Rev. Mod. Phys. 80, 395–450 (2008)** (cit. on pp. 7, 9, 16, 21).

[20]E. Casandruc, D. Nicoletti, S. Rajasekaran, Y. Laplace, V. Khanna, G. D. Gu, J. P. Hill, and A. Cavalleri, "Wavelength-dependent optical enhancement of superconducting interlayer coupling in $La_{1.885}Ba_{0.115}CuO_4$", **Phys. Rev. B 91, 174502 (2015)** (cit. on p. 8).

[21]H.-T. Chen, G. Cohen, and D. R. Reichman, "Inchworm Monte Carlo for exact non-adiabatic dynamics. I. Theory and algorithms", **J. Chem. Phys. 146, 054105 (2017)** (cit. on pp. 9, 25, 45).

[22]H.-T. Chen, G. Cohen, and D. R. Reichman, "Inchworm Monte Carlo for exact non-adiabatic dynamics. II. Benchmarks and comparison with established methods", **J. Chem. Phys. 146, 054106 (2017)** (cit. on pp. 9, 25, 45).

[23]Y.-F. Chen, T. Dirks, G. Al-Zoubi, N. O. Birge, and N. Mason, "Nonequilibrium tunneling spectroscopy in carbon nanotubes", **Phys. Rev. Lett. 102, 036804 (2009)** (cit. on p. 87).

[24]G. Cohen, E. Gull, D. R. Reichman, and A. J. Millis, "Green's functions from real-time bold-line Monte Carlo calculations: Spectral properties of the nonequilibrium Anderson impurity model", **Phys. Rev. Lett. 112, 146802 (2014)** (cit. on pp. 9, 25, 45, 84).

[25]G. Cohen, E. Gull, D. R. Reichman, and A. J. Millis, "Taming the dynamical sign problem in real-time evolution of quantum many-body problems", **Phys. Rev. Lett. 115, 266802 (2015)** (cit. on pp. 9, 25, 45).

[26]G. Cohen, D. R. Reichman, A. J. Millis, and E. Gull, "Green's functions from real-time bold-line Monte Carlo", **Phys. Rev. B 89, 115139 (2014)** (cit. on pp. 9, 25, 45).

[27]D. L. Cox and A. Zawadowski, "Exotic Kondo effects in metals: Magnetic ions in a crystalline electric field and tunnelling centres", **Adv. Phys. 47, 599–942 (1998)** (cit. on p. 13).

[28]S. M. Cronenwett, T. H. Oosterkamp, and L. P. Kouwenhoven, "A tunable Kondo effect in quantum dots", **Science 281, 540–544 (1998)** (cit. on pp. 7, 18).

[29]A. J. Daley, C. Kollath, U. Schollwöck, and G. Vidal, "Time-dependent density-matrix renormalization-group using adaptive effective Hilbert spaces", **J. Stat. Mech. Theory Exp. 2004, P04005 (2004)** (cit. on p. 24).

[30]S. De Franceschi, R. Hanson, W. G. van der Wiel, J. M. Elzerman, J. J. Wijpkema, T. Fujisawa, S. Tarucha, and L. P. Kouwenhoven, "Out-of-equilibrium Kondo effect in a mesoscopic device", **Phys. Rev. Lett. 89, 156801 (2002)** (cit. on p. 24).

[31]T. Delattre, C. Feuillet-Palma, L. G. Herrmann, P. Morfin, J.-M. Berroir, G. Fève, B. Plaçais, D. C. Glattli, M.-S. Choi, C. Mora, and T. Kontos, "Noisy Kondo impurities", **Nat. Phys. 5, 208 (2009)** (cit. on p. 7).

[32]Y. Deng, E. Kozik, N. V. Prokof'ev, and B. V. Svistunov, "Emergent BCS regime of the two-dimensional fermionic Hubbard model: Ground-state phase diagram", **EPL 110, 57001 (2015)** (cit. on p. 45).

[33]A. Dirks, S. Schmitt, J. E. Han, F. Anders, P. Werner, and T. Pruschke, "Double occupancy and magnetic susceptibility of the Anderson impurity model out of equilibrium", **EPL (Europhysics Letters) 102, 37011 (2013)** (cit. on pp. 24, 25).

[34]B. Doyon and N. Andrei, "Universal aspects of nonequilibrium currents in a quantum dot", **Phys. Rev. B 73, 245326 (2006)** (cit. on p. 35).

[35]T. A. Driscoll and L. N. Trefethen, *Schwarz-Christoffel mapping*, Cambridge Monographs on Applied and Computational Mathematics (Cambridge University Press, 2002) (cit. on p. 63).

[36]J. Eckel, F. Heidrich-Meisner, S. G. Jakobs, M. Thorwart, M. Pletyukhov, and R. Egger, "Comparative study of theoretical methods for non-equilibrium quantum transport", **New J. Phys. 12, 043042 (2010)** (cit. on pp. 24, 25).

[37]D. Fausti, R. I. Tobey, N. Dean, S. Kaiser, A. Dienst, M. C. Hoffmann, S. Pyon, T. Takayama, H. Takagi, and A. Cavalleri, "Light-induced superconductivity in a stripe-ordered cuprate", **Science 331, 189–191 (2011)** (cit. on p. 8).

[38]T. Fujii and K. Ueda, "Perturbative approach to the nonequilibrium Kondo effect in a quantum dot", **Phys. Rev. B 68, 155310 (2003)** (cit. on pp. 23, 83).

[39]M. Gaudin, "Une démonstration simplifiée du théorème de Wick en mécanique statistique", **Nucl. Phys. 15, 89–91 (1960)** (cit. on p. 30).

[40]A. Georges, G. Kotliar, W. Krauth, and M. J. Rozenberg, "Dynamical mean-field theory of strongly correlated fermion systems and the limit of infinite dimensions", **Rev. Mod. Phys. 68, 13–125 (1996)** (cit. on p. 8).

[41]L. I. Glazman and M. E. Raikh, "Resonant Kondo transparency of a barrier with quasilocal impurity states.", **JETP Lett. 47, 452–455 (1988)** (cit. on p. 22).

[42]D. Goldhaber-Gordon, J. Göres, M. A. Kastner, H. Shtrikman, D. Mahalu, and U. Meirav, "From the Kondo regime to the mixed-valence regime in a single-electron transistor", **Phys. Rev. Lett. 81, 5225–5228 (1998)** (cit. on pp. 7, 18).

[43]D. Goldhaber-Gordon, H. Shtrikman, D. Mahalu, D. Abusch-Magder, U. Meirav, and M. A. Kastner, "Kondo effect in a single-electron transistor", **Nature 391, 156 (1998)** (cit. on pp. 7, 18, 19).

[44]E. Gull, P. Werner, O. Parcollet, and M. Troyer, "Continuous-time auxiliary-field Monte Carlo for quantum impurity models", **EPL 82, 57003 (2008)** (cit. on pp. 9, 21, 24, 45, 56).

[45]E. Gull, A. J. Millis, A. I. Lichtenstein, A. N. Rubtsov, M. Troyer, and P. Werner, "Continuous-time Monte Carlo methods for quantum impurity models", **Rev. Mod. Phys. 83, 349–404 (2011)** (cit. on pp. 8, 21, 45).

[46]E. Gull, D. R. Reichman, and A. J. Millis, "Bold-line diagrammatic Monte Carlo method: general formulation and application to expansion around the noncrossing approximation", **Phys. Rev. B 82, 075109 (2010)** (cit. on p. 45).

[47]E. Gull, D. R. Reichman, and A. J. Millis, "Numerically exact long-time behavior of nonequilibrium quantum impurity models", **Phys. Rev. B 84, 085134 (2011)** (cit. on pp. 9, 25).

[48]E. Gull, P. Werner, A. Millis, and M. Troyer, "Performance analysis of continuous-time solvers for quantum impurity models", **Phys. Rev. B 76, 235123 (2007)** (cit. on p. 45).

[49]A. J. Guttmann, *Asymptotic analysis of power-series expansions*, edited by C. Domb and J. Lebowitz, Vol. 13, Domb C., Lebowitz J. - Phase Transitions and Critical Phenomena (Academic Press, 1989) (cit. on p. 62).

[50]W. de Haas, J. de Boer, and G. van dën Berg, "The electrical resistance of gold, copper and lead at low temperatures", **Physica 1, 1115–1124 (1934)** (cit. on p. 12).

[51]H. Hafermann, K. R. Patton, and P. Werner, "Improved estimators for the self-energy and vertex function in hybridization-expansion continuous-time quantum Monte Carlo simulations", **Phys. Rev. B 85, 205106 (2012)** (cit. on p. 39).

[52]F. D. M. Haldane, "Scaling theory of the asymmetric Anderson model", **Phys. Rev. Lett. 40, 416–419 (1978)** (cit. on pp. 20, 21).

[53]J. M. Hammersley and D. C. Handscomb, *Monte Carlo methods*, Monographs on Statistics and Applied Probability (Springer Netherlands, 1964) (cit. on p. 48).

[54]J. E. Han and R. J. Heary, "Imaginary-time formulation of steady-state nonequilibrium: Application to strongly correlated transport", **Phys. Rev. Lett. 99, 236808 (2007)** (cit. on p. 24).

[55]J. E. Han, A. Dirks, and T. Pruschke, "Imaginary-time quantum many-body theory out of equilibrium: Formal equivalence to Keldysh real-time theory and calculation of static properties", **Phys. Rev. B 86, 155130 (2012)** (cit. on p. 24).

[56]G. H. Hardy, *Divergent series* (Oxford University Press, Oxford, 1949) (cit. on pp. 9, 61).

[57]R. Härtle, G. Cohen, D. R. Reichman, and A. J. Millis, "Transport through an Anderson impurity: Current ringing, nonlinear magnetization, and a direct comparison of continuous-time quantum Monte Carlo and hierarchical quantum master equations", **Phys. Rev. B 92, 085430 (2015)** (cit. on p. 24).

[58]W. K. Hastings, "Monte Carlo sampling methods using Markov chains and their applications", **Biometrika 57, 97–109 (1970)** (cit. on p. 48).

[59]R. Hedden, V. Meden, T. Pruschke, and K. Schönhammer, "A functional renormalization group approach to zero-dimensional interacting systems", **J. Phys.: Condens. Matter 16, 5279–5296 (2004)** (cit. on p. 24).

[60]F. Heidrich-Meisner, A. E. Feiguin, and E. Dagotto, "Real-time simulations of nonequilibrium transport in the single-impurity Anderson model", **Phys. Rev. B 79, 235336 (2009)** (cit. on pp. 9, 24).

[61]S. Hershfield, J. H. Davies, and J. W. Wilkins, "Probing the Kondo resonance by resonant tunneling through an Anderson impurity", **Phys. Rev. Lett. 67, 3720–3723 (1991)** (cit. on p. 85).

[62]S. Hershfield, J. H. Davies, and J. W. Wilkins, "Resonant tunneling through an Anderson impurity. I. Current in the symmetric model", **Phys. Rev. B 46, 7046–7060 (1992)** (cit. on p. 85).

[63]A. Hewson, "Renormalization group and Fermi liquid theory", **Adv. Phys. 43, 543–575 (1994)** (cit. on pp. 12, 20).

[64]A. C. Hewson, *The Kondo problem to heavy fermions*, Cambridge Studies in Magnetism (Cambridge University Press, 1993) (cit. on pp. 11, 13).

[65]R. Hiraoka, E. Minamitani, R. Arafune, N. Tsukahara, S. Watanabe, M. Kawai, and N. Takagi, "Single-molecule quantum dot as a Kondo simulator", **Nat. Commun. 8, 16012 (2017)** (cit. on p. 19).

[66]J. E. Hirsch and R. M. Fye, "Monte Carlo method for magnetic impurities in metals", **Phys. Rev. Lett. 56, 2521–2524 (1986)** (cit. on pp. 21, 45).

[67]W. Hofstetter, "Generalized numerical renormalization group for dynamical quantities", **Phys. Rev. Lett. 85, 1508–1511 (2000)** (cit. on p. 78).

[68]B. Horvatić, D. Sokcević, and V. Zlatić, "Finite-temperature spectral density for the Anderson model", **Phys. Rev. B 36, 675–683 (1987)** (cit. on pp. 20, 21).

[69]B. Horvatić and V. Zlatić, "Equivalence of the perturbative and Bethe-Ansatz solution of the symmetric Anderson Hamiltonian", **J. Phys. France 46, 1459–1467 (1985)** (cit. on pp. 66, 67, 70, 76, 77).

[70]Y. Huang, K. Chen, Y. Deng, N. Prokof'ev, and B. Svistunov, "Spin-ice state of the quantum Heisenberg antiferromagnet on the pyrochlore lattice", **Phys. Rev. Lett. 116, 177203 (2016)** (cit. on p. 45).

[71]B. Huard, A. Anthore, F. Pierre, H. Pothier, N. O. Birge, and D. Esteve, "Intensity of Coulomb interaction between quasiparticles in diffusive metallic wires", **Solid State Commun. 131, 599–607 (2004)** (cit. on p. 87).

[72]K. L. Hur, B. I. Halperin, and A. Yacoby, "Charge fractionalization in nonchiral Luttinger systems", **Ann. Phys. (N. Y.) 323, 3037–3058 (2008)** (cit. on p. 7).

[73]Z. Iftikhar, A. Anthore, A. K. Mitchell, F. D. Parmentier, U. Gennser, A. Ouerghi, A. Cavanna, C. Mora, P. Simon, and F. Pierre, "Tunable quantum criticality and super-ballistic transport in a "charge" Kondo circuit", **Science 360, 1315–1320 (2018)** (cit. on pp. 7, 19).

[74]Z. Iftikhar, S. Jezouin, A. Anthore, U. Gennser, F. D. Parmentier, A. Cavanna, and F. Pierre, "Two-channel Kondo effect and renormalization flow with macroscopic quantum charge states", **Nature 526, 233 (2015)** (cit. on p. 19).

[75]S. G. Jakobs, M. Pletyukhov, and H. Schoeller, "Nonequilibrium functional renormalization group with frequency-dependent vertex function: A study of the single-impurity Anderson model", **Phys. Rev. B 81, 195109 (2010)** (cit. on p. 24).

[76]P. Jarillo-Herrero, J. Kong, H. S. J. van der Zant, C. Dekker, L. P. Kouwenhoven, and S. De Franceschi, "Orbital Kondo effect in carbon nanotubes", **Nature 434, 484 (2005)** (cit. on p. 19).

[77]S. C. Kapfer and W. Krauth, "Irreversible local Markov chains with rapid convergence towards equilibrium", **Phys. Rev. Lett. 119, 240603 (2017)** (cit. on p. 49).

[78]N. Kawakami and A. Okiji, "Exact expression of the ground-state energy for the symmetric Anderson model", **Phys. Lett. A 86, 483–486 (1981)** (cit. on pp. 7, 20).

[79]L. V. Keldysh, "Diagram technique for nonequilibrium processes", **Sov. Phys. JETP 20, [Zh. Eksp. Theor. Fiz. 47, 1515 (1964)], 1018 (1965)** (cit. on pp. 9, 29).

[80]D. M. Kennes and V. Meden, "Quench dynamics of correlated quantum dots", **Phys. Rev. B 85, 245101 (2012)** (cit. on p. 24).

[81]U. F. Keyser, C. Fühner, S. Borck, R. J. Haug, M. Bichler, G. Abstreiter, and W. Wegscheider, "Kondo effect in a few-electron quantum ring", **Phys. Rev. Lett. 90, 196601 (2003)** (cit. on p. 19).

[82]A. Koga, "Quantum monte carlo study of nonequilibrium transport through a quantum dot coupled to normal and superconducting leads", **Phys. Rev. B 87, 115409 (2013)** (cit. on p. 24).

[83]J. Kondo, "Resistance minimum in dilute magnetic alloys", **Prog. Theor. Phys. 32, 37–49 (1964)** (cit. on pp. 7, 12).

[84]G. Kotliar, S. Y. Savrasov, K. Haule, V. S. Oudovenko, O. Parcollet, and C. A. Marianetti, "Electronic structure calculations with dynamical mean-field theory", **Rev. Mod. Phys. 78, 865–951 (2006)** (cit. on p. 8).

[85]L. Kouwenhoven and L. Glazman, "Revival of the Kondo effect", **Physics World 14, 33–38 (2001)** (cit. on p. 7).

[86]E. Kozik, K. V. Houcke, E. Gull, L. Pollet, N. Prokof'ev, B. Svistunov, and M. Troyer, "Diagrammatic Monte Carlo for correlated fermions", **EPL 90, 10004 (2010)** (cit. on p. 45).

[87]W. Krauth, *Statistical mechanics: algorithms and computations*, Oxford Master Series in Statistical, Computational, and Theoretical Physics (Oxford University Press, 2006) (cit. on pp. 49, 54).

[88]A. V. Kretinin, H. Shtrikman, D. Goldhaber-Gordon, M. Hanl, A. Weichselbaum, J. von Delft, T. Costi, and D. Mahalu, "Spin-$\frac{1}{2}$ Kondo effect in an InAs nanowire quantum dot: Unitary limit, conductance scaling, and Zeeman splitting", **Phys. Rev. B 84, 245316 (2011)** (cit. on pp. 7, 19, 23).

[89]H. R. Krishna-murthy, J. W. Wilkins, and K. G. Wilson, "Renormalization-group approach to the Anderson model of dilute magnetic alloys. I. Static properties for the symmetric case", **Phys. Rev. B 21, 1003–1043 (1980)** (cit. on p. 21).

[90]H. R. Krishna-murthy, J. W. Wilkins, and K. G. Wilson, "Renormalization-group approach to the Anderson model of dilute magnetic alloys. II. Static properties for the asymmetric case", **Phys. Rev. B 21, 1044–1083 (1980)** (cit. on p. 21).

[91]I. Krivenko, J. Kleinhenz, G. Cohen, and E. Gull, "Dynamics of the Kondo voltage splitting after a quantum quench", **arXiv:1904.11527 (2019)** (cit. on pp. 9, 25).

[92]P. Kubiczek, A. N. Rubtsov, and A. I. Lichtenstein, "Exact real-time dynamics of single-impurity anderson model from a single-spin hybridization-expansion", **arXiv:1904.12582 (2019)** (cit. on p. 24).

[93]S. A. Kulagin, N. Prokof'ev, O. A. Starykh, B. Svistunov, and C. N. Varney, "Bold diagrammatic Monte Carlo method applied to fermionized frustrated spins", **Phys. Rev. Lett. 110, 070601 (2013)** (cit. on p. 45).

[94]S. A. Kulagin, N. Prokof'ev, O. A. Starykh, B. Svistunov, and C. N. Varney, "Bold diagrammatic Monte Carlo technique for frustrated spin systems", **Phys. Rev. B 87, 024407 (2013)** (cit. on p. 45).

[95]N. Lanatà and H. U. R. Strand, "Time-dependent and steady-state gutzwiller approach for nonequilibrium transport in nanostructures", **Phys. Rev. B 86, 115310 (2012)** (cit. on p. 24).

[96]R. Leturcq, L. Schmid, K. Ensslin, Y. Meir, D. C. Driscoll, and A. C. Gossard, "Probing the Kondo density of states in a three-terminal quantum ring", **Phys. Rev. Lett. 95, 126603 (2005)** (cit. on p. 24).

[97]E. Lindelöf, *Le calcul des résidus et ses applications à la théorie des fonctions* (Gauthier-Villars, 1905) (cit. on pp. 9, 61).

[98]A. Lorke, R. Johannes Luyken, A. O. Govorov, J. P. Kotthaus, J. M. Garcia, and P. M. Petroff, "Spectroscopy of nanoscopic semiconductor rings", **Phys. Rev. Lett. 84, 2223–2226 (2000)** (cit. on p. 7).

[99]T. Maier, M. Jarrell, T. Pruschke, and M. H. Hettler, "Quantum cluster theories", **Rev. Mod. Phys. 77, 1027–1080 (2005)** (cit. on p. 90).

[100]C. H. Mak and R. Egger, "A multilevel blocking approach to the sign problem in real-time quantum Monte Carlo simulations", **J. Chem. Phys. 110, 12–14 (1999)** (cit. on p. 24).

[101]H. C. Manoharan, C. P. Lutz, and D. M. Eigler, "Quantum mirages formed by coherent projection of electronic structure", **Nature 403, 512–515 (2000)** (cit. on p. 18).

[102]Y. Meir and N. S. Wingreen, "Landauer formula for the current through an interacting electron region", **Phys. Rev. Lett. 68, 2512–2515 (1992)** (cit. on pp. 23, 75).

[103]Y. Meir, N. S. Wingreen, and P. A. Lee, "Low-temperature transport through a quantum dot: the Anderson model out of equilibrium", **Phys. Rev. Lett. 70, 2601–2604 (1993)** (cit. on p. 23).

[104]N. Metropolis, A. W. Rosenbluth, M. N. Rosenbluth, A. H. Teller, and E. Teller, "Equation of state calculations by fast computing machines", **J. Chem. Phys. 21, 1087–1092 (1953)** (cit. on p. 48).

[105]A. P. Micolich, "What lurks below the last plateau: experimental studies of the $0.7 \times 2e^2/h$ conductance anomaly in one-dimensional systems", **J. Phys.: Condens. Matter 23, 443201 (2011)** (cit. on p. 90).

[106]M. Moeckel and S. Kehrein, "Real-time evolution for weak interaction quenches in quantum systems", **Ann. Phys. (N. Y.) 324, 2146–2178 (2009)** (cit. on p. 8).

[107]C. Mora and K. Le Hur, "Universal resistances of the quantum resistance–capacitance circuit", **Nat. Phys. 6, Article, 697 (2010)** (cit. on p. 7).

[108]A. Moutenet, P. Seth, M. Ferrero, and O. Parcollet, "Cancellation of vacuum diagrams and long-time limit in out-of-equilibrium diagrammatic quantum Monte Carlo", **arXiv:1904.11969 (2019)** (cit. on p. 51).

[109]A. Moutenet, W. Wu, and M. Ferrero, "Determinant Monte Carlo algorithms for dynamical quantities in fermionic systems", **Phys. Rev. B 97, 085117 (2018)** (cit. on pp. 9, 45).

[110]L. Mühlbacher and R. Egger, "Crossover from nonadiabatic to adiabatic electron transfer reactions: Multilevel blocking Monte Carlo simulations", **J. Chem. Phys. 118, 179–191 (2003)** (cit. on p. 24).

[111]L. Mühlbacher, D. F. Urban, and A. Komnik, "Anderson impurity model in nonequilibrium: Analytical results versus quantum Monte Carlo data", **Phys. Rev. B 83, 075107 (2011)** (cit. on pp. 24, 45).

[112]L. Mühlbacher and E. Rabani, "Real-time path integral approach to nonequilibrium many-body quantum systems", **Phys. Rev. Lett. 100, 176403 (2008)** (cit. on pp. 24, 45).

[113]F. Nakamura, M. Sakaki, Y. Yamanaka, S. Tamaru, T. Suzuki, and Y. Maeno, "Electric-field-induced metal maintained by current of the Mott insulator Ca_2RuO_4", **Sci. Rep. 3, Article, 2536 (2013)** (cit. on p. 8).

[114]T. K. Ng and P. A. Lee, "On-site Coulomb repulsion and resonant tunneling", **Phys. Rev. Lett. 61, 1768–1771 (1988)** (cit. on p. 22).

[115]D. Nicoletti, E. Casandruc, Y. Laplace, V. Khanna, C. R. Hunt, S. Kaiser, S. S. Dhesi, G. D. Gu, J. P. Hill, and A. Cavalleri, "Optically induced superconductivity in striped $La_{2-x}Ba_xCuO_4$ by polarization-selective excitation in the near infrared", **Phys. Rev. B 90, 100503 (2014)** (cit. on p. 8).

[116]D. Nicoletti, D. Fu, O. Mehio, S. Moore, A. S. Disa, G. D. Gu, and A. Cavalleri, "Magnetic-field tuning of light-induced superconductivity in striped $La_{2-x}Ba_xCuO_4$", **Phys. Rev. Lett. 121, 267003 (2018)** (cit. on p. 8).

[117]D. Nicoletti and A. Cavalleri, "Nonlinear light–matter interaction at terahertz frequencies", **Adv. Opt. Photon. 8, 401–464 (2016)** (cit. on p. 8).

[118]P. Nordlander, M. Pustilnik, Y. Meir, N. S. Wingreen, and D. C. Langreth, "How long does it take for the Kondo effect to develop?", **Phys. Rev. Lett. 83, 808–811 (1999)** (cit. on p. 81).

[119]P. Nozières and A. Blandin, "Kondo effect in real metals", **J. Phys. France 41, 193–211 (1980)** (cit. on pp. 12, 13, 18).

[120]J. Nygård, D. H. Cobden, and P. E. Lindelof, "Kondo physics in carbon nanotubes", **Nature 408, 342–346 (2000)** (cit. on p. 19).

[121]O. Parcollet, M. Ferrero, T. Ayral, H. Hafermann, I. Krivenko, L. Messio, and P. Seth, "TRIQS: A toolbox for research on interacting quantum systems", **Comput. Phys. Commun. 196, 398–415 (2015)** (cit. on pp. 9, 54).

[122]J. J. Parks, A. R. Champagne, T. A. Costi, W. W. Shum, A. N. Pasupathy, E. Neuscamman, S. Flores-Torres, P. S. Cornaglia, A. A. Aligia, C. A. Balseiro, G. K.-L. Chan, H. D. Abruña, and D. C. Ralph, "Mechanical control of spin states in spin-1 molecules and the underscreened Kondo effect", **Science 328, 1370–1373 (2010)** (cit. on p. 19).

[123]R. Peters, T. Pruschke, and F. B. Anders, "Numerical renormalization group approach to Green's functions for quantum impurity models", **Phys. Rev. B 74, 245114 (2006)** (cit. on p. 21).

[124]L. Pollet, "Recent developments in quantum Monte Carlo simulations with applications for cold gases", **Rep. Prog. Phys. 75, 094501 (2012)** (cit. on p. 45).

[125]H. Pothier, S. Guéron, N. O. Birge, D. Esteve, and M. H. Devoret, "Energy distribution function of quasiparticles in mesoscopic wires", **Phys. Rev. Lett. 79, 3490–3493 (1997)** (cit. on p. 87).

[126]R. M. Potok, I. G. Rau, H. Shtrikman, Y. Oreg, and D. Goldhaber-Gordon, "Observation of the two-channel Kondo effect", **Nature 446, 167 (2007)** (cit. on pp. 7, 20).

[127]W. H. Press, B. P. Flannery, S. A. Teukolsky, and W. T. Vetterling, "Numerical recipes in C: the art of scientific computing", in, Numerical Recipes (Cambridge University Press, 1992), p. 73 (cit. on p. 51).

[128]R. E. V. Profumo, C. Groth, L. Messio, O. Parcollet, and X. Waintal, "Quantum Monte Carlo for correlated out-of-equilibrium nanoelectronic devices", **Phys. Rev. B 91, 245154 (2015)** (cit. on pp. 9, 10, 25, 27, 36–38, 45, 46, 50, 51, 62, 64, 74, 81, 89, 94).

[129]N. V. Prokof'ev and B. V. Svistunov, "Bold diagrammatic Monte Carlo: A generic sign-problem tolerant technique for polaron models and possibly interacting many-body problems", **Phys. Rev. B 77, 125101 (2008)** (cit. on pp. 9, 45, 61).

[130]N. V. Prokof'ev, B. V. Svistunov, and I. S. Tupitsyn, "Exact, complete, and universal continuous-time worldline Monte Carlo approach to the statistics of discrete quantum systems", **J. Exp. Theor. Phys. 87, 310–321 (1998)** (cit. on p. 9).

[131]N. V. Prokof'ev and B. V. Svistunov, "Polaron problem by diagrammatic quantum Monte Carlo", **Phys. Rev. Lett. 81, 2514–2517 (1998)** (cit. on pp. 9, 45).

[132]N. Prokof'ev and B. Svistunov, "Bold diagrammatic Monte Carlo technique: When the sign problem is welcome", **Phys. Rev. Lett. 99, 250201 (2007)** (cit. on pp. 9, 45).

[133]M. Pustilnik and L. Glazman, "Kondo effect in quantum dots", **J. Phys.: Condens. Matter 16, R513–R537 (2004)** (cit. on pp. 22, 23).

[134]J. Rammer, *Quantum field theory of non-equilibrium states* (Cambridge University Press, 2007) (cit. on pp. 9, 27, 28, 30, 31).

[135]M. Ridley, V. N. Singh, E. Gull, and G. Cohen, "Numerically exact full counting statistics of the nonequilibrium Anderson impurity model", **Phys. Rev. B 97, 115109 (2018)** (cit. on pp. 7, 9, 25).

[136]L. Riegger, N. Darkwah Oppong, M. Höfer, D. R. Fernandes, I. Bloch, and S. Fölling, "Localized magnetic moments with tunable spin exchange in a gas of ultracold fermions", **Phys. Rev. Lett. 120, 143601 (2018)** (cit. on p. 7).

[137]N. Roch, S. Florens, T. A. Costi, W. Wernsdorfer, and F. Balestro, "Observation of the underscreened Kondo effect in a molecular transistor", **Phys. Rev. Lett. 103, 197202 (2009)** (cit. on p. 19).

[138]A. Rosch, J. Kroha, and P. Wölfle, "Kondo effect in quantum dots at high voltage: universality and scaling", **Phys. Rev. Lett. 87, 156802 (2001)** (cit. on p. 23).

[139]R. Rossi, T. Ohgoe, E. Kozik, N. Prokof'ev, B. Svistunov, K. Van Houcke, and F. Werner, "Contact and momentum distribution of the unitary Fermi gas", **Phys. Rev. Lett. 121, 130406 (2018)** (cit. on p. 45).

[140]R. Rossi, T. Ohgoe, K. Van Houcke, and F. Werner, "Resummation of diagrammatic series with zero convergence radius for strongly correlated fermions", **Phys. Rev. Lett. 121, 130405 (2018)** (cit. on p. 61).

[141]R. Rossi, N. Prokof'ev, B. Svistunov, K. Van Houcke, and F. Werner, "Polynomial complexity despite the fermionic sign", **EPL 118, 10004 (2017)** (cit. on pp. 64, 89).

[142]R. Rossi, "Determinant diagrammatic Monte Carlo algorithm in the thermodynamic limit", **Phys. Rev. Lett. 119, 045701 (2017)** (cit. on pp. 9, 45).

[143]R. Rossi, "Direct sampling of the self-energy with Connected Determinant Monte Carlo", **arXiv:1802.04743 (2018)** (cit. on p. 45).

[144]A. N. Rubtsov and A. I. Lichtenstein, "Continuous-time quantum Monte Carlo method for fermions: Beyond auxiliary field framework", **JETP Letters 80, 61–65 (2004)** (cit. on pp. 9, 21, 45).

[145]A. N. Rubtsov, V. V. Savkin, and A. I. Lichtenstein, "Continuous-time quantum Monte Carlo method for fermions", **Phys. Rev. B 72, 035122 (2005)** (cit. on pp. 21, 35, 45).

[146]M. Schiró, "Real-time dynamics in quantum impurity models with diagrammatic Monte Carlo", **Phys. Rev. B 81, 085126 (2010)** (cit. on pp. 24, 45).

[147]M. Schiró and M. Fabrizio, "Real-time diagrammatic Monte Carlo for nonequilibrium quantum transport", **Phys. Rev. B 79, 153302 (2009)** (cit. on pp. 24, 45).

[148]M. Schiró and M. Fabrizio, "Time-dependent mean field theory for quench dynamics in correlated electron systems", **Phys. Rev. Lett. 105, 076401 (2010)** (cit. on p. 24).

[149]J. Schmid, J. Weis, K. Eberl, and K. v. Klitzing, "A quantum dot in the limit of strong coupling to reservoirs", **Physica B: Condens. Matter 256-258, 182–185 (1998)** (cit. on pp. 7, 18).

[150]H. Schmidt and P. Wölfle, "Transport through a Kondo quantum dot: Functional RG approach", **Ann. Phys. 19, 60–74 (2010)** (cit. on p. 24).

[151]T. L. Schmidt, P. Werner, L. Mühlbacher, and A. Komnik, "Transient dynamics of the Anderson impurity model out of equilibrium", **Phys. Rev. B 78, 235110 (2008)** (cit. on pp. 24, 45).

[152]H. Schoeller, "A perturbative nonequilibrium renormalization group method for dissipative quantum mechanics", **Eur. Phys. J. Spec. Top. 168, 179–266 (2009)** (cit. on p. 24).

[153]U. Schollwöck, "The density-matrix renormalization group", **Rev. Mod. Phys. 77, 259–315 (2005)** (cit. on p. 9).

[154]U. Schollwöck, "The density-matrix renormalization group in the age of matrix product states", **Ann. Phys. (N. Y.) 326, January 2011 Special Issue, 96–192 (2011)** (cit. on p. 9).

[155]J. R. Schrieffer and P. A. Wolff, "Relation between the Anderson and Kondo Hamiltonians", **Phys. Rev. 149, 491–492 (1966)** (cit. on p. 20).

[156]F. Schwarz, I. Weymann, J. von Delft, and A. Weichselbaum, "Nonequilibrium steady-state transport in quantum impurity models: a thermofield and quantum quench approach using matrix product states", **Phys. Rev. Lett. 121, 137702 (2018)** (cit. on pp. 7, 9, 24).

[157]J. Schwinger, "Brownian motion of a quantum oscillator", **J. Math. Phys. 2, 407–432 (1961)** (cit. on p. 9).

[158]D. Segal, A. J. Millis, and D. R. Reichman, "Numerically exact path-integral simulation of nonequilibrium quantum transport and dissipation", **Phys. Rev. B 82, 205323 (2010)** (cit. on p. 24).

[159]H. Shi and S. Zhang, "Infinite variance in fermion quantum Monte Carlo calculations", **Phys. Rev. E 93, 033303 (2016)** (cit. on p. 47).

[160]F. Šimkovic IV and E. Kozik, "Determinant Monte Carlo for irreducible Feynman diagrams in the strongly correlated regime", **Phys. Rev. B 100, 121102(R) (2019)** (cit. on pp. 9, 45).

[161]G. Stefanucci and R. van Leeuwen, *Nonequilibrium many-body theory of quantum systems: a modern introduction* (Cambridge University Press, 2013) (cit. on p. 74).

[162]H. Steinberg, G. Barak, A. Yacoby, L. N. Pfeiffer, K. W. West, B. I. Halperin, and K. Le Hur, "Charge fractionalization in quantum wires", **Nat. Phys. 4, 116 (2007)** (cit. on p. 7).

[163]H. Theil, "A rank-invariant method of linear and polynomial regression analysis", in ***Henri theil's contributions to economics and econometrics: econometric theory and methodology***, edited by B. Raj and J. Koerts (Springer Netherlands, Dordrecht, 1992), pp. 345–381 (cit. on p. 67).

[164]A. I. Tóth, C. P. Moca, Ö. Legeza, and G. Zaránd, "Density matrix numerical renormalization group for non-Abelian symmetries", **Phys. Rev. B 78, 245109 (2008)** (cit. on p. 78).

[165]A. Tsvelick and P. Wiegmann, "Exact results in the theory of magnetic alloys", **Adv. Phys. 32, 453–713 (1983)** (cit. on pp. 7, 11, 18).

[166]K. Van Houcke, F. Werner, E. Kozik, N. Prokof'ev, B. Svistunov, M. J. H. Ku, A. T. Sommer, L. W. Cheuk, A. Schirotzek, and M. W. Zwierlein, "Feynman diagrams versus Fermi-gas Feynman emulator", **Nat. Phys. 8, 366 (2012)** (cit. on pp. 9, 45, 61).

[167]K. Van Houcke, F. Werner, T. Ohgoe, N. V. Prokof'ev, and B. V. Svistunov, "Diagrammatic Monte Carlo algorithm for the resonant Fermi gas", **Phys. Rev. B 99, 035140 (2019)** (cit. on p. 45).

[168]K. Van Houcke, E. Kozik, N. Prokof'ev, and B. Svistunov, "Diagrammatic Monte Carlo", **Physics Procedia 6, 95–105 (2010)** (cit. on p. 45).

[169]R. Van Roermund, "Theoretical study of non-equilibrium transport in Kondo quantum dots", Thesis (Université de Grenoble, Oct. 2010) (cit. on p. 23).

[170]R. Van Roermund, S.-y. Shiau, and M. Lavagna, "Anderson model out of equilibrium: Decoherence effects in transport through a quantum dot", **Phys. Rev. B 81, 165115 (2010)** (cit. on p. 23).

[171]P. Wang and S. Kehrein, "Flow equation calculation of transient and steady-state currents in the anderson impurity model", **Phys. Rev. B 82, 125124 (2010)** (cit. on p. 24).

[172]S. Weiss, J. Eckel, M. Thorwart, and R. Egger, "Iterative real-time path integral approach to nonequilibrium quantum transport", **Phys. Rev. B 77, 195316 (2008)** (cit. on p. 24).

[173]P. Werner, A. Comanac, L. de'Medici, M. Troyer, and A. J. Millis, "Continuous-time solver for quantum impurity models", **Phys. Rev. Lett. 97, 076405 (2006)** (cit. on pp. 9, 21, 24, 45).

[174]P. Werner, T. Oka, M. Eckstein, and A. J. Millis, "Weak-coupling quantum Monte Carlo calculations on the Keldysh contour: Theory and application to the current-voltage characteristics of the Anderson model", **Phys. Rev. B 81, 035108 (2010)** (cit. on pp. 7, 9, 24, 45, 83, 85).

[175]P. Werner, T. Oka, and A. J. Millis, "Diagrammatic Monte Carlo simulation of nonequilibrium systems", **Phys. Rev. B 79, 035320 (2009)** (cit. on pp. 9, 24, 45, 85).

[176]S. R. White, "Density matrix formulation for quantum renormalization groups", **Phys. Rev. Lett. 69, 2863–2866 (1992)** (cit. on p. 9).

[177]S. R. White, "Density-matrix algorithms for quantum renormalization groups", **Phys. Rev. B 48, 10345–10356 (1993)** (cit. on p. 9).

[178]S. R. White and A. E. Feiguin, "Real-time evolution using the density matrix renormalization group", **Phys. Rev. Lett. 93, 076401 (2004)** (cit. on p. 24).

[179]P. Wiegmann, "Exact solution of s-d exchange model at $T = 0$", Sov. Phys. JETP Lett. **31**, 392 (1980) (cit. on pp. 7, 18).

[180]P. Wiegmann, "Towards an exact solution of the Anderson model", **Phys. Lett. A 80, 163–167 (1980)** (cit. on pp. 7, 20).

[181]K. G. Wilson, "The renormalization group: Critical phenomena and the Kondo problem", **Rev. Mod. Phys. 47, 773–840 (1975)** (cit. on pp. 7, 9, 11, 12, 16).

[182]N. S. Wingreen and Y. Meir, "Anderson model out of equilibrium: Noncrossing-approximation approach to transport through a quantum dot", **Phys. Rev. B 49, 11040–11052 (1994)** (cit. on pp. 23, 24, 83).

[183]K. Yamada, "Perturbation expansion for the Anderson Hamiltonian. II", **Prog. of Theor. Phys. 53, 970 (1975)** (cit. on pp. 20, 76, 77).

[184]K. Yosida and K. Yamada, "Perturbation expansion for the Anderson Hamiltonian", **Prog. of Theor. Phys. Supp. 46, 244–255 (1970)** (cit. on p. 20).

[185]X. Zheng, J. Jin, S. Welack, M. Luo, and Y. Yan, "Numerical approach to time-dependent quantum transport and dynamical Kondo transition", **J. Chem. Phys. 130, 164708 (2009)** (cit. on p. 24).